



# Structural and electrical properties of Co-doped ZnO prepared by DC-Magnetron co-sputtering for spintronic applications

Edgar Felipe Galíndez Ruales

Universidad Nacional de Colombia  
Science Faculty, Physics Department  
Bogotá, Colombia  
2020



# Structural and electrical properties of Co-doped ZnO prepared by DC-Magnetron co-sputtering for spintronic applications

Edgar Felipe Galíndez Ruales

Thesis presented as a partial requisite to apply for the title of:  
**Master in Science - Physics**



Advisor:  
Ph.D. Anderson Dussán Cuenca

Line of Research:  
Diluted Magnetic Semiconductors  
Research Group:  
Nanostructured Materials and Their Applications

Universidad Nacional de Colombia  
Science Faculty, Physics Department  
Bogotá, Colombia  
2020





Sanity and happiness are an impossible combination.

Mark Twain

To my parents.



# Acknowledgements

At the end of this important step in my scientific career as a physicist, I would like to express my most sincere gratitude to all that have been a support through the past years. First of all, I want to thank the essence of the higher, which allows me every day to have nature phenomena to explore and think about. To my parents, who are the pioneers in my education and scientific taste. Without them, this whole project would have been just a dream. For their unconditional support and love, I have nothing more to give than my greater respect.

To my sis Laura, for her oxygenating talks and her smile. To my chosen-brother Luis, for his hugs, support, comprehension, patience, and love. To my dear friend Jose, for his jokes, support, wisdom, and advice, I wish to be as brave as you are. This work is possible thanks to the emotional support of these persons, which I will always have in the deep of my heart.

To the Group of Nanostructured materials and their Applications, especially to professor Anderson Dussan, to whom I would be glad to offer my gratitude for the last four years of support and commitment. To him, who always believed in my capabilities, even before me, I want to present my most intensive admiration for the person and scientific who he is. Specially thanks to professor Fredy Mesa and professor Rafael González-Hernández, who were an incredible addition to my scientific development, with whom I hope to continue collaborating and growing. Also, I want to thank Heiddy, Jorge, and all the groupmates, that despite our differences have been a huge help in this project and my realization as a person. I am also grateful for the opportunity to teach that the Physics department gave me with the assistant teaching scholarship, especially to professor Yuly Sanchez.

Finally, but absolutely not least, to the light of my eyes, my friend and love Camila. This work is successfully finished because she became part of my life and without her wholehearted support, care and motivation I could not have done this. There are no words to express how grateful I am for having her in my life. For she, I only have my unwavering love and the sureness that every future step next to her will make us better humans.

In memory of my grandpa, who I know is proud of me, wherever he is.



# Abstract

In this work, the effect of Cobalt in  $ZnO$  thin films was studied. The samples were synthesized by DC-Magnetron co-sputtering over different substrates (Glass,  $Al_2O_3$ , ITO,  $Si$ , and  $Au$ ). Structural and electrical properties were studied through several characterization techniques, correlating the synthesis parameters and varying them until an optimal semiconductor matrix was achieved. Looking for the best configuration for a spintronic device, these and other characteristics of the samples were studied using diverse techniques, such as scanning electron microscopy, Auger spectroscopy, X-ray diffraction, atomic force microscopy, energy-dispersive X-ray spectroscopy, ultraviolet-visible-near-infrared spectroscopy, electric measurements (Resistance and current-voltage curves) and magnetization measurements. Additionally, a computational study of the oxygen vacancies and cobalt role in the room-ferromagnetism was performed. This approach was based on the density functional theory, where different configurations of impurities were analyzed. A room temperature ferromagnetic stability was predicted in the  $Zn_xCo_{1-x}O_y$  structure, also a decrease in the magnetic moment was founded when the oxygen vacancies increased. Experimentally, the Cobalt concentration in the samples was determined and secondary phases of Cobalt were not found in concentrations below 15%, and the d-d bond was confirmed by optical measurements. The thickness of the thin films was between 50 and 190 nm, with Zinc:Oxygen in a 2:1 proportion. On the surface of the samples, the roughness increased with the cobalt concentration, and the samples with  $\sim 15\%$  presented a superficial magnetic orientation. The application as non-volatile memory was studied, current-voltage measurements showed the resistive switching phenomenon reported for the pure semiconductor, with a strong correlation with the Cobalt. The switching was performed with different limit currents and, the reliability and durability of the device were tested. The samples' magnetization exhibited hysteresis loops at room temperature when the samples have a considerable crystallinity. The magnetic behavior at room temperature along with the interesting electric properties brings the  $Co : ZnO$  thin films prepared by DC-magnetron co-sputtering as a possible spintronic material for electronic applications.

**Keywords:**  $ZnO$ , room-temperature ferromagnetism, resistive switching, non-volatile memories, Cobalt.

# Resumen

En este trabajo se estudió el efecto del cobalto en películas delgadas de  $ZnO$ . Las muestras se sintetizaron mediante pulverización catódica sobre diferentes sustratos (vidrio,  $Al_2O_3$ , ITO,  $Si$  y  $Au$ ). Las propiedades estructurales y eléctricas fueron estudiadas, correlacionando los parámetros de síntesis y variándolos hasta lograr un semiconductor óptimo. Con la aplicación espintrónica en mente, se estudiaron estas y otras características de las muestras utilizando diversas técnicas, como microscopía electrónica de barrido, espectroscopía Auger, difracción de rayos X, microscopía de fuerza atómica, espectroscopía de rayos X de energía dispersiva, foto-espectroscopía, medidas eléctricas (resistencia y curvas de corriente-voltaje) y medidas de magnetización. Además, se realizó un estudio computacional sobre el papel de las vacancias de oxígeno y el cobalto en el ferromagnetismo a temperatura ambiente. Este enfoque se basó en la teoría funcional de la densidad, donde se analizaron diferentes configuraciones de impurezas y se predijo una estabilidad ferromagnética a temperatura ambiente. Experimentalmente, se determinó la concentración de cobalto en las muestras y no se encontraron fases secundarias en concentraciones por debajo del 15 %. La presencia del enlace d-d se confirmó mediante mediciones ópticas de las películas delgadas, cuyo espesor varió entre 50 y 190 nm, con una proporción entre Zinc: Oxígeno de 2: 1. En la superficie de las muestras, la rugosidad aumentó con la concentración de cobalto, y las muestras con  $\sim 15\%$  presentaron una orientación magnética superficial. Las medidas de corriente-voltaje mostraron el fenómeno de conmutación resistiva reportado para el semiconductor puro, con una fuerte correlación con el cobalto. La conmutación se realizó con diferentes corrientes límite, donde la confiabilidad y durabilidad del dispositivo fue comprobada. La magnetización de las muestras exhibió histéresis a temperatura ambiente en las muestras con cristalinidad considerable. El comportamiento magnético a temperatura ambiente junto con las interesantes propiedades eléctricas hace que las películas delgadas de  $Co : ZnO$  preparadas mediante pulverización catódica sean un posible material con aplicaciones en la espintrónica.

**Palabras clave:**  $ZnO$ , ferromagnetismo, conmutación resistiva, memorias no volátiles, cobalto.

# Contents

<b>Acknowledgements</b>	<b>vii</b>
<b>Abstract</b>	<b>ix</b>
<b>List of figures</b>	<b>xii</b>
<b>List of tables</b>	<b>xv</b>
<b>1. Introduction</b>	<b>2</b>
<b>2. <i>Co</i>-doped <i>ZnO</i> as Oxide Diluted Magnetic Semiconductor</b>	<b>6</b>
2.1. State of the art: Generalities . . . . .	6
2.2. Experimental aspects . . . . .	8
2.3. Synthesis characteristics . . . . .	10
<b>3. <math>Zn_{1-x}O_yCo_x</math> Density Functional Theory approach</b>	<b>14</b>
3.1. State of the art: Computational approaches . . . . .	15
3.2. Theoretical aspects . . . . .	16
3.3. Methods and model . . . . .	18
3.4. Results and discussion . . . . .	21
3.4.1. Effect of $Co - V_O$ distance in the $Zn_{1-x}O_yCo_x$ system . . . . .	21
3.4.2. Effect of the $V_O$ on the magnetic and electronic properties of <i>Co</i> -doped Zinc oxide . . . . .	24
<b>4. Structural and morphological characterization of Cobalt doped <i>ZnO</i></b>	<b>29</b>
4.1. State of the art: Structural and morphological properties . . . . .	29
4.2. Experimental aspects . . . . .	30
4.3. Methods and model . . . . .	34
4.4. Results and discussions . . . . .	35
<b>5. Electrical, optical and magnetic characterization of Cobalt doped <i>ZnO</i> thin films</b>	<b>50</b>
5.1. State of the art: Electrical, optical and magnetic properties . . . . .	50
5.2. Experimental aspects . . . . .	53
5.3. Methods and model . . . . .	55

---

5.4. Results and discussions . . . . .	56
<b>6. Conclusions and perspectives</b>	<b>72</b>
6.1. Conclusions . . . . .	72
6.2. Perspectives . . . . .	74
6.3. Peer-reviewed articles . . . . .	75
6.3.1. <i>ZnO</i> DFT approach . . . . .	75
6.3.2. Cobalt influence in DMS . . . . .	75
<b>A. Appendix: Purity report of ZnO and Co targets</b>	<b>76</b>
<b>B. Appendix: Substrates data-sheet</b>	<b>79</b>
<b>C. Appendix: PDF files from XRD analysis</b>	<b>82</b>



# List of Figures

<b>2-1.</b>	(a) Sputtering chamber distribution sketch and (b) substrates distribution in the synthesis of <i>Co</i> -doped <i>ZnO</i> (Yellow for gold/glass, green for ITO/glass, blue for <i>Si</i> , purple for $Al_2O_3/Al$ /glass, gray for <i>Ti</i> and white for glass) . . .	11
<b>3-1.</b>	Wurtzite single cell, with two different tetrahedrons, of <i>Co</i> -doped (Blue spheres) <i>ZnO</i> (left) and 332 super-cell (F-Configuration in Table <b>3-1</b> ). Large yellow (small whitish) spheres designate <i>Zn</i> ( <i>O</i> ) atoms. . . . .	18
<b>3-2.</b>	Formation Energy for different impurities configurations in the <i>ZnO</i> matrix.	20
<b>3-3.</b>	Effect of <i>Co</i> – <i>V<sub>O</sub></i> distance in (left) the total magnetic moment per Cobalt atom in (a) 1 : 1 ( <i>Co</i> : <i>V<sub>O</sub></i> ) ratio, (b) 1 : 2 ratio and (c) Formation energy, for different cobalt concentrations and one <i>V<sub>O</sub></i> per super-cell. . . . .	22
<b>3-4.</b>	(a) Average contribution from <i>Co</i> , interstitial region, <i>Zn</i> and <i>O</i> , to the total magnetic moment per Cobalt atom and (b) contributions per orbital into the Cobalt atom. . . . .	22
<b>3-5.</b>	Difference between Ferromagnetic ( $E_{\uparrow\uparrow}$ ) and Anti-ferromagnetic ( $E_{\uparrow\downarrow}$ ) formation energies as function of the <i>Co</i> – <i>Co</i> (5, 56% <i>Co</i> ) distance for configurations with and without <i>V<sub>O</sub></i> , the right axis shows the exchange constant $J_0$ in the model Eq. 3-10. . . . .	23
<b>3-6.</b>	Spin density difference ( $\rho_{\uparrow} - \rho_{\downarrow}$ ) section (plane $(\bar{1}2\bar{1}0)$ ) of Cobalt doped <i>ZnO</i> with <i>V<sub>O</sub></i> (left) and without <i>V<sub>O</sub></i> (right). . . . .	24
<b>3-7.</b>	Spin density difference ( $\rho_{\uparrow} - \rho_{\downarrow}$ ) section (plane $(\bar{1}2\bar{1}0)$ ) of Cobalt doped <i>ZnO</i> with 12, 5% of <i>V<sub>O</sub></i> -1 $C_o$ : 2 $V_o$ relation-(left) and without <i>V<sub>O</sub></i> (right). . . . .	25
<b>3-8.</b>	Spin density difference ( $\rho_{\uparrow} - \rho_{\downarrow}$ ) section (plane $(11\bar{2}0)$ ) and iso-surfaces (outer) of (a) Antiferromagnetic and (b) ferromagnetic configurations. Cobalt doped <i>ZnO</i> with <i>V<sub>O</sub></i> (left) and without <i>V<sub>O</sub></i> (right). . . . .	26
<b>3-9.</b>	Total DOS and PDOS ( <i>Co</i> , <i>O</i> and <i>Zn</i> ) of most stable structures in Ferromagnetic configuration with 5,56% of <i>Co</i> , (a) without <i>V<sub>O</sub></i> and (b) with <i>V<sub>O</sub></i> at 2, 77%. The zero of the energy has been set at the Fermi level, as indicated with dashed lines. The values of the positive (negative) states correspond to the majority (minority) spin regions. . . . .	27
<b>4-1.</b>	Contour plot of the relative Cobalt atomic concentration as a function of the localization in the substrate holder. . . . .	35

4-2.	(a) Profilometer results of a $ZnO$ thin film sample in its interface. (b) $ZnO$ Thickness as a function of the deposit time for two different $Co$ concentration, whit a $Ln$ -like fit. . . . .	36
4-3.	Auger spectroscopy results for $ZnO$ thin films synthesized at different $P_{Co}$ . . . . .	37
4-4.	Average atomic composition of the $Co : ZnO$ thin films through Auger spectroscopy for samples synthesized with (a) $P_{Co} = 0$ W, (b) $P_{Co} = 20$ W, (c) $P_{Co} = 40$ W, and (d) $P_{Co} = 60$ W. . . . .	38
4-5.	Powder X-ray diffraction pattern for $ZnO$ thin films deposited over different substrates, along with the XRD measurement for $Au$ , $Al_2O_3$ , and $Si$ substrates. . . . .	39
4-6.	X-ray diffraction pattern of the $Co : ZnO/Al_2O_3$ samples synthesized at different Cobalt target power. . . . .	41
4-7.	X-ray diffraction pattern of the $Co : ZnO/Si$ samples synthesized at different Cobalt target power. . . . .	41
4-8.	Diffraction pattern for the $Co$ doped $ZnO$ samples over $Al_2O_3$ prepared at different substrate temperature. . . . .	43
4-9.	Diffraction pattern for the $Co$ doped $ZnO$ samples over $Si$ prepared at different substrate temperature. . . . .	43
4-10.	SEM micrographs of $Co : ZnO/Ti$ thin films fabricated at 293(4) K (left) and 373(2) K (right). All micrograph are from SE at $HV = 30$ kV, average $WD = 10,05(1)$ mm and magnifications of 10kx (a, b), 20kx (c, d), and 40kx (e, f). . . . .	45
4-11.	SEM micrographs of $Co : ZnO$ thin films fabricated at 423(2) K over $Ti$ (a, g), $Au$ (b, h), soda-lime glass (c, i), ITO (d), $Al_2O_3$ (e, j), and $Si$ (f). All micrograph are from SE at $HV = 30$ kV (except c and i at 10 kV), average $WD = 9,8(1)$ mm and magnifications of 10kx (a, b, c, d, e, f), 20kx (h, j), 36kx (i), and 40kx (g). . . . .	46
4-12.	AFM/MFM micrographs of $ZnO$ (a-c) and $Co$ -doped $ZnO$ . Thin films prepared over soda-lime glass at 423(2) K and $P_{Co} = 20$ W (d-f), $P_{Co} = 40$ W (g-i), and $P_{Co} = 60$ W (j-l). All the color-bars scale are in nm. Gold figures AFM Height, and cold-warm scale represent the amplitude of the signal from the magnetic interaction. Z-axis in 3D plots represent the AFM height. . . . .	47
4-13.	Root mean square roughness as a function of the Cobalt power target for $Co : ZnO$ thin films synthesized at 473(2) K over soda-lime glass. Error bars represent the standard deviation. . . . .	48
5-1.	Arrangement of the different upper electrodes in the $Co : ZnO$ film deposited on the lower electrode (ITO). On the right side, the configuration for sheet measurements can be observed. . . . .	55
5-2.	Bipolar resistive switching for a sample of $Au/ZnO/ITO$ thin film prepared at 423(2) K (250 cycles performed). . . . .	57

5-3.	Current (right) and resistance (left) in the switching cycles for <i>Co</i> -doped <i>ZnO</i> thin films at different $P_{Co}$ and prepared at 423(2) K. Current limit fix to 0, 2 mA in all the 250 cycles. . . . .	58
5-4.	Current-Voltage SET cycles (250) for the different <i>Co</i> concentrations at their optimal (op) limit current. . . . .	59
5-5.	Average LRS and HRS as function of the deposit time for <i>Co</i> -doped <i>ZnO</i> at 13, 19 %. The limit current was the optimal (red and black) or fix at 0, 1 mA (blue and red). Error bars represent the state dispersion of the average over 250 cycles. . . . .	60
5-6.	Low and high resistance states as a function of the number of cycles for a <i>Au/Co : ZnO/ITO</i> system. . . . .	61
5-7.	LRS and average HRS as a function of the time for a <i>Au/Co : ZnO/ITO</i> system. . . . .	62
5-8.	Absorbance spectrum for different Cobalt concentrations in <i>Co : ZnO/Glass</i> . . . . .	63
5-9.	Bode plots for the impedance bulk measurement of <i>Au/Co : ZnO/ITO</i> systems at different Cobalt concentrations: 0 % at. (a), 8,7 % at. (b), 13,19 % at. (c), and 14,39 % at. (d). . . . .	64
5-10.	Normalized Nyquist plot for different Cobalt concentrations in the <i>Co : ZnO/ITO</i> thin films. The inset shows the low frequencies range for the highest concentration of Cobalt. . . . .	65
5-11.	ALIS results of the <i>Au/Co : ZnO/ITO</i> systems: Amplitude reduction and phase shift for the sample illuminated with $\lambda = 390$ nm (left) and $\lambda = 632$ nm (right). . . . .	66
5-12.	Sheet resistivity of <i>Co : ZnO</i> for different Cobalt concentrations in the 0-6 V range. . . . .	67
5-13.	Annealing effect in the magnetization as a function of the externally applied field. Measurements realized at 150 K (a, c) and 300 K (b) of <i>Co</i> -doped <i>ZnO/Glass</i> at 13, 19 %. Sub-figure c shows zoom-in low fields. . . . .	68
5-14.	Magnetization of the $Al_2O_3$ substrate as function of the magnetic field (red line) and No-diamagnetic magnetization contribution (black line). The inset shows these magnetization at low external fields. . . . .	69
5-15.	M-H curves for each different $P_{Co}$ at 300 K. Blue(black) lines correspond to the blue(black) magnetization scale. . . . .	70
5-16.	Magnetization as a function of the external field at 50 K (a) and 300 K (b), for the <i>Co : ZnO</i> thin film doped at 14, 39%. (c) FC curve at 300 Oe for the same sample. . . . .	71

# List of Tables

2-1.	Different synthesis parameters for the $ZnO$ and $Co$ -doped $ZnO$ thin films series.	12
3-1.	$Zn_{1-x}O_yCo_x$ systems studied (A-H configurations) at different $V_O$ and $Co$ composition, in 222 or 332 super-cells and its $Co - Co$ characteristic distances.	19
4-1.	Identified peaks in Fig. 4-5 for substrates and $Co$ doped $ZnO$ thin films. . .	40
4-2.	Principal peaks position, FWHM, and relative intensities values/changes extracted from the XRD patterns of the $Co : ZnO$ samples synthesized at different powers for the Cobalt target. . . . .	42
4-3.	Principal peaks position, FWHM, and relative intensities values/changes extracted from the XRD patterns of the $Co : ZnO$ samples synthesized at different substrate temperature. . . . .	44
5-1.	Powers of SET and RESET for different Cobalt concentration and current limit.	60
5-2.	Gap values for the different $Co$ concentrations in the $ZnO$ thin films over glass and ITO. . . . .	63
5-3.	Equivalent circuit scheme and values for the different Cobalt doped $ZnO$ thin films. . . . .	66

# 1. Introduction

The modern era has brought along with technological innovations the need to handle enormous amounts of digital data [1]. Every day the humanity creates 2,5 quintillion bytes of data [2]. This would fill 10 million Blu-ray discs, the height of which stacked would measure the height of four Eiffel Towers one top another. That information needs to be processed, stored, and analyzed at high speeds; in 2013 global internet traffic was approximately 51 billion gigabytes, in 2018 grew to 50 000 GB per second, and today the number of people who have access to the internet equals that of the world population in 1960 (3 billion) [2]. In this context, velocity is defined as the increasing speed at which data is created and the speed at which it can be processed, stored and analyzed. Analyzing that information is a challenge for the current coding, due to the lack of data structure, the growing social need for privacy and encryption, and the enormous number of sources and access routes that request the information simultaneously.

Trying to overcome the limitations of the current coding, the scientific community has turned to develop devices that can support the growth of information, which currently has a growth equal to four times the world economy [2]. In particular, the challenge of storage and data processing devices is to deal with information avalanches, preserving or even improving high velocity, with high data density, low power consumption, high durability, and low market prices [3,4]. In this sense, spintronics was born as a hope to take humanity to the next level of information and data processing [5]. The spin could be stored in semiconductors, run at frequencies many times faster than today's technology, and work at room temperature; all in a single nanostructure [6].

Spintronics (a portmanteau meaning spin transport electronics), also known as spin electronics, is the study of the intrinsic spin of the electron and its associated magnetic moment, in addition to its fundamental electric charge, in solid-state devices [7]. Spintronics emerged from discoveries in the 1980s concerning spin-dependent electron transport phenomena in solid-state devices [8]. The first mass-produced spintronic device has already revolutionized the hard-disk drive industry. Introduced in 1997, the giant magneto-resistive (GMR) head, developed at the IBM Almaden lab, is a super-sensitive magnetic-field sensor that enabled a 40-fold increase in data density over the past seven years [9]. The first use of spin-valve sensors in hard disk drive read heads was in the IBM Deskstar 16GP Titan, which was released in 1997 with 16.8 GB of storage [10]. In 2007, Hitachi, which bought IBM's hard drive

---

division in 2003, released the Deskstar 7K1000, the first 1 TB hard disk drive [11]. Today, the Hitachi Deskstar 7K3000 provides up to 3 TB of storage [12]. Another multilayered spintronic structure is at the heart of the high-speed, nonvolatile magnetic random-access memory (MRAM), currently being developed by a handful of companies [6, 13].

One of the proposals that has revolutionized the way of understanding solid matter physics as we know it, and has come close enough to the dreamed electronics, are the spintronic devices. A spintronic device is a system based on materials that take advantage of both the electrical and magnetic properties of the electron, which is considered the fundamental particle in electronic processes. The idea of these devices is to be able to add an extra control variable to the usual electronics, known as spin. In this context, the spin represents an intrinsic magnetic moment of the electron, which in principle has random values. In spintronic materials, the orientation of the spin, which was previously thought to be completely random, is now controllable for short times (1 millisecond = 1/1000 seconds). Adding an extra parameter to the information carried by the electron. Taking advantage of the charge and spin property of the electron, these new bits with an extra variable, result in faster electronics, higher capacity, and a step closer to quantum computing.

Seeking to improve the way of understanding the operation of these devices and optimize their performance, in the last decade materials known as dilute magnetic semiconductors (DMSs) have been studied [14–17]. These materials consist of macroscopic systems of low dimensionality that exhibit spintronic properties [17, 18]. A DMS consists of an embedded semiconductor matrix, in low proportions ( $< 10\%$ ), with atoms of material with magnetic properties [19]. A requirement to obtain a functional DMS is the non-existence of agglomerations or nanostructures of the dopant magnetic material in addition to the non-existence of crystalline phases associated with magnetic ions [20, 21].

The development of DMSs based devices was around 8000 papers per year in the last decade, all of these trying to find an optimal configuration of this semiconductors matrix and its dopants to reach a reproducible and functional material to improve the current technology [22]. The biggest problem with DMSs based on the usual semiconductors is their low Curie temperature, which limits them to laboratory scenarios and makes their development as a commercial device impossible [23].

Beginning with magnetic semiconductors whose spin control properties were observed below 100 K [24], semiconductor oxides, revolutionized the researches by exhibiting (computationally by Dietl and Ohno, 2000 [25]) ferromagnetic behavior at room temperature, and experimentally confirmed in different systems [26–32].

The growth of these doped semiconductors is usually at high temperatures by Molecular

Beam Epitaxy (MBE), an expensive synthesis technique that consists basically of putting atom by atom over a perfect oriented substrate in ultra-high vacuum [33–35]. The results with this method set the tone in the development of the devices, but the high costs and the speed of production are not a solution for the already named growing market [36]. To be able to take a significant step, it is a necessary development in the already revolutionary magnetic seismic oxides, achieving reproducible results, scalable and at a low cost.

Among the semiconductors that have attracted attention to these applications are, among others, the semiconductor oxides based on  $TiO_2$ ,  $ZnO$ ,  $SnO_2$ ,  $Cu_2O$ , etc. In particular, Zinc oxide (ZnO) has been widely studied in different nanostructures, due to its particular electrical, structural, magnetic, chemical, and optical properties. This broadband semiconductor, so-called because of its wide gap, has a stable hexagonal structure, turns out to be friendly to the environment (null toxicity), and has an electronic behavior as a semiconductor. The incorporation of atoms in said matrix, known as doping, usually results by substitution of magnetic ions ( $Mn$ ,  $Co$ ,  $Fe$ , etc.) or by vacancies of oxygen. The doping results in a structure with a magnetic moment different from zero, allowing the exploitation of the magnetic properties of the material.

Current research in DMSs based on ZnO is centralized on expensive synthesis techniques on perfect crystals as substrates, such as Molecular Beam Epitaxy deposit on sapphire or zirconium substrates. Other techniques involve toxic or dangerous reagents and do not produce a homogenous thin film, which limits their reproducibility and scalability. The sputtering method is an intermediate solution, between characteristics like high costs and low homogeneity. This synthesis technique consists of extracting atoms of a high purity target by an attack with ions of a plasma. The extracted atoms travel to the substrate, where diffusion processes determine the growth of the thin film.

To solve how to prepare optimal DMSs based on oxides magnetic semiconductors using a lower-cost synthesis technique and what are the best synthesis parameters for spintronic applications, this proposal is based on the use the sputtering as a synthesis technique, that is already implemented in several industries, low cost compared with MBE, an atom-by-atom deposit technique (which helps to avoid the formation of clusters or secondary phases) and optimized in the research group in which the project was developed. The growth by sputtering is thin film and can be carried out on any surface. To avoid the problem of degradation with the environment and take advantage of theoretical and experimental background on a material well developed in other areas,  $ZnO$  was used as a semiconductor matrix in the project scope and looking for an optimal response as spintronic atoms of Co as dopants. The best synthesis parameters in DC-Magnetron co-sputtering of doped  $ZnO$  thin films for spintronic applications were determined and, finally establishing a guide for future investigations in this material for its application as a spintronic device.

This work, reports the synthesis, characterization, and modeling of the *Co*-doped *ZnO* and its correlation with the synthesis parameters by DC-magnetron co-sputtering. After synthesizing thin films, these were characterized as a function of the synthesis parameters: deposition time, target power, annealing processes, among others. *ZnO : Co* thin films with different concentrations of Co were fabricated using the optimal synthesis parameters and by a study of the electrical properties were improved its applicability in spintronic systems.



## 2. *Co*-doped *ZnO* as Oxide Diluted Magnetic Semiconductor

In this chapter, generalities of Cobalt doped *ZnO* are approached, doing a state of the art compendium that summarizes the last researches in *ZnO* as an Oxide-diluted magnetic semiconductor, that will be thoroughly deepened in the next chapters as being necessary. Also, a theoretical and experimental review is presented, finishing with the synthesis description and parameters that were used in the fabrication of the *Co*-doped *ZnO* samples.

### 2.1. State of the art: Generalities

The semiconductor oxides are a family of materials whose advantage is not found in their mechanical properties but their electrical, structural, magnetic, chemical, and optical characteristics [37]. The applications of these semiconductor matrices are based on two characteristics: the presence of cations with different valence states and an adjustable oxygen deficiency due to oxygen vacancies [38]. Physical properties are adjusted by altering or varying any of these characteristics, generating possible technological exploitation of these materials. Among the most important applications of semiconductor, oxides are their use as gas sensors [39] and the manufacture of transparent conductive electrodes in solar cells [40], flat screens, organic LEDs [41] and other electronic devices [42].

At the nanostructured level, these oxides may manifest some of their altered physical properties, modified or even appear new properties concerning those of the material with a larger scale constitution. The essential components of transparent electronic devices are broadband semiconductors, where the different oxides participate actively, even replacing traditional semiconductors such as silicon [43], gaining special attention during the last years and establishing itself today as one of the most promising technologies to lead the next generation of screens due to its excellent electronic performance [44].

Semiconductor oxides, especially amorphous ones, can be produced at relatively low temperatures ( $< 500^{\circ}\text{C}$ ) and still have highly homogeneous surfaces, whose electronic performances do not depend on the degree of order of the films [45]. These materials represent a revolutionary idea and exhibit interesting properties, such as high optical transparency, high electron mobility, and amorphous micro-structure [46]. Also, these do not have grain limits,

so the main limitation of mobility in poly-crystalline semiconductors is avoided, which is a great advantage for the integration of electronic processes [47].

Among these semiconductors, Zinc oxide is a very promising material for its application as a semiconductor [36, 48–51]. It has a wide bandwidth of direct transition in the spectral region close to UV radiation [52–56], and high binding exciton energy [52–55][53–56]. The processes of excitonic emission in this material can be maintained at high temperatures, equal to or more than room temperature [54, 57]. *ZnO* crystallizes in the structure of wurtzite, the same as *GaN*, but, on the contrary, *ZnO* is available as large crystals [54].

*ZnO* properties have been studied since the early days of semiconductor electronics [58], but the use of *ZnO* as an emergency semiconductor in electronic devices has been hampered by the lack of control over its electrical conductivity. *ZnO* crystals are almost always of type n, whose cause has been the object of extensive debate and investigation [52–56]. With the recent success of nitrides in optoelectronics, *ZnO* has been considered as a substrate for *GaN*, to which it provides a close coincidence [54]. During the last decade, we have witnessed a significant improvement in the quality of *ZnO* mono-crystal substrates and epitaxial films [36, 48–51]. This, in turn, has led to a reactivation of the idea of using *ZnO* as an optoelectronic or electronic material in its own right.

The possibility of using *ZnO* as a complement to *GaN* in optoelectronics has led many research groups around the world to focus on their semiconductor properties, trying to control the involuntary n-type conductivity and achieve p-type conductivity. Theoretical studies, in particular, the calculations of the first principles based on the functional theory of density (DFT), have also contributed to a deeper understanding of the native point defects and impurities on the conductivity in the *ZnO* [59–65]. However, acceptance of doping has remained challenging, and the key factors that would lead to reproducible and stable p-type doping have to be yet identified [36, 48–51]. The transition metals have been introduced to the semiconductor matrix, retaining the electrical properties of the material as semiconductor, but also add new and interesting properties to the material.

Diluted Magnetic Semiconductor materials (DMS) are semiconductors doped with magnetic impurities, where doping atoms are replaced more or less randomly at the host crystal sites where they introduce local magnetic moments. These have attracted interest in the past years due to the combination of semiconductor and magnetic properties within the same material [66, 67]. One of the potential applications that DMS materials can offer is to exploit both the charge and the spin of the electron. Physical properties, such as bandgap or magnetism, now turn out to be functions of particle size and, besides, the level of doping. Therefore, ordered arrays of Nano-sized magnetic semiconductors are promising components for new devices in magneto-electronics or spintronics.

However, the low Curie temperature and the low reproducibility of these magnetic semiconductors have limited their application. These seemed to be one of those research topics whose glory belonged to the past. Fortunately, at the beginning of the nineties, [68–70] the ferromagnetic order was discovered in the DMS III-V with critical temperatures that reached 170 K, which has renewed and intensified the interest in these materials. The semiconductor version of spintronics has also attracted researchers because of the hope of participating in efforts to build quantum information processing devices. While these hopes and expectations have not yet been met, the effort continues, as a good example of recent achievements, quantum dots that contain a single magnetic ion result in a huge advance in experimental quantum information [71].

The nanostructured metal oxides have received a lot of attention and have produced different results with respect to the existence of room-temperature ferromagnetism (RTFM), which has been observed in both pure and doped oxides, in nanoparticles of *SnO*<sub>2</sub>, *CeO*<sub>2</sub>, *ZnO*, *TiO*<sub>2</sub>, among others [21, 31, 72–75]. The variations reported in the results and conclusions are quite controversial; however, it appears that the observed magnetism is affected by particle size, grain boundary area, defects, surface coating, and/or doping [32, 76–78]. Experimental research on doped oxide semiconductors with Transition Metals (TM) has attracted a lot of interest after the prediction that *ZnO* is a promising type for a DMS, due to its predicted RTFM [79].

*ZnO* thin films are generally n-type due to the electronic doping defects originated in *Zn* interstitial, *O* vacancies in the *ZnO* network, or impurities including hydrogen. Recently, Bououdina et al. [80] studied electron properties polarized by spin and discovered that oxygen plays an important role in the magnetic properties observed in *ZnO* systems doped with *Fe*, *Ni*, *Mn*, and *Co*. In general, experimental studies are carried out at high temperature by expensive techniques, such as deposition by molecular beam epitaxy or ion implantation, so a study with a more industrialized, less expensive technique that allows the deposit at low temperatures is an important step for the science of the DMS itself.

## 2.2. Experimental aspects

As DMS matrix, *ZnO* has studied since *Dietl et. al.* [25] predicted that Curie Temperature can increase above room temperature, especially in wide-band-gap semiconductors. After the first report of *ZnO* as DMS with *Mn* doping [81], many studies on *ZnO* doped have been reported with several TMs. However, there is no agreement in the existence and explanation of ferromagnetism. A few studies claim non-ferromagnetic behavior of *ZnO*

doped with TM [81–85], whereas other research claim ferromagnetic behavior of the same compounds [86–94]. The reported values of  $T_C$  scatter from 30 to 550 K and there are strongly correlated with the synthesis conditions. Also, most studies [95] report a hysteresis loop in magnetization-field measurements in Cobalt doped  $ZnO$  and that is their principal argument to claim ferromagnetism behavior. Fabrication of  $Co$ -doped  $ZnO$  thin films has been performed by several synthesis techniques. The surface morphology and bulk structure have a strong dependence of the preparation process [90]. Authors have reported successful synthesis of  $Co$  doped  $ZnO$  nanostructures by Cobalt implanted [96], pulsed laser deposition [97,98], chemical vapor deposition [99], sputtering [100], solid-state reaction technique [101], ultrasonic spray technique [102], spin-coating [103], spray pyrolysis [104], sol-gel method [105] and molecular-beam epitaxy [106].

The deposit by sputtering is a technique of physical vapor deposition that takes advantage of the collisions of an ionized gas (plasma) on a material, commonly known as the target, to release atoms, clusters, or molecules from this through energy transfer of the collisions, to form a thin film on the surface of a substrate. The deposition by this method with two simultaneous targets is known as co-Sputtering, which allows controlling the stoichiometry of the deposited film. The sputtering technique has certain advantages over other forms of synthesis: the uniformity of the films, the thickness control [107], the deposit at low temperatures, the variety of materials that can be sputtered, the possibility of synthesizing mixtures and alloys, the good adhesion of the deposited film and the deposit rate control [108]. The basic sputtering process has been known for many years and a variety of materials have been successfully deposited by this technique [109]. However, the process is limited by low deposit rates, low plasma ionization efficiencies, and a large substrate heating effect. These limitations have been overcome by the development of Sputtering with balanced magnetrons and, more recently, by Sputtering with unbalanced magnetrons [110].

From its origins in 1852, where Sir William Robert Grove described the phenomenon, to more recent research has improved the physical understanding of the Sputtering technique resulting in various industrial applications such as lens coatings [111], microelectronic devices [112], solid-state transistors [113,114], among others. The depositing process is carried out in an airtight chamber that, to have the necessary connections to achieve vacuum conditions, also has two surfaces in opposite positions, where target and substrate are held; there are models with several targets to make a simultaneous or multi-layer synthesis. The system must have the necessary gas inlets and connections that allow controlling the synthesis parameters into the chamber. Depending on the reactive nature of the gas, two types of sputtering are distinguished: reactive and non-reactive. In the first one, the ionized gas ( $O_2$ ,  $N_2$ , ...) reacts with the target, forming compounds ( $TiO_2$ ,  $TiN...$ ) and the non-reactive sputtering is where the gas is inert; usually  $Ar$  is used, due to its low ionization energy (1520,6 kJ / mol), its high molecular mass (39,948 u) and its moderate cost [115]. Accord-

ing to the nature of the voltage used to ionize the gas, the Direct Current (DC) and Radio Frequency (RF) sputtering are distinguished, where RF uses alternating current at radio wave frequencies to avoid charge build-ups on conductive targets [116].

If the ionized gas is directed from the substrate to the target by an electric field, it is said to be Diode type Sputtering. On the contrary, in the magnetron sputtering the gas ions are carried towards the target by a magnetic field, this magnetic field is produced by a magnetron (high current cooled coil) that directs the ions in the gas, increasing their linear momentum and confining the plasma to the surroundings of the target. The magnetron is said to be unbalanced when the field lines reach the substrate and allow the attack of the gas ions on the surface of the substrate and balanced when the field is restricted to the target. Furthermore, the magnetron is said to be compensated when the generated magnetic field takes into account the magnetic nature of the target and compensates for the magnetization caused in response to the imposed field.

### 2.3. Synthesis characteristics

Samples were synthesized by DC magnetron co-sputtering, in a high-vacuum chamber. *ZnO* and *Co* targets of 76, 2 mm diameter, 3 mm thick and 99, 9% purity (see Appendix A), were used with a 70 mm substrate-target distance. Unlike ceramic *ZnO* target, Cobalt target was sputtered in a compensated magnetron, due to its magnetic response. Both targets inclined  $10^\circ$  to the substrate perpendicular line.

Before thin-film synthesis, the chamber was cleaned with acetone, isopropanol, and dried with  $N_2$ ; also, after each deposit chamber was cleaned with isopropanol and dried with  $N_2$ . Before reaching optimal conditions in the sputtering system, high-vacuum conditions were achieved ( $\sim 8 \times 10^{-4}$  Pa), then a high purity  $N_2$  (99, 999%) flux was introduced to the system, as drag gas ( $f_{N_2} = 20$  sccm by 3 minutes). Finally, high vacuum conditions were sustained while temperature conditions were reached in the substrates. Once the temperature was stabilized ( $\pm 3^\circ C$ ), a high purity Argon flux (99, 999% at  $f_{Ar} = 20$  sccm) was constantly injected into the system and a pressure valve was used to fix the chamber pressure work ( $P_w$ ) in 3, 3(1) Pa.

All thin films were synthesized in the same  $P_w$  on different substrates: soda-lime glass, Alumina ( $Al_2O_3$ /Glass), Indium Tin Oxide (*ITO*/Glass), Gold (*Au*/Glass), Titanium (*Ti* sheet) and Silicon (*Si* n-type). All Glass substrates were cleaned following a standardized process: Soap bath, Alconox [117] bath in ultrasound by 15 minutes, distilled water washed, acetic acid ( $CH_3COOH$ ) bath, hydrogen peroxide ( $H_2O_2$ ) bath, deionized water bath in ultrasound by 15 minutes, isopropanol washed and  $N_2$  drying.

*Al* and *Au* films over glass were deposited by thermal evaporation; *ITO*, *Si*, and *Ti* substrates were bought with laboratory standards (see Appendix B).  $Al_2O_3$  substrates were synthesized by thermal-dry evaporation. The *Si* was oxidized by a natural process. Both oxidation processes were performed at 74,6 kPa and high relative humidity. All substrates were stored in a dehumidified vacuum chamber and, just before starting the synthesis, blown with high purity  $N_2$ . Fig. 2-1 shows a schematic diagram of the sputtering chamber and the substrates distribution.

Substrates had always the same distribution inside the chamber, and due to the distri-

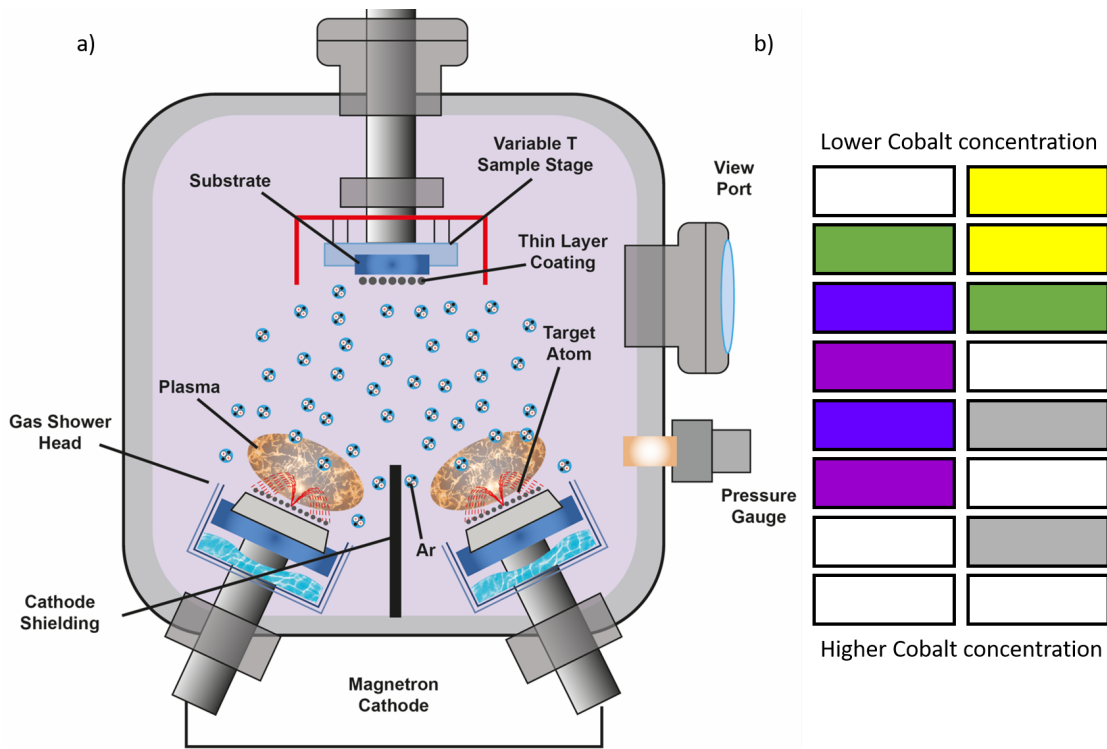


Figure 2-1.: (a) Sputtering chamber distribution sketch and (b) substrates distribution in the synthesis of *Co*-doped *ZnO* (Yellow for gold/glass, green for *ITO*/glass, blue for *Si*, purple for  $Al_2O_3/Al$ /glass, gray for *Ti* and white for glass)

bution of the targets, thin films width and *Co* concentration have a strong dependence on that position. For this reason, the position of the substrates were fixed for all synthesis.

One of the most important conditions to achieve a novel, functional and precursor spintronic material is the existence of intrinsic magnetic properties without magnetic crystal phases. The probability to have secondary phases in the semiconductor matrix is highly dependent on the synthesis method and cobalt concentration. The substrates that are closer to *Co* target have more *Co* concentration than others; to increase the concentration of Cobalt

in each substrate position, sputtering power was varied in a range of 20 W to 60 W to the Cobalt target, and keep fixed in 100 W on the *ZnO* target.

Due to the ceramic nature of the *ZnO* target (Low thermal conductivity), reach a DC power of 100 W is not easy (295,7(1) V at 0,338(1) A). Target manufacturer recommends 20 W/sq<sup>2</sup> for the maximum power and 20 W/min of maximum power increase [118] , for this reason, a power gradual increment was done until 100 W. When this power was reached, the *Co* magnetron was turned-on directly in the required power and one minute of co-sputtering was done to clean the target surface, then shutters were opened for the corresponding deposit time.

First to all, a couple of series were performed without *Co* impurities to study the growth of the semiconductor matrix. In these series, the *ZnO* target power (80 W, 100 W, and 120 W) was varied. After some structural and composition analysis, the 100 W target power was established as the optimal-safely. Different deposit times, temperatures and *Co*-target power were used to achieve an optimal *ZnO*-based DMS. Table **2-1** shows the different variable parameters. The other deposit parameters were remain constant: work pressure ( $P_W = 3,3(1)$  Pa), Argon flux ( $f_{Ar} = 20,0(1)$  sccm) and, *ZnO*-target power ( $P_{ZnO} = 100,00(5)$  W).

Table **2-1.**: Different synthesis parameters for the *ZnO* and *Co*-doped *ZnO* thin films series.

Series (Label)	Substrate Temperature $T_s$ (°C)	Sputtering time $t_d$ (min)	<i>Co</i> -target power $P_{Co}$ (W)
A	150(2)	15,00(1)	0
A2	20(4)	15,00(1)	0
B	150(2)	15,00(1)	20,00(5)
C	150(2)	15,00(1)	40,00(5)
D	150(2)	15,00(1)	60,00(5)
E	150(2)	15,00(1)	40,00(5)
F	150(2)	15,00(1)	40,00(5)
G	150(2)	20,00(1)	40,00(5)
H	150(2)	30,00(1)	40,00(5)
L	20(4)	15,00(1)	40,00(5)
M	50(3)	15,00(1)	40,00(5)
N	100(3)	15,00(1)	40,00(5)
O	150(2)	15,00(1)	40,00(5)

We need to find an optimal configuration to have a tetrahedral position of *Co* in the *ZnO*

---

matrix. As is well known, diffusion and species mobility constants are higher when the temperatures rise. For this reason, higher temperature exposure was the best option to give the system the necessary energy to reach the stablest configuration. Once finished the deposit, was studied the effect of an *in situ* annealing on two samples (one fabricated at room temperature  $\sim 300$  K - and another at 423 K). We analyzed the magnetic properties to determine if the annealing thermal energy was necessary to have optimal conditions to achieve a *ZnO* based DMS. Possible *Co* magnetic contributions were observed in a competition with the *ZnO* diamagnetic nature only when the samples were annealed. For this reason, all samples were annealed *in situ* by two hours at 473 K.



### 3. $Zn_{1-x}O_yCo_x$ Density Functional Theory approach

Among the II-VI semiconductors, the  $ZnO$  is a material with wide bandgap energy ( $E_g = 3,35$  eV) that has a transparent characteristic in the visible, then once doped with transition metals would be an interesting ferromagnetic material. Wurtzite is the most stable  $ZnO$  crystalline structure (hexagonal, with  $a = 3,25$  Å and  $c = 5,12$  Å) [119]. This oxide has naturally an electron conductivity ( $n$ -type) but with certain doping types,  $p$ -type conductivity can be induced [29]. Besides, the possibility of inducing room-temperature (RT) ferromagnetism (FM) in Diluted Magnetic Semiconductors (DMS) based on  $ZnO$  have attracted plenty of interest [25, 120–122]. Since Dietl predicted a Curie temperature ( $T_C$ ) above room temperature in  $Mn$ -doped  $ZnO$ , DMSs based on this semiconductor had raised great interest [25], being emerged as a leading candidate for spintronic due to its special semiconductor characteristics and spin properties.

Cobalt doped  $ZnO$  has become a focus of attention as one of the possible doping types due to its high Curie temperature reported, even of up to room temperature (RT) and a controllable FM ordering [123, 124]. Coupled with  $ZnO$  current and well-studied electrical and optical characteristics, the addition of a controllable magnetism will make it a technologically novel and attractive material. Previous reports have shown that at  $Co$  concentrations of less than 10% there is a substitution between Cobalt and Zinc atoms, with a +2 charge state [125].  $Co(II)$  (with  $3d^74s^0$  configuration) as Zn-substitutional in the wurtzite structure results stable and occupies a fourfold tetrahedral coordination site, causing that the  $t_d$  crystal field splits the  $Co - 3d$  states into lower  $e_d$  and upper  $t_{2d}$  states (typically on the order of  $1,5 - 2,0$  eV), resulting in a spin-oriented occupation with a local  $Co$  magnetic moment close to  $3\mu_B$ . [126].

However, experimental reports on  $ZnO$ -based DMS have been highly conflicting in reproduce these predictions. It was found to be paramagnetic [86, 127, 128], and in some situations were reported ferromagnetism in some samples [90, 120], with a strong dependence on methods and conditions of synthesis [129, 130]. Magnetic ordering seems to be susceptible to the chemical ordering of the  $Co$  dopant and other impurities such as interstitials and vacancies in the lattice. Spintronic applications [82] usually require that ferromagnetism has an intrinsic origin, *i.e.*, not from magnetic Cobalt clusters or impurity phases [131].

One way to study the *Co*-doped FM materials is based on the  $3d$  band coupling [132]. How *ZnO* is a wide gap semiconductor, minority spin *Co*  $t_{2d}$  states would place within the band-gap, reported from *ZnO : Co* optical and magnetic measurements *ZnO : Co* [125, 133, 134]. Surprisingly, once again some previous theoretical and experimental studies are not in agreement [23, 135, 136]. It has been made clear that different reports disagree, even among similar models and techniques. It is not clear what is the best setup in *Co*-doped *ZnO* or the most accurate model to explain the magnetic interactions.

In this chapter, we studied the role of oxygen vacancy ( $V_O$ ) near cobalt impurities in the *ZnO* matrix, trying to achieve an optimal configuration for the room temperature ferromagnetism that have been reported by experimental studies [90, 120, 129, 130]. Different configurations were performed, varying the positions and concentrations of *Co* and  $V_O$ . The stability of these systems was determined by the formation energy calculations. To understand the magnetic ordering, the DOS and spin-charge spatial distributions were compared between the most stable configurations. The idea to have interplaying charge and spin degrees of freedom accommodated into a semiconductor material at room temperature is expected to explore novel physics and new devices, such as spin valves.

### 3.1. State of the art: Computational approaches

Several computational methods based on density functional theory have been extensively used for study the electrical, structural, optical, and magnetic properties of *ZnO* [137]. It is well known that DFT conventional methods produce underestimated value of the energy bandgap ( $\sim 0,7 - 1,0$  eV) compared with the experimental value ( $\sim 3,4$  eV). The error has been discussed in the literature, for this and other larger electronic  $d$  and  $f$  orbital systems [138, 139]. In the last two decades, several approximations, have been proposed for a better result on the electronic localization of those electrons. Besides, these corrected approaches have also been successfully used in the calculation of defects, surfaces, and interface properties [140, 141]. Although this error, the spin-charge distribution is well estimated under conventional DFT methods and it is been frequently discussed in most published articles [137, 142–144]. GGA+U, as bandgap correction method [145], introduces an effective Hubbard  $U$  to count for the  $d$  electrons of transition metals to improve the estimation of the bandgap. The corrected bandgap as a function of the Hubbard  $U$  has been shown that various  $U$  values give a consistent improvement of band gap for different phases of *ZnO*, for GGA [146]. Since GGA calculation is less computationally expensive than GGA+U, if we are not interested in band-gap calculations, GGA is enough to have a first approach to the structure and magneto-electric properties.

Several theoretical studies based on ab initio methods have focused on the study of hexag-

onal shape  $ZnO$ . Even though there are a lot of studies about its other crystal structures, including rocksalt,  $CsCl$  structure type, zinc-blend, and wurtzite have been reported [147, 148]. The thermodynamically stable phase of  $ZnO$  at ambient condition is the hexagonal structure (Wurtzite) which is fourfold-coordinated. The zinc-Blend structure is another similar structure that can be stabilized by the epitaxial growth of  $ZnO$  on cubic substrates. The properties of each lattice are well studied, theoretically and experimentally. For the wurtzite cell, the theoretical  $a_0(c_0)$  constant takes values around  $3, 1\text{\AA}-3, 3\text{\AA}(5, 10\text{\AA}-5, 30\text{\AA})$  [146, 149, 150], while the experimental value in pure-wurtzite systems has been reported as  $3, 250\text{\AA}(5, 204\text{\AA})$  [145].

## 3.2. Theoretical aspects

The foundation of the first-principles method is based on quantum mechanics description of the behavior of electrons and atomic nuclei [151]. The Schrödinger equation serves as the basic equation here, where the Hamiltonian operator consists of kinetic and potential energies due to the Coulomb interaction between electrons and nuclei:

$$\hat{H} = \sum_{I=1}^N \frac{P_I^2}{2M_I} + \sum_{i=1}^n \frac{P_i^2}{2} m_i + \sum_{i \neq j} \frac{e^2}{|r_i - r_j|} + \sum_{I \neq J} \frac{Z_I Z_J e^2}{|R_I - R_J|} - \sum_{ij} \frac{Z_I e^2}{|R_I - r_i|}, \quad (3-1)$$

where  $P_I$  ( $p_i$ ) are the momenta of ions (electrons),  $R$  ( $r$ ) represent the coordinates of ion (electron),  $Z$  ( $e$ ) is the charge of the ion (electron), and  $M$  ( $m$ ) are their masses.

Due to the complexity of the Schrödinger equation, it is almost impossible to be solved and would lead to uncontrollable computation in a system of multiple electrons. This is principally due to their interaction nature which each other, which leads to many-body problem [151, 152]. Several approximations are then developed to solve this. The first useful one is the well-studied Born–Oppenheimer approximation [153, 154]. The principal idea in that approximation is to separate the electron and nuclear motion [152]. This is because the mass of the nucleus is much larger than the electron's, and the nuclei are principally fixed particles. Uncoupling that, eventually enables the possible application of the Schrödinger equation in a complex system.

Hohenberg and Kohn(1964) [155] developed a couple of theorems that defined the electron density as a unique function for ground state energy of a system with  $N$ -electrons. Hohenberg-Kohn theorems have served as the basis for modern DFT. The first theorem stated that in a system with  $n$  interacting electrons, the many-body ground state wavefunction ( $\Psi_{(r_i \dots r_n)}$ ) of all electrons is a unique functional of the electronic density,  $\rho(r)$  [155]:

$$\rho(r) = n \int \dots \int |\Psi(r_i \dots r_n)|^2 dr_i \dots dr_n. \quad (3-2)$$

As the Hamiltonian equation comprised of the sum of several terms (electronic kinetic energy  $T$ , the attraction of electron-nuclear  $V_{Ne}$ , and electron-electron repulsion  $V_{ee}$ ), the molecular property based on these average variables is determined by ground-state electronic wave-function  $\rho_0(r)$ . So, the total energy can be calculated as the sum of average quantities. Now, considering  $v(r)$  as a function for nuclear potential energy for an electron at point  $r$ , the energy of the ground state is:

$$E_0 = E_v[\rho_0] = \bar{T}[\rho_0] + \bar{V}_{ee}[\rho_0] + \int \rho_0 v(r) dr; \quad (3-3)$$

the first theorem focus on the wave-functions and energy functionals. The second one allocates a minimum principle for density. It stated that the ground state energy of any trial electron density cannot be smaller than the true ground state system:

$$E_v[\rho_{tr}] = E_v \geq E_0 = E_0[\rho_0]. \quad (3-4)$$

After those theorems, a Schrödinger-like equation with a modified effective potential had been introduced, by adding a set of the independent-particle equation much easier to solve (Kohn and Sham [156]). This fictitious supporting system is used to resemble the true many-electron system, and write the energy as a numerical solvable set:

$$E_v[\rho] = \int \rho(r)v(r)dr + \bar{T}_s[\rho] + \frac{1}{2} \int \int \frac{\rho(r_1)\rho(r_2)}{r_{12}} dr_1 dr_2 + E_{XC}[\rho]. \quad (3-5)$$

$E_{XC}$  is known as the exchange-correlation energy that contains the correlation energy, exchange energy, Coulomb correlation energy, and self-interaction correction. No exact expression for this exchange and correlation ( $XC$ ) potential is known [157]. So, to ensure the accuracy of DFT calculation an approximation is thus embodied. There are a lot of approximations that have been developed (LDA, GGA, meta-GGA, and hybrid functional). Each of these conveys different definitions and approaches. Usually, the LDA and GGA are the ones widely used in the DFT calculation of the  $ZnO$  system [144, 158, 159].

The idea of LDA is: for a given region of material with a slow varying in charge density, the  $XC$  energy at point  $r$  is only dependent on the particle density at that point,  $n(r)$  [160]. This  $XC$  energy must be similar to homogeneous electron gas ( $e^{hom}$ ) of the same charge density:

$$E_{XC}^{LDA} [n(r)] = \int n(r)e_{XC}^{hom} [n(r)] dr \quad (3-6)$$

Even with the new advances in material science, it has been successfully calculated the properties of different materials with predictive accuracy [157]. However, the localized characteristic in LDA has enabled the incorrect treatment of the electronic structure of certain materials, especially in a system with a strongly correlated structure [158, 161, 162].  $ZnO$  is an example of a strongly correlated structure owing to the full electrons at  $Zn - 3d$  state.

For this reason, generalized gradient approximation is more used in this system. This second approximation uses two variables instead of one, the electron density and its gradient:

$$E_{XC}^{GGA} = \int n(r) e_{XC}^{hom} [n(r), \nabla n(r)] dr, \quad (3-7)$$

also, some corrected functional functions have been developed in GGA formalism to include the contribution of exchange and correlation part [163, 164].

### 3.3. Methods and model

The spin density functional theory (DFT) was used with the generalized gradient approximation (GGA) as parameterized by Perdew, Burke, and Ernzerhof (PBE) for exchange-correlation functionals [163], as implemented in the VASP package [165, 166]. The electron wave functions were described using the projector augmented wave (PAW) method of Blöchl in the implementation of Kresse and Joubert [167]. For DFT calculations, two periodic orthogonal super-cells, with 16(8) and 36(18) formula units (single-cells) of  $ZnO$  were used, containing 32 (16) or 72 (36) atoms (Molecules), which have lattice vectors  $(0; \sqrt{3}a/2; 0)$ ,  $(3a/2; 0; 0)$ ,  $(0; 0; c)$  (see Fig. 3-1).

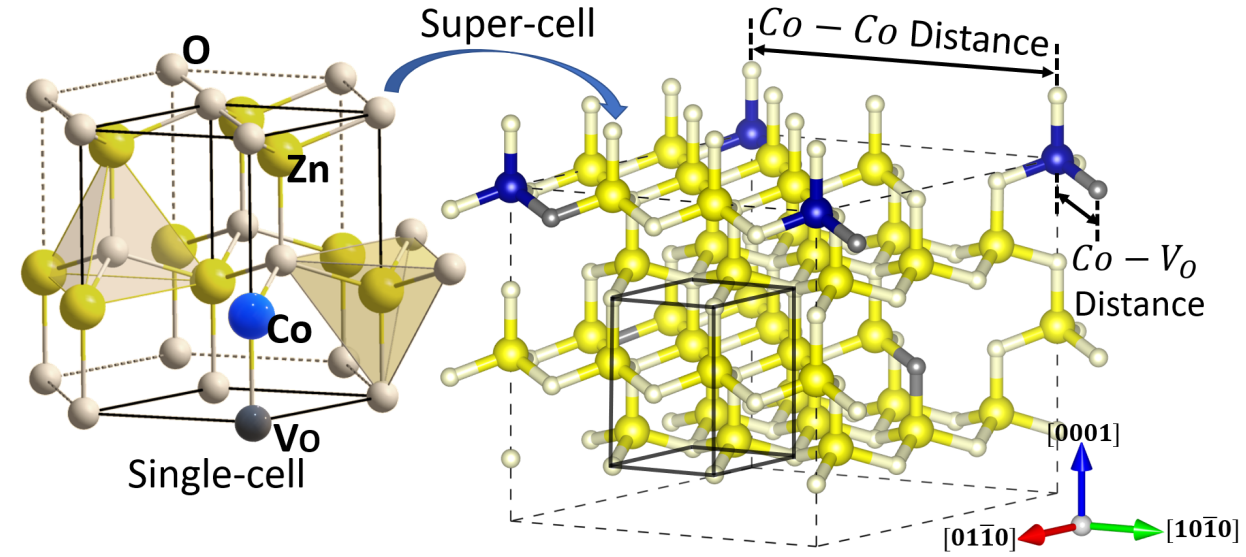


Figure 3-1.: Wurtzite single cell, with two different tetrahedrons, of  $Co$ -doped (Blue spheres)  $ZnO$  (left) and 3x3x2 super-cell (F-Configuration in Table 3-1). Large yellow (small whitish) spheres designate  $Zn$  ( $O$ ) atoms.

In all the different configurations performed (see Table 3-1), plane waves have been included up to cutoff energy of 520 eV, energy difference for ionic convergence was set to 1 meV and

electronic states were occupied with a Methfessel-Paxton smearing width of 0,20 eV in a real-space projection scheme, used for efficient computations.

super-cell	Single	Impurities				$Co - Co$	
	Cells (#)	Co (#)	Co (%)	Vo (#)	Vo (%)	Distance Å	Conf.
222	16	1	6,25%	0	0,00%	6,58(1)	A
		1	6,25%	1	6,25%	6,58(1)	B
		1	6,25%	2	12,50%	6,58(1)	C
332	36	1	2,77%	0	0,00%	9,87(1)	D
		1	2,77%	1	2,77%	9,87(1)	E
		1	2,77%	2	5,55%	9,87(1)	F
		2	5,55%	0	0,00%	$2\Delta_{Co-Vo}$	G
		2	5,55%	1	2,77%	$2\Delta_{Co-Vo}$	H

Table **3-1.**:  $Zn_{1-x}O_yCo_x$  systems studied (A-H configurations) at different  $V_O$  and  $Co$  composition, in 222 or 332 super-cells and its  $Co - Co$  characteristic distances.

To calculate the formation energy of each  $Co$ -doped and  $O$ -vacancy configuration. First, we carried out total energy calculations for  $Co$ -atom,  $Co$ -bulk,  $Zn$ -atom,  $Zn$ -bulk,  $O_2$  molecule, and  $ZnO$ -wurtzite, and then we calculated these energies for the  $Co$ -doped  $ZnO$  system. Formation Energy ( $E_f$ ) and Cohesive Energy ( $E_c$ ) were calculated as [168]:

$$E_{c,(f)} = \mu_{ZnO} - \mu_{Zn_{(2)}} - \mu_{O_{(2)}}, \quad (3-8)$$

where  $\mu_{ZnO}$  is the total energy per atom pair of  $ZnO$  compound,  $\mu_{Zn}$  is the isolated atom energy of  $Zn$  for  $E_c$  (energy per atom of bulk  $Zn$  for  $E_f$ ) and  $\mu_O$  corresponds to isolated atom energy of  $O$  for  $E_c$  (energy per  $O$  atom in the  $O_2$  dimer for  $E_f$ ).  $Co$ -doping and the formation energy calculations for impurities were performed using [168]:

$$E_F = E_{tot} - \left( E_{tot} [host] + \sum_i \eta_i \mu_i \right), \quad (3-9)$$

where  $E_{tot}$  is the total energy for the super-cell with impurities,  $E_{tot} [host]$  is the total energy of the host super-cell,  $\eta_i$  indicates the number of atoms type  $i$  that are added ( $\eta_i > 0$ ) or subtracted ( $\eta_i < 0$ ), and  $\mu_i$  is the chemical potential of the  $i$  species.

With the same computational parameters, previous calculations were performed with different kinds of impurities in the  $ZnO$  matrix (Oxygen vacancies, Zinc vacancies,  $Co_O$  substitution,  $Zn_O$  anti-site, and  $Co_{Zn}$  substitution). Also, combinations of these impurities

at different concentrations were studied. Figure 3-2 shows the formation energy of these configurations ordered from the lowest to the highest. Based on this, we can predict that is more probable to have one or another kind of impurity, at determining the energy. After that, the configurations were restricted to the Cobalt-Zn substitution and Oxygen Vacancies.

The absolute errors were calculated based on statistical dispersion of the data and er-

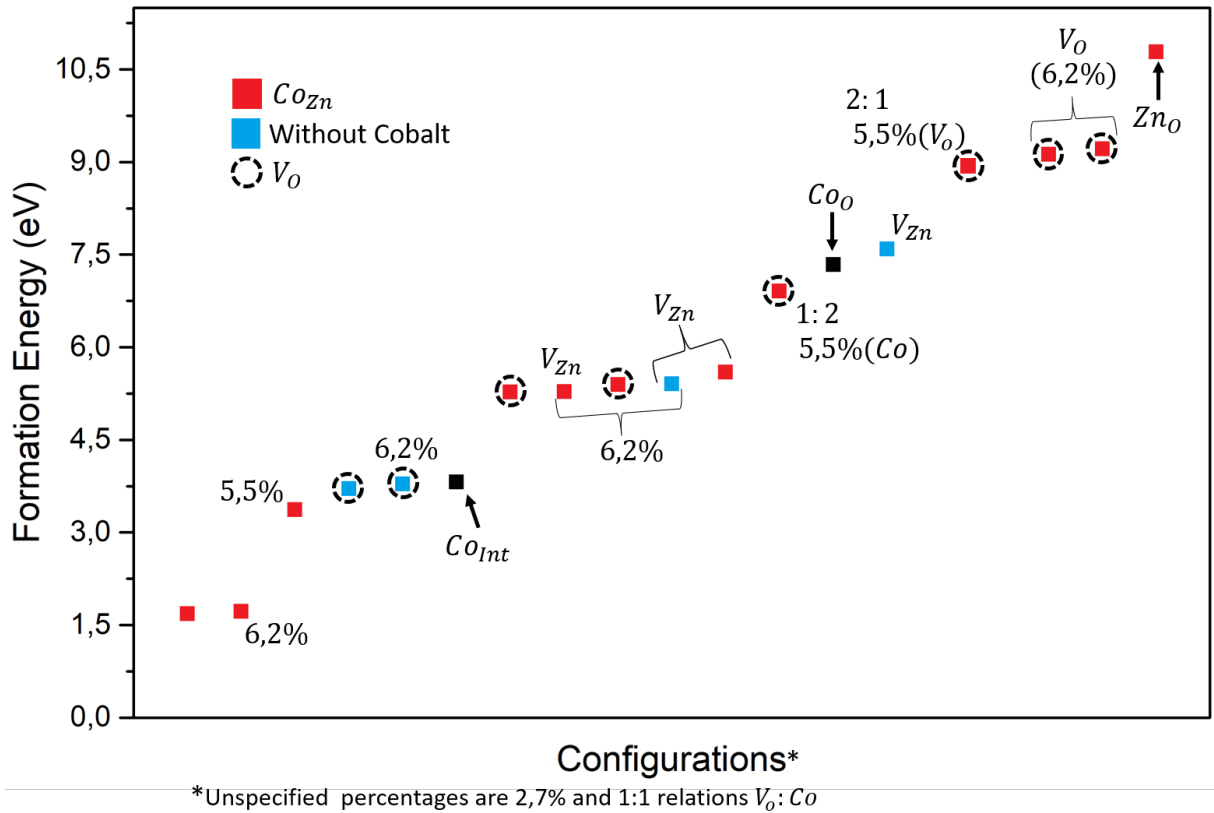


Figure 3-2.: Formation Energy for different impurities configurations in the  $ZnO$  matrix.

ror propagation, the number in parenthesis is the one-sigma ( $1\sigma$ ) uncertainty in the last two digits of the given value. The previous calculations and the corresponding values to undoped super-cell were according to previous reports. Our results  $E_c = -7,01(2)$  eV and  $E_f = -2,95(1)$  eV are in good agreement with theoretical ( $E_c = -7,69$  eV and  $E_f = -2,89$  eV) [169–171] and experimental ( $E_c = -7,52$  eV and  $E_f = -3,56$  eV) [172] results reported by other authors. However, we can observe that the GGA approach tends to underestimate the formation energy values. After determining the energies associated with undoped systems, it is necessary to determine, under our model and approximations, the most stable configuration for each type of doping,  $Co$  impurities and oxygen defects (Interstitial Cobalt,  $Zn$  and oxygen vacancies,  $Co$ -Oxygen and  $Zn - O$  antisites, and  $Co - Zn$  substitution at 2,78%, 5,56% and 6,25% with and without Oxygen vacancies). Once determined the

stability range of Oxygen vacancy doped in  $Zn_{1-x}O_yCo_x$  systems, we perform a series of simulations varying the shortest distance between Cobalt and  $V_O$ , at different  $Co$  concentrations (Table **3-1-B**, D, E, and H configurations). In the most stable  $Co - V_O$  system was added a second  $V_O$  at different positions (Table **3-1-C** and F configurations). After VASP simulations, using the VESTA software we analyzed the spin density distribution in different planes to show how the oxygen vacancies affect the magnetic distribution inside the structure. Spin density plots were analyzed in the range of  $4e^-/\text{\AA}^3$ .

## 3.4. Results and discussion

Our structural optimization calculations for  $Co$ -doped  $ZnO$  at a Cobalt concentration of 6,25% and 3,12% in  $Zn$ -substitutional positions, and a  $V_O$  concentration of 0%, 3,12% and 6,25%, reveal that the distance and the associate substitutional local symmetries have an important role in the structure stability. To study the effect of the oxygen vacancy ( $V_O$ ) on the structural, magnetic, and electric properties of  $Co$ -doped  $ZnO$ , in the eight configurations, different positions of oxygen vacancy were adopted. In Fig. **3-1** (right) the different configurations to oxygen vacancies in the super-cell were set varying the  $Co - V_O$  distance at different  $O$  positions. Different  $Co - Co$  distance configurations were also studied.

### 3.4.1. Effect of $Co - V_O$ distance in the $Zn_{1-x}O_yCo_x$ system

We studied the  $Co - V_O$  distance ( $\Delta_1$ ) replacing oxygen by vacancy at different positions, with a fixed  $Co - Co$  distance: 9,87(1)  $\text{\AA}$  (2,78% $Co$ ), 6,58(1)  $\text{\AA}$  (6,25% $Co$ ), and twice  $Co - V_O$  distance (5,56% $Co$ ). After calculated the most stable magnetic configuration ( $V_{O1}$  around 1,90(6)  $\text{\AA}$ ), we studied the effect of a second  $V_O$  at different  $Co - V_O$  distances ( $\Delta_2$ ) in 2,78%  $Co$  and 6,25%  $Co$  systems. (Fig. **3-3**-(b)). Fig. **3-3**-(c) shows the formation energy as a function of  $Co - V_O$  distance ( $\Delta_1$ ) for different  $Co$  concentrations, the stability of the structure is higher as  $\Delta_1$  decrease and all configurations have a magnetic moment in the range of 3,02(1)  $\mu_B/Co$ . When the  $V_O$  is added, the magnetic moment decrease as  $\Delta_1$  (Fig. **3-3**-(a)) and is always lower than the calculated without oxygen vacancies (dashed line  $\overline{\mu_T} = 3,131(1)\mu_B/Co$ ).

When the second vacancy is added, the effect in short distances (comparable with the first vacancy) differs according to the  $Co - Co$  distance. When it is shorter (6,58(1)  $\text{\AA}$  for 6,25%  $Co$ ) the total magnetic moment per cobalt ( $TMM/Co$ ) decreases as  $\Delta_2$ . In the other hand, for a lower Cobalt concentration (2,78%  $Co$ ) and a higher  $Co - Co$  distance,  $TMM/Co$  increases as  $\Delta_2$  decreases. However, when  $\Delta_2$  is at least twice  $\Delta_1$  in both cases  $\mu_T/Co$  trends to the one-near  $V_O$  case with  $TMM/Co \sim 3,00(2)\mu_B$ , giving us an effective range for the second vacancy. Taking this as a start point, we can analyze the effect of one vacancy near to the cobalt atoms and assume that other far vacancies do not contribute in a significant way.



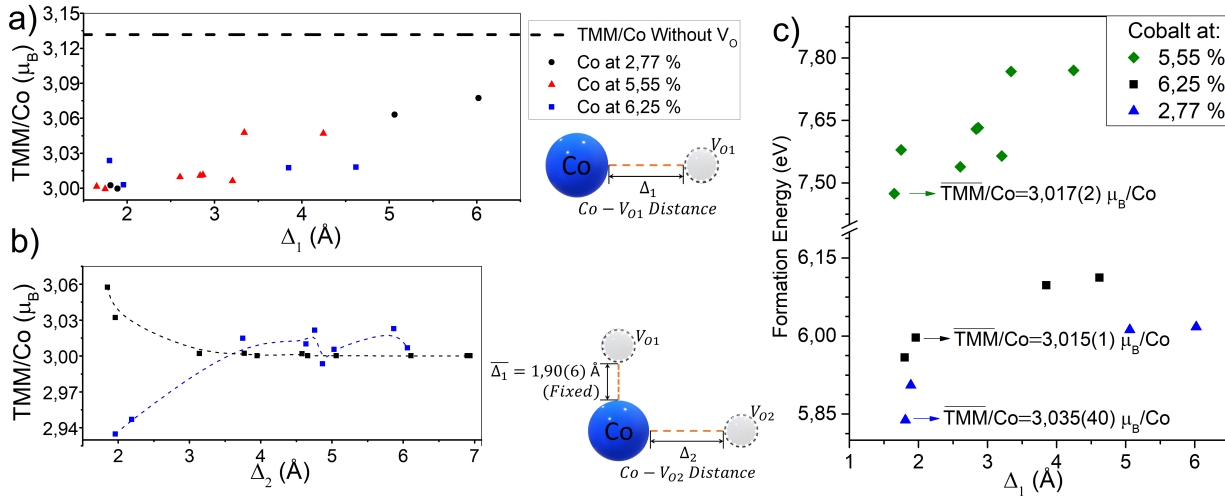


Figure 3-3.: Effect of  $Co - V_O$  distance in (left) the total magnetic moment per Cobalt atom in (a) 1 : 1 ( $Co : V_O$ ) ratio, (b) 1 : 2 ratio and (c) Formation energy, for different cobalt concentrations and one  $V_O$  per super-cell.

Different atoms contribute to the  $TMM/Co$ , as expected, Cobalt mostly, but also, a lower contribution from the semiconductor matrix and the electrons located in the interstitial region. Fig. 3-4-(a) shows the average contributions of these species. The contributions per Cobalt orbital (Fig. 3-4-(b)) is mainly by  $d$  orbital (97,67%) where no-compensated electrons are located. The lower contributions of  $s$  and  $p$  orbitals allow a  $d - d$  coupling between adjacent Cobalt or a possible mediated magnetic interaction for electrons trapped in the oxygen vacancies [126].

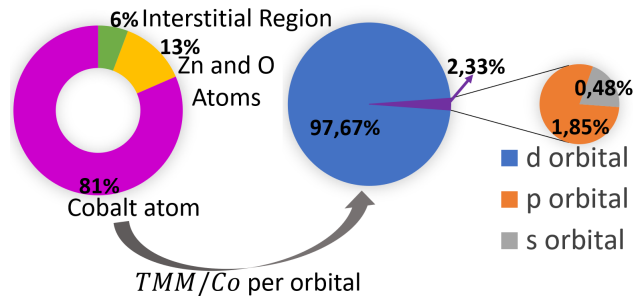


Figure 3-4.: (a) Average contribution from  $Co$ , interstitial region,  $Zn$  and  $O$ , to the total magnetic moment per Cobalt atom and (b) contributions per orbital into the Cobalt atom.

In a Heisenberg model, the formation energy difference between ferromagnetic (FM) and

antiferromagnetic (AFM) configuration ( $\Delta E_f$ ) is given by [173]:

$$\Delta E_f = (E_f^{AFM} - E_f^{FM}) = J_0 S_T (S_T + 1) \quad (3-10)$$

and Curie temperature, following [174]:

$$k_B T_C = \frac{3}{2} J_0 S(S + 1) \quad (3-11)$$

We carried out ferromagnetic and antiferromagnetic configurations, at 5,56%  $Co$  and then we add  $V_O$  at 2,78%, to study the difference in the formation energy and its respective exchange constant as a function of the  $Co - Co$  distance (Fig. 3-5). The stabilization on the magnetic configuration increases as  $\Delta E_f$ , a positive(negative) value indicates that FM(AFM) configuration is preferred by the structure. When Oxygen vacancies are not in the structure, the energy difference is the smallest, and the most stable structure corresponds to an antiferromagnetic configuration. In almost all the cases, it is shown that the  $V_O$  stabilizes the ferromagnetic configuration, reaching a maximum  $T_C = 374,88(5) K$  where the two cobalt atoms are closer. The addition of  $V_O$  is a mediator in the high-temperature ferromagnetism but its effect on the electronic distribution around the Cobalt atoms remains a question.

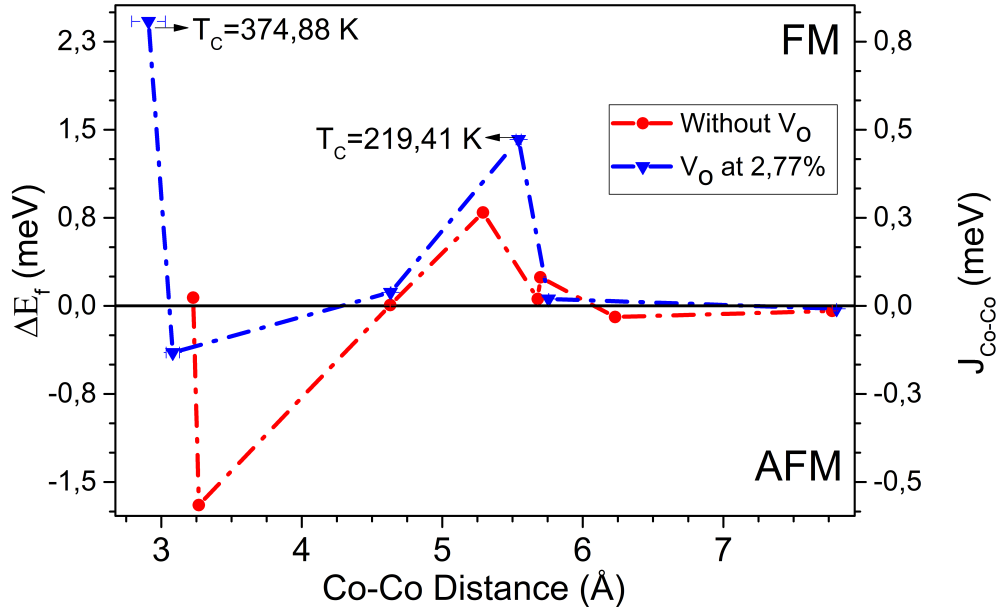


Figure 3-5.: Difference between Ferromagnetic ( $E_{\uparrow\uparrow}$ ) and Anti-ferromagnetic ( $E_{\uparrow\downarrow}$ ) formation energies as function of the  $Co - Co$  (5,56%  $Co$ ) distance for configurations with and without  $V_O$ , the right axis shows the exchange constant  $J_0$  in the model Eq. 3-10.

### 3.4.2. Effect of the $V_O$ on the magnetic and electronic properties of $Co$ -doped Zinc oxide

Also, we have studied the electron spin-density (up and down) in  $Co$ -doped  $ZnO$  with and without oxygen vacancies for the most stable energetical configurations. First, we observe the spin distribution in different crystallographic planes for the case of oxygen vacancy near the Cobalt impurity. We focused on the planes that contain the oxygen vacancy, Cobalt, and other Oxygen atoms near the Cobalt atom. Fig. 3-6 shows the plane  $(\bar{1}2\bar{1}0)$  section of two comparative scenarios: The right shows a Cobalt atom (blue sphere) in a tetrahedral Zn position with four oxygen (two red spheres in the plane) and the left shows the same configuration but with an oxygen vacancy in this plane; Zn atoms are represented by a silver sphere.

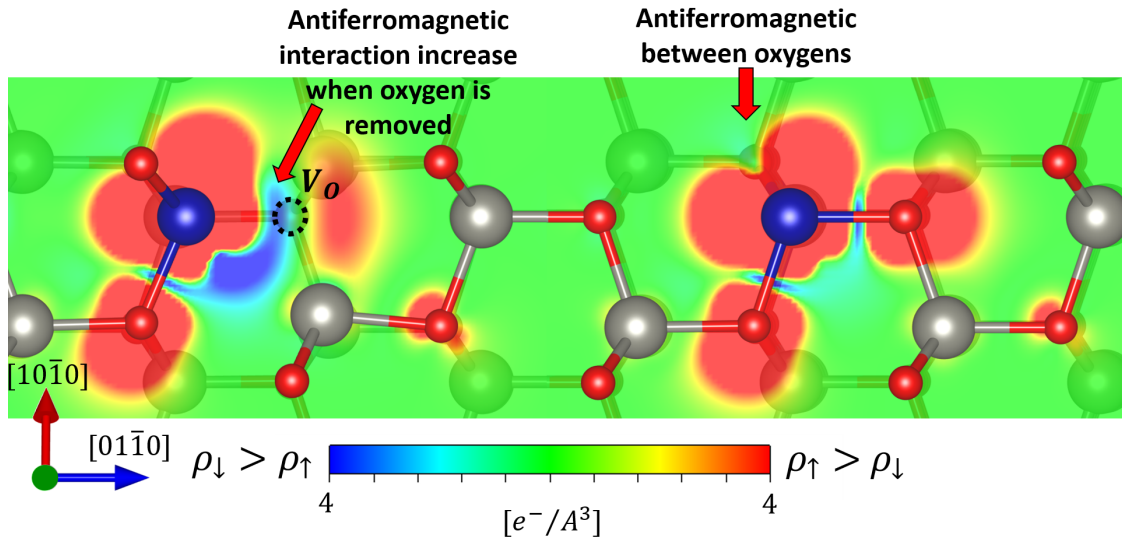


Figure 3-6.: Spin density difference ( $\rho_\uparrow - \rho_\downarrow$ ) section (plane  $(\bar{1}2\bar{1}0)$ ) of Cobalt doped  $ZnO$  with  $V_O$  (left) and without  $V_O$  (right).

The right side of Fig. 3-6, shows a slightly higher  $\rho_\downarrow$  in the middle of two oxygen atoms, those zones are present always between any couple of oxygen atoms. Also, on the left side, it is possible to observe a bigger compensated electrons zone (blue-red zone), which explains the lower total magnetic moment when  $V_O$  is added. In the  $V_O$  site there are  $\rho_\downarrow$  and  $\rho_\uparrow$  contributions, giving a full-compensated (equal  $\rho_\downarrow$  and  $\rho_\uparrow$  contributions) spin-density zone. This increment of the antiferromagnetic zones can be explained by the non-coupled electrons from the oxygen removed, that have an exchange interaction ( $J_0 < 0$ ) with the Cobalt electrons.

When the second Oxygen vacancy is added, as we previously discussed, there is a maximum range to affect the total magnetic moment per Cobalt. Figure 3-7 shows a transverse section of the spin density difference in the lower- $\Delta_2$  C-configuration. The plane  $(\bar{1}2\bar{1}0)$  contains both  $V_O$  as the rightest part of the figure shows. In the  $\rho_\uparrow - \rho_\downarrow$  plot can be observed

the difference in the spin distribution when the two vacancies are added (left). Contrasting with the one- $V_O$  part (left part Figure 3-6) there is a new zone of positive spin difference, so the total magnetic moment per Cobalt should increase, as we expected since Figure 3-3 was discussed. Also, the iso-surface (outside-left) shows three negative zones (cyan zones) that have antiferromagnetic interactions with the positive distribution (purple zones) from the Cobalt atom and the electrons of the interstitial region.

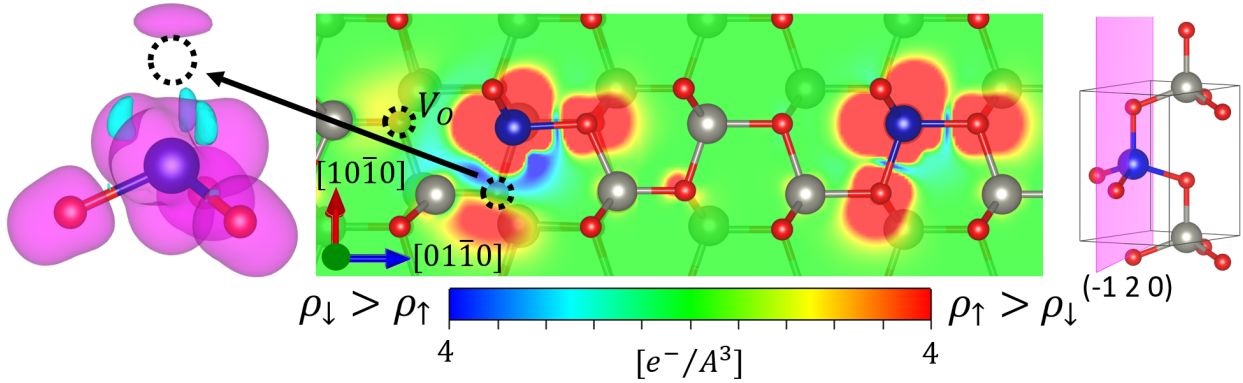


Figure 3-7.: Spin density difference ( $\rho_{\uparrow} - \rho_{\downarrow}$ ) section (plane  $(\bar{1}2\bar{1}0)$ ) of Cobalt doped  $ZnO$  with 12,5% of  $V_O$  - $1_{Co} : 2V_O$  relation-(left) and without  $V_O$  (right).

We analyzed the antiferromagnetic and ferromagnetic cases when the two Cobalt atoms are closer; Fig. 3-8 shows a cut section (plane  $(11\bar{2}0)$ ) of these configurations with (left) and without (right) oxygen vacancies. In the ferromagnetic cases, when  $V_O$  is added, we have a lower  $\rho_{\downarrow}$  increment than the previous case, but the  $\rho_{\uparrow}$  zone decreases. This is easier to see in the iso-surfaces representation (Outer), where only the extremes of the scale are showed. This resulted in an average total magnetic moment per Cobalt decreasing (from  $2,561(1)\mu_B$  to  $2,481(61)\mu_B$ ) due to the  $V_O$ , with proportionality between  $TMM/Co$  and  $Co - Co$  distance increase.

In the antiferromagnetic case, we have an average total absolute magnetic moment per Cobalt of  $\overline{|TMM/Co|} = 2,55(1)\mu_B/Co$  without Oxygen vacancies and  $\overline{|TMM/Co|} = 2,46(7)\mu_B/Co$  with  $V_O$ . The spin-density-difference zones (Fig. 3-8-(a)) result in a compensated distribution, where is visible an antiferromagnetic interaction inside the shared Oxygen, and between this Oxygen and Cobalt neighbors. Once again, the effect of the  $V_O$  is easier to observe in the iso-surface representation (Fig. 3-8-(a)-outer), where the oxygen zone is wrapped by compensated distributions, but when  $O$  is removed, the  $\rho_{\uparrow}$  and  $\rho_{\downarrow}$  spin densities are getting closer to the opposite Cobalt, letting a compensated electrons  $V_O$  zone.

Now, we are particularly interested in the DOS distribution near the Fermi level. DOS provides physical insight into how the interaction of  $Co$  impurities and  $O$  vacancies on  $ZnO$

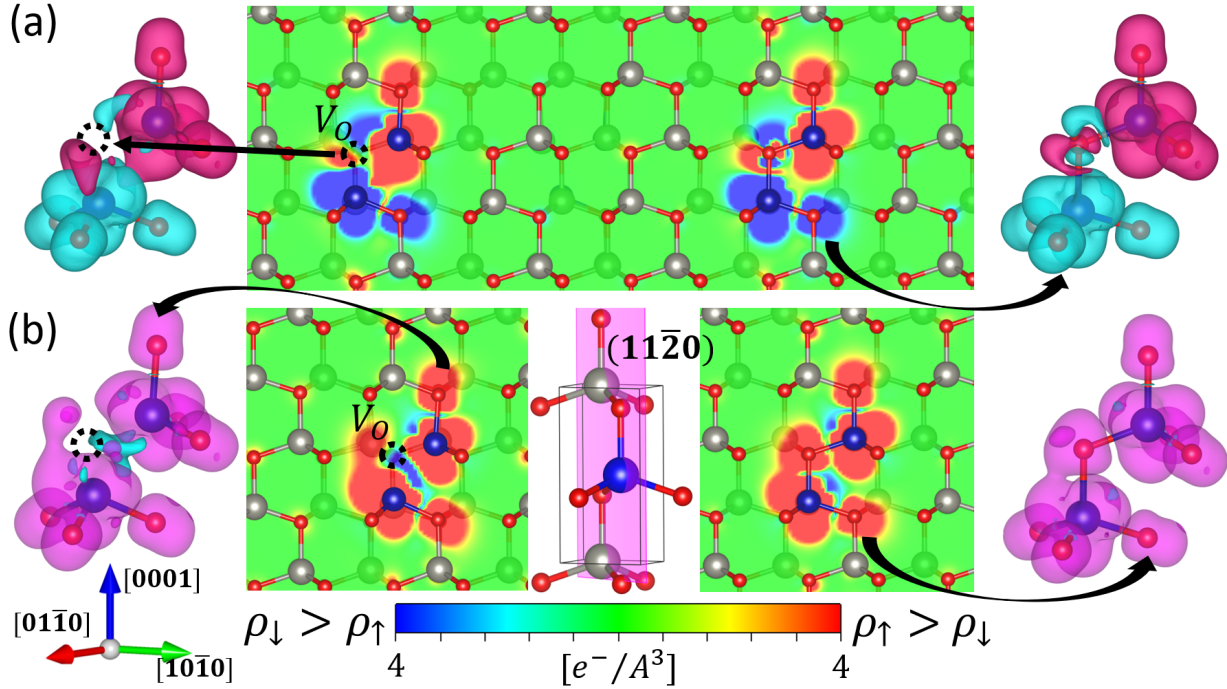


Figure 3-8.: Spin density difference ( $\rho_{\uparrow} - \rho_{\downarrow}$ ) section (plane  $(11\bar{2}0)$ ) and iso-surfaces (outer) of (a) Antiferromagnetic and (b) ferromagnetic configurations. Cobalt doped  $ZnO$  with  $V_O$  (left) and without  $V_O$  (right).

occurs, and how these interactions can generate induced magnetism. The total density of state (TDOS) and the partial density of state (PDOS) of the  $3d - Co$ ,  $2p - O$ , and  $3d - Zn$  orbitals were calculated in the ferromagnetic most stable configuration with (Figure 3-9-(b)) and without  $V_O$  (Figure 3-9-(a)).

Previously we showed that the addition of  $V_O$  results in a decrease of the  $TMM/Co$ , but with a more stable structure. PDOS statistical analysis showed that the largest PDOS contributions in  $Co$  and  $O$  are  $d$  (87(2)%) and  $p$  orbitals (71(1)%), respectively. Based on that, a  $p-d$  coupling is the best fit model to explain the magnetic behavior of the structure. Comparing the PDOS of  $Co$  and  $O$  in structures without  $V_O$  with the most stable  $Zn_{1-x}O_yCo_x$  structure, we can observe extra spin-down states appear in the  $O$ -PDOS (Fig. 3-9-b).

We observed below, on, and above the Fermi level, some impurity energy-level states in the spin-minority region (TDOS in Figure 3-9-(a)) caused mainly by  $3d - Co$  states. Compared with the majority spin region where there are no states, it shows a high polarization of spin induced by the  $Co$  impurity, indicating that the system is nearly half-metallic. Concerning the PDOS of the  $3d - Co$  orbitals, near and below the Fermi level in the minority spin region, this area is divided into four parts, forming peaks of energy bands that indi-

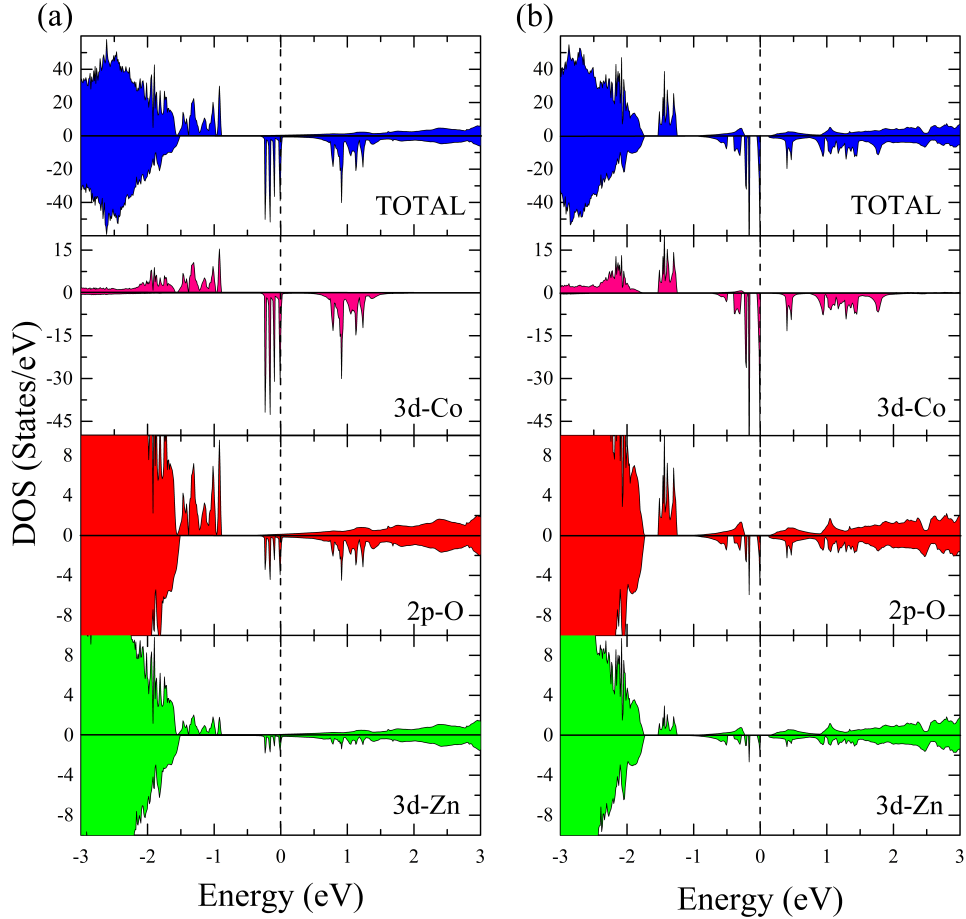


Figure 3-9.: Total DOS and PDOS ( $Co$ ,  $O$  and  $Zn$ ) of most stable structures in Ferromagnetic configuration with 5,56% of  $Co$ , (a) without  $V_O$  and (b) with  $V_O$  at 2,77%. The zero of the energy has been set at the Fermi level, as indicated with dashed lines. The values of the positive (negative) states correspond to the majority (minority) spin regions.

cated localized states. These peaks overlap with four others of lower height, corresponding to the  $2p - O$  orbitals. On the other hand, five peaks of unoccupied bands appear above the Fermi level in the minority spin region, caused mainly by states located in an energy range of 0,75 and 1,25 eV. Once again there is an overlap with the other five lower height peaks, corresponding to the  $2p - O$  orbitals. All these characteristics present in the PDOS suggest a strong hybridization between the  $3d - Co$  and  $2p - O$  orbitals, inducing magnetization in the  $Co$  atom as well as in the neighboring  $O$  atoms, as was observed in the spatial-spin distribution (Fig. 3-6). These results are in agreement with those reported by *González-García et. al.* [175]. In Fig. 3-9-(b), compared to the TDOS of Fig. 3-9-(a), the states are modified due to the  $O$  vacancy. Below and above the Fermi level, in the minority and majority spin regions, extra energy states that emerge in  $3d - Co$ ,  $2p - O$  and  $3d - Zn$  can

be seen. These states are not exhibited in the PDOS of the  $3d - Co$ ,  $2p - O$  and  $3d - Zn$  in figure **3-9**(a), which suggests that there is a charge transference when the  $O$  atom is removed. So, there could be loose bonds in the structure, which are redistributed causing a charge transference toward its first and second neighboring atoms. Due to the presence of  $2p - O$  and  $3d - Zn$  states near below and above the Fermi level in the majority spin region, the spin-polarization is reduced and the total magnetic moment per cobalt decreasing. We can see this behavior in the previous spin density plots (Fig. **3-6** and Fig. **3-8**), where there is a lower increment of  $\rho$  when  $O$  vacancy is added.

However, in the  $3d - Co$  states, the new states introduced in minority spin regions above the Fermi level increasing the local magnetic moment of  $Co$  atoms. Below the Fermi level in the minority spin region, the states become more localized and the Fermi level passes through a small part of the impurity states maintains the nearly half-metallic behavior. Given that the  $Co - Co$  distance is large enough to ignore the direct coupling between them (see Figure **3-8**(outer)), and according to the Bader analysis, there is an appreciable charge transfer between the two  $Co$  atoms that could be mediated through  $O$  vacancy. The direct exchange interaction  $d - d$  between the  $Co$  atoms could explain the stabilization of ferromagnetism in this compound. These results are very similar to and consistent with those reported by *Walsh et. al.* [126]. These results indicate that  $Co$ -doped  $ZnO$  can be used as a potential diluted magnetic semiconductor in spin-valve devices [176,177].



## 4. Structural and morphological characterization of Cobalt doped $ZnO$

Spintronic materials are characterized by controlling and having both, electrical and magnetic, properties [18]. To achieve a functional, optimal, and reliable spintronic it is necessary to have control of its structure.  $ZnO$  structure has been studied for a long time, and as it was mentioned above, the Wurtzite structure is the most stable. Also, it was checked that the  $Co_{Zn}$  substitution is possible and it is not too expensive energetically.

The experimental study of  $Co$ -doped  $ZnO$  thin films starts in this chapter. Here, several properties related to the thin-film structure are studied. First, a brief state of the art is reviewed to have an accurate background of the reported structural properties of  $ZnO$ . Then, some experimental aspects are aborded about the characterization techniques used along with all the technical details. Finally, results are presented following the process to identify the structural properties as a function of the synthesis parameters.

### 4.1. State of the art: Structural and morphological properties

Using the sputtering as a synthesis technique, there are several reports of  $ZnO$  and a few less about  $Co$  doped  $ZnO$  [178–180]. During the last few years, it has received great attention to solving the environmental pollutants issues because of its low cost and nontoxic nature [181, 182]. Hammad et al. [183] have successfully shown the change in structural characteristics of  $ZnO$  by  $Co$  doping, and when no extra peaks were found related to cobalt metal, cobalt oxide, and any other  $Zn - Co$  phases, it is suggesting that the doped  $Co$  ions are primarily incorporated into the  $ZnO$  lattice [180, 184]. The change in the principal  $ZnO$  peak shifted towards the higher or lower diffraction angle with the Cobalt concentration is attributed with replacement of  $Co^{2+}$  ion of radius (0,56 Å) with the  $Zn^{2+}$ (0,60Å) in the  $ZnO$  lattice [185–187]. Also, it is reported that the intensities of the peaks planes changed at different Oxygen pressure, which also suggested the incorporation of the  $Co^{2+}$  ion with the  $Zn^{2+}$ ions [182].  $Co$ -doping slightly decreased the lattice parameters of the  $ZnO$  nanocrystals, inferring that, the  $Co^{2+}$  ions were systematically substituted by  $Zn^{2+}$  ions without changing the crystal structure [184, 188, 189]. Also, the FWHM of the  $Co$ -doped  $ZnO$  was found to be narrower than that of the undoped sample, suggesting that  $Co$ -doping improved



the crystallinity of the *ZnO* nanostructure [178, 189–193]. Cobalt peaks are reported usually in concentrations up to 15%, where peaks near to  $44^\circ$  are reported [98, 194]

The surface roughness of the reported films was increased with the Cobalt [180]. Formation of islands was observed with the introduction of *Co*-metal into the *ZnO* thin films. This is usually attributed to the grain boundary pinning effect [195]. Also, the roughness of the samples increases with the *Co* target power in sputtering reports [180]. Formation of nanorods by sputtering is reported when the *Co* concentration increase and a strong dependence of the temperature deposit on these nanostructures [178, 196]. Some surface chemical composition of the pure *ZnO* and *Co* : *ZnO* thin films at different watt power have been investigated through XPS survey scan [180]. The carbon detected in these samples is attributed to the surface contamination during the sample transfer from chamber [197]. Higher concentration of Cobalt ( $> 50$  W in the Cobalt target) results in secondary phases detected only by XPS technique [180, 195, 198–204].

After this brief report review, it can be concluded that the *Co* concentration, the substrate temperature, and chemical nature are the most relevant parameters in the structural and morphological properties of the *Co* : *ZnO* samples.

## 4.2. Experimental aspects

There are some experimental techniques involved in this chapter: a profilometer to study the thickness of the thin films, an X-ray diffractometer for the structural properties, an Auger spectroscope to study the atomic composition of the samples, and, for the morphological characterization, an electron microscope and an atomic force microscope. Here, the fundamentals of each of these techniques will be briefly explained.

The X-ray diffraction technique consists of a compositional and structural method that allows not only the identification of the composition of mono or polycrystalline material but also its crystalline phases, crystalline structure, preferential orientation, etc. It consists of bombarding a sample with ionizing radiation (highly energetic) at different angles and detecting the reflected radiation from the sample to interpret the angles at which constructive interference exists [205]. X-ray production is a consequence of the deceleration of electrically charged particles [206]. In this case, emission occurs when highly energetic electrons collide against a target given that the kinetic energy of the incident particles is very high. As a consequence, these particles can penetrate the inner energy levels of the atoms present in the target and then displace the electrons located in the K orbitals, therefore, leaving a vacancy on the first energy level, which will be occupied by an electron of the outer orbitals (L or M).

When an electron undergoes a sudden decrease in its energy, dropping from a higher en-

ergy level to a lower energy level inside the atom, a photon with the characteristic frequency of X-ray radiation will be emitted from it, the energy of this photon is characteristic for every material. Once the highly energetic photons are produced, they will pass through a collimator and a monochromator to guarantee that the incident radiation is as coherent as possible; this is important because the diffraction would not be detected from the sample if the incident wave is not in the same phase.

When the X-rays reach the sample, two non-mutually exclusive physical phenomena take place. The first is the emission of X-rays by photonic incidence, and the second one is the X-ray diffraction process. The most relevant physical process in this technique constitutes the X-ray diffraction: every monocrystalline material can be considered as a large set of diffraction slits in which the line division distance corresponds to the distance between two adjacent planes of the crystalline lattice. Once the radiation reaches the planes of the material, these are diffracted at a determined angle; if two waves emitted from the sample are in the same phase, the maximum intensity condition, also known as constructive interference, will be achieved and therefore the detector will receive an abrupt increase in radiation.

The angle at which a diffraction peak is registered depends exclusively on  $\theta$ , therefore the entire set of angles in a crystal at which diffraction occurs depends only on the dimensional characteristics of its lattice and not on the positions of its atoms [207]. This implies that every X-ray diffraction pattern is characteristic of every material and therefore allows the unequivocal identification and characterization of it. In polycrystalline materials, there will be a higher number of angles at which constructive interference occurs, which results in a diffractogram exhibiting more peaks. In amorphous materials, compositional characterization is not possible with this technique due to a lack of a large-scale periodic structure inside the material, which will not allow the diffraction between planes.

Auger electron spectroscopy (AES) provides compositional information of the first atomic shells, due to the interaction of high-energy electrons with the surface of a material. When an incident electron interacts with an atom, it can generate ionization from an internal level which, when relaxing, fills the vacancy with an electron from an external level. The released energy can be taken up by an electron from the same shell or another outer shell, producing the emission of an Auger electron or emitting a photon [208]. The energy of the Auger electron depends exclusively on the energies of the atomic levels of its host atom. This Auger energy is characteristic of each atom and allows the direct identification of the element, even if the identified Auger electron comes from the valence band [208].

The Auger process is most dominant for kinetic energies below 2000 eV and strongly decreases for higher energies where the fluorescence yield is increasing [209]. Therefore, the most predominant Auger peaks are the KLL transitions for elements with atomic numbers

from 3 to 14, the LMM transitions for elements 14 to 40, and the MNN transitions for the heavier elements [209]. Therefore, the line shape of the AES spectra is influenced by plasmon losses [210] and ionization loss, so that the ionization loss energy can change by modifying the energy of the primary beam [209].

Scanning electron microscopy (SEM) is a handy technique to identify the morphological characteristics of the samples. This technique is based on the theoretical relation proposed by De Broglie in 1924 in which he proved that an accelerated electron beam has an associated wavelength, involving that a potential acceleration of 60 kV or an 80 kV will exhibit wavelengths ranging from 0,005 to 0,0043 nm, respectively. As a comparison, when an optical microscope is used, assuming a wavelength of 500 nm, the limit for resolution is around 217,86 nm [211]; in an electron microscope, this value would be enhanced by at least three orders of magnitude, given the fact that the wavelengths of the particles used are 103 times smaller, this proves to show the major advantage of using a scanning electron microscope in material science for the identification of possible surface nanostructures on a sample instead of an optical microscope [211].

In a SE microscope, the emission of electrons is from a tungsten filament that is heated using an electric current which consequently emits electrons that are then accelerated using electric tension ranging typically from 5 kV to 30 kV; the temperature at which the filament starts the thermionic emission is around 2700 K, if a greater current is put through the filament, a greater number of electrons will be obtained, however, it may compromise the mean life of the filament.

The entire system must have high vacuum conditions ( $< 1mPa$ ) for the mean free path of the electrons to be enough to reach the surface of the sample. An increase in resolution is achieved by focusing the electrons in an extremely thin beam, which is made employing copper lenses along the column. Once the electrons reach the sample, they begin to interact with its surface causing several physical phenomena and particle emission [212], the latter process is of great importance for the morphological characterization because the emitted particles are the ones responsible for the obtaining of the micrographs. Here, three important emitted particles are relevant: secondary electrons, backscattered electrons, and characteristic X-Rays photons.

The secondary electrons are the particles ejected from the outermost regions of the material under study, these are valence electrons from the atoms that are ripped from them once the energy of the incident electron beam overcomes the ionization potential of an atom. Given the fact that these are low energetic particles (inferior to 50 eV), only the outermost electrons can be emitted from the sample. After emission takes place, these electrons are detected by the secondary electron detector coupled with a photomultiplier and an amplifier

that translate the different intensities into an image on a computer. These electrons are useful for the study of surface topography.

Backscattered electrons are particles directly coming from the incident beam, but reflected after interaction with the surface of the sample, changing energy. These are reflected from deeper regions of the sample, not only from its surface, and are more sensitive to the chemical composition of the sample: The greater the atomic number ( $Z$ ) of an atom inside the material, the greater the quantity of emitted backscattered electrons; therefore, given that the detector assigns a different brightness to different received intensities, the areas with heavier elements will appear brighter in a micrograph, whilst the areas with smaller  $Z$  numbers will appear more opaque. The detector of backscattered electrons allows not only a topographical, but also a compositional study of the sample.

The characteristic X-ray photons are emitted by the standard process, when an incident electron beam interacts with a sample, this radiation is captured by an X-ray detector and allows the compositional characterization of the material employing the energy-dispersive X-ray spectroscopy (EDXS) technique. The interacting layers in this process depend on the energy of the incident beam, and if the sample is too thin, there can be some overlapping with the substrate composition.

Atomic force microscopy (AFM) is a technique for topographic and morphological characterization. It works under the physical phenomena of electrostatic repulsion and Van der Waals attraction and it reaches atomic resolution. The measuring process consists basically of scanning the surface of the sample with a probe placed on a cantilever (at a 10 Å separation), detecting any change in its surface through the movement of a light beam coming from a laser, whose reflection from the cantilever points towards a photo-detector that allows the collection of the feedback of the topography in the material. The probe is usually made of silicon nitride ( $Si_3N_4$ ), and the cantilever itself generally is made of pure silicon. An ideal probe should be one atom thick to guarantee a perfect resolution, however, commercial probes have lengths of around 3 to 6  $\mu\text{m}$  with a radius of 15 to 40 nm, which still imply resolutions of up to 0,1 nm. It can operate in three separate modes: Contact mode, non-contact mode, and tapping mode [213].

The tapping mode is the middle point between contact and non-contact modes; when the contact mode is applied to a sample, the tip oscillates all over its surface at small amplitude, however in this process, because of the adhesive forces of the material under study, the tip may result contaminated and the measurement distorted. The tapping mode eliminates this disadvantage because the tip is intermittently in contact with the surface and it oscillates with enough amplitude to prevent the tip from getting trapped under said adhesive forces. The result is that this mode provides the best resolution with minimum damage to the sam-

ple; in most cases, the non-contact mode is operated as a tapping mode instead.

There are other additional microscopy modes, changing the chemical nature of the tip, that can be configured into AFM equipment to evaluate other characteristics of a material, for example, evaluate the presence and distribution of magnetic domains in the surface of a sample.

Profilometry is a technique used to extract topographical data from a surface. This can be a single point, a line scan, or even a full three-dimensional scan. The purpose of profilometry is to get surface morphology, step heights, and surface roughness. This can be done using a physical probe or by using light. Stylus profilometers use a probe to detect the surface, physically moving a probe along the surface to acquire the surface height. This is done mechanically with a feedback loop that monitors the force from the sample pushing up against the probe as it scans along the surface. A feedback system is used to keep the arm with a specific amount of torque on it, known as the ‘setpoint’. The changes in the Z position of the arm holder can then be used to reconstruct the surface.

### 4.3. Methods and model

The samples were characterized from XRD measurements using X-ray diffractometer X’Pert Pro polycrystal PANalytical, equipped with a source of  $Cu - K_{\alpha}1,540598 \text{ \AA}$ , a potential difference of 40 kV, current of 40 mA, and X’Celerator detector. The software used to compare the samples was X’Pert HighScore Plus. The thin film thickness was studied using a Dektak 150 from Veeco. This is a surface profilometer that takes surface measurements using contact profilometry techniques in a line. This is equipped with a Low-Inertia Sensor (LIS 3) using a 3 mg force on the 10 nm stylus. It has a resolution of 10 Å in the 10 μm range where was set up. For the morphological characterization of the samples were used an electron microscope (SEM) Vega3 SB with tungsten source, an XFlash Detector 410 M, and an acceleration voltage of 10 kV under high vacuum ( $\sim 10^{-5}$  Pa) and Atomic Force Microscopy (AFM) Asylum Research MFP 3D Bio in tapping mode, the magnetic-domain investigation was carried out by using this same AFM in MFM mode on the surface of the sample using a *Co* tip. This measurement allows both the topographic and the magnetic-force image to be collected separately. Additionally, the SEM microscope has an X flash 410 M detector and SDD for EDXS microanalysis. Auger measurements were performed in an AES Omicron spectroscope. With a tungsten gun to bombard energetic electrons in the 2 – 50 KeV range under ultra-high vacuum conditions ( $\sim 10^{-8}$  Pa). The Argon gun to clean the surface and go into the bulk was set-up in  $xx$  mA for  $yy$  s. In this chapter, all the mentioned characterization techniques were performed at room temperature. All the fitting were performed using the least-squares method with a Levenberg Marquardt algorithm. Also, SEM micrographs were treated using Python 2.7. Here a Contrast enhancement was executed with a 0,5% of tolerance.

## 4.4. Results and discussions

Before all else, due to the sputtering chamber configuration, the Cobalt distribution in the substrates (Fig. 2-1.b) depends on the substrate position. Through EDXS measurements the relative Cobalt concentration in each sample position was identified. Following that, the sputtered particles follow a free mean path until reaching the substrate, which interrupts the trajectories into a conic section. Also, it is known by the experimental measurements that the *Co* concentration is greater near to the *Co*-target and lower close to the *ZnO*-target. So, based on a few EDXS measurements in different substrates, interpolating can be determined the *Co* distribution in the samples. Through a basic 4th order algorithm, and strained to the physical constraints, the relative percentage of Cobalt atoms with respect to Zinc atoms was founded. Fig. 4-1 shows this results in a contour plot-oriented according with the Fig. 2-1.b.

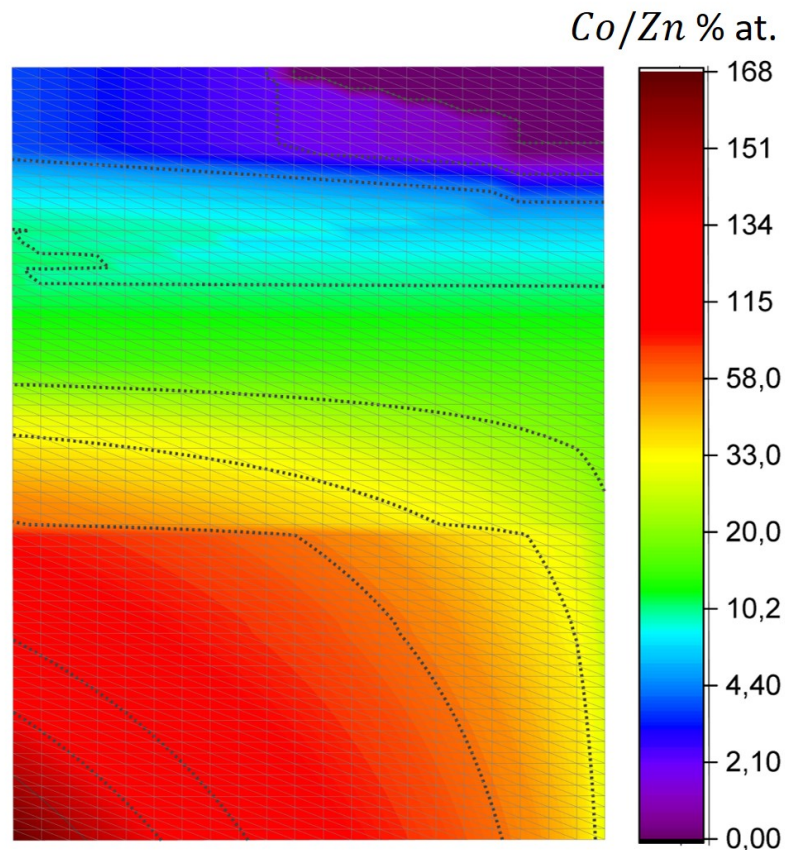


Figure 4-1.: Contour plot of the relative Cobalt atomic concentration as a function of the localization in the substrate holder.

Once the Cobalt concentration was determined, the next thing studied was the thickness of the thin films. Physically it is expected that the number of sputtered particles increases with the time of deposit. Due to the substrate distribution in the chamber, it depends on

the position of the substrate. With a profilometer, some samples with different deposit times were measured. The needle-height was recorded, and when it passes over the interface, thin-film/substrate, a significant change was observed (Fig. 4-2a).

The results were fitted using a linear fit before and after the interface. The height difference in the midpoint corresponds to the thickness of the thin film. This process was iterated in the rest of the samples. The thickness showed a tendency with the time deposit as expected (Fig. 4-2b). Also, the fact that it is not linear has a lot of sense, due to the nature of the synthesis. So, a logarithm function could explain the growth as a function of the deposit time. The thickness of the samples over  $ITO$  have similar behavior, but in

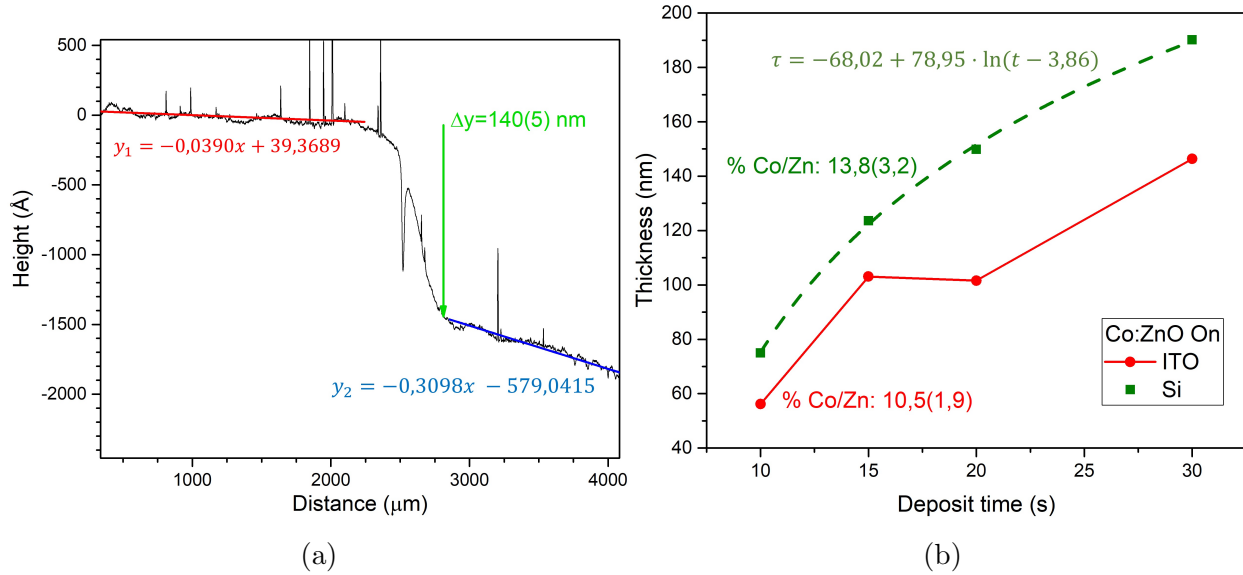


Figure 4-2.: (a) Profilometer results of a  $ZnO$  thin film sample in its interface. (b)  $ZnO$  Thickness as a function of the deposit time for two different  $Co$  concentration, with a  $Ln$ -like fit.

this case, for the same deposit time, there is a lower value for the thickness. That could be explained due to the chemical nature of the substrate, which allows the sticking of a higher number of sputtered atoms during the synthesis. Here the Cobalt concentration is possible evidence of this, the samples over  $Si$  have a higher concentration of Cobalt, with the same target power, so perhaps due to the chemical nature and the structural similarity, there are more  $ZnO$  and  $Co$  atoms in the sample over  $Si$  than in the sample on  $ITO$ . Also, some authors report a decrease in the in-plane constant of  $ZnO$  when Cobalt is added, while the lattice out-plane constant increases [214]. So, a higher concentration of Cobalt can result in a macroscopic increase in thickness. The thickness of the samples is an important value for the next characterization techniques, which involve knowing its value for the models, or the experimental setup.

The biggest problem for the Cobalt distribution determined by EDXS measurements is that we have a superposition with the contributions from the substrate, and it is pretty complicated to separate it from the sample. As it was studied in the previous chapter, the Oxygen vacancies play a relevant role in the physical properties of the  $ZnO$ . Even with the beam-energy is lower, there is saturation in the measurement from the substrate contribution, due to the nanometric thickness of the thin films. There are several superficial techniques, but we are interested in the atomic composition of the bulk, without reach the substrate. To solve this, a variation of the Auger spectroscopy was used (See Fig. 4-3).

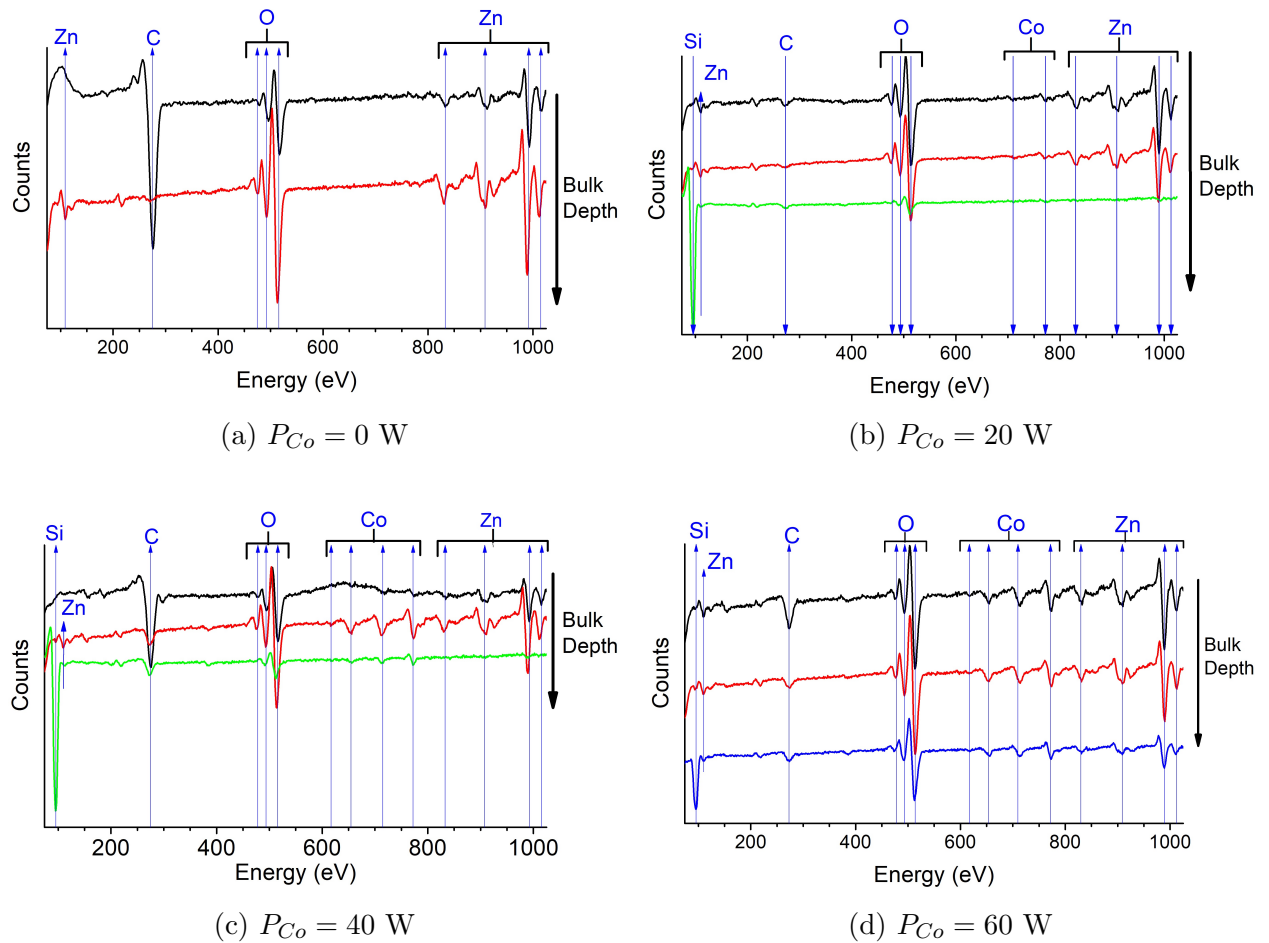


Figure 4-3.: Auger spectroscopy results for  $ZnO$  thin films synthesized at different  $P_{Co}$ .

Here, there is an Argon gun that cleans the surface to avoid dirtiness. But, also it can sputter the surface to measure deep in the bulk. So, the  $Ar$ -gun clean the surface and take another measurement. That was repeated until the substrate was reached. After 12 measurements the Auger spectrometer detects the substrate. The spectra were analyzed to identify and quantify the contribution of the atoms. Fig. 4-3 shows the results of the spectroscopy. A total of 14 different peaks were identified, included one for  $C$  (superficial dirt) and  $Si$



(substrate). For the peak identification, in  $C++$  was developed an algorithm, where also was performed the quantification method. This software also identified the associated triple-transition.

In Fig. 4-3 are shown only a few spectra, only for visualization reason. The down-arrows indicate the profundity in bulk, *i.e.*, the lower spectra are closer to the substrate. Fig. 4-3a does not present any Cobalt peaks due to the absence of Cobalt in the synthesis. The  $Co$  peaks in Fig. 4-3b, 4-3c, and 4-3d are not equal in relative intensities in each measurement, this is a clue for a random located ions. Also, there are some slight variations in the  $Co$ ,  $Zn$ , and  $O$  positions, as a trace of different kinds of bounds (share electrons). The average results of the quantification process are shown in Fig. 4-4.

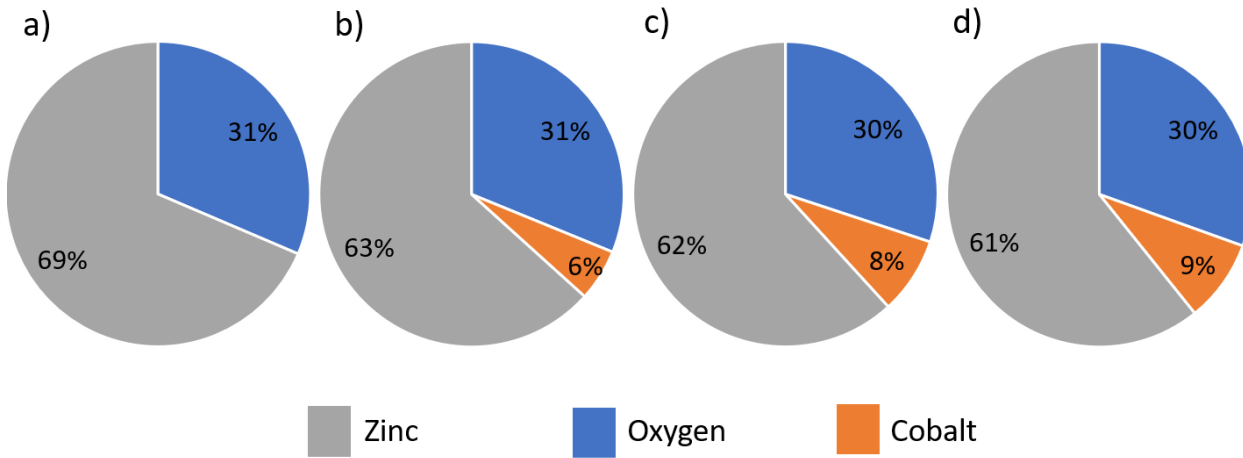


Figure 4-4.: Average atomic composition of the  $Co : ZnO$  thin films through Auger spectroscopy for samples synthesized with (a)  $P_{Co} = 0$  W, (b)  $P_{Co} = 20$  W, (c)  $P_{Co} = 40$  W, and (d)  $P_{Co} = 60$  W.

The relative values of the Cobalt concentration are 8, 7 ( $P_{Co} = 20$  W), 13, 18 ( $P_{Co} = 40$  W) and, 14, 38 ( $P_{Co} = 60$  W). So, as expected the relative concentration (and the absolute) increase with the power of the  $Co$ -target. Also, it is remarkable that the ratio of atoms  $O : Zn$  is on average 0,49. It implies that there are a lot of Oxygen vacancies in the structure, and possible  $Zn$  clusters. Even in this prospect, from the previous chapter, it is known that there is more likely a double  $V_O$  than a  $Co_O$  substitution.

Now that the concentration of Cobalt was established and it was identified a relation of like two  $Zn$  atoms per each  $O$ , *i.e.* an absence of  $O$  in the deposit process, XRD measurements were performed. In this step, the influence of  $P_{Co}$  is clear. Remembering that DMS materials need no magnetic clusters, it is necessary to find a balance between the magnetic response and the non-presence of Magnetic crystal phases. Also, possible  $Zn$  clusters could reduce the semiconductor properties.

Considering the synthesis parameters, there are three relevant variables in the crystal structure of the thin films: the chemical nature of the substrate, thermal stimulation, and Cobalt concentration. In the first aspect, we choose some substrates for its minimal coincident interface area (MCIA) and elastic energy with the Wurtzite  $ZnO$  [215]. These substrate were  $Au$  (0,060 meV and MCIA=121, 8),  $SiO_2$ (0,074 meV and MCIA=192, 0), and  $Al_2O_3$ (0,096 meV and MCIA=180.0). Fig. 4-5 shows the diffraction patterns for  $ZnO$  thin films over those substrates and soda-lime glass. These samples were fabricated at 423(2) K with  $P_{Co} = 40$  W. Some peaks in Fig. 4-5 are matched to the substrate, and just slight variations in intensity, FWHM, and central position are observed. These variations are attached to the growth of the  $ZnO$  on the substrate preferential planes.

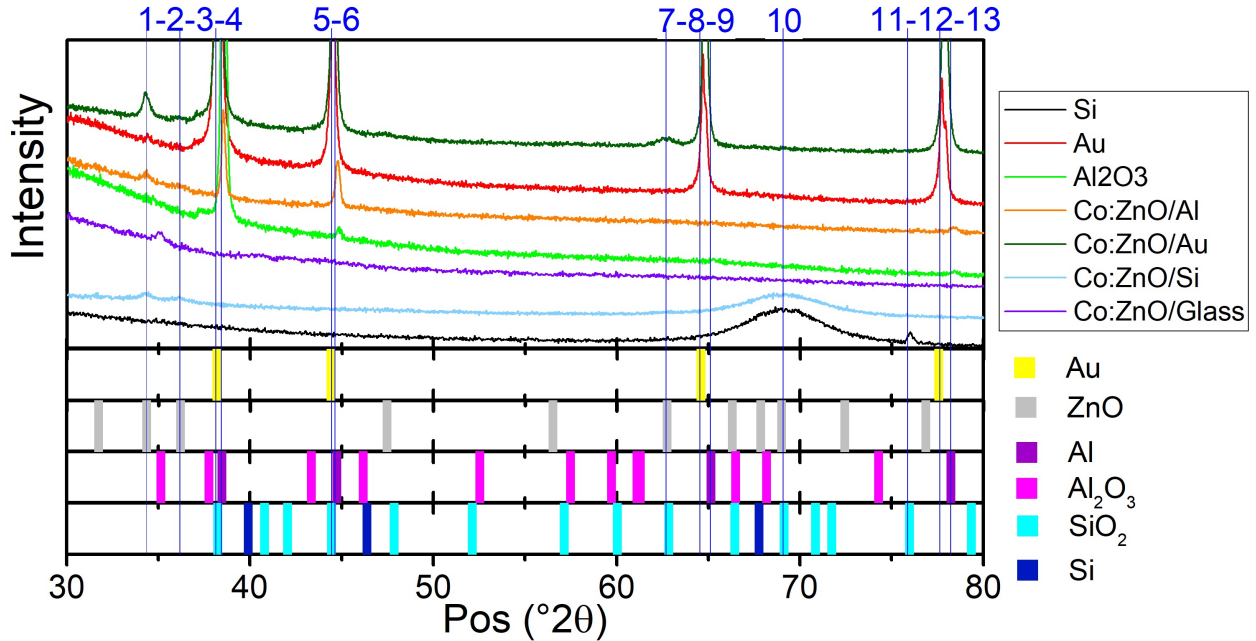


Figure 4-5.: Powder X-ray diffraction pattern for  $ZnO$  thin films deposited over different substrates, along with the XRD measurement for  $Au$ ,  $Al_2O_3$ , and  $Si$  substrates.

Peaks 1-13 in 4-5 are identified in Table 4-1. There also are presented the corresponding PDF file, the diffraction plane, the crystal system, and the space group. At the end of the table 4-1, two extra peaks are presented. These corresponding to the  $Al_2O_3$  principal peak and the  $Si$  peak of orientation. The first one is difficult to see because the atomic form factor of the closest  $Al$  peak is too much bigger. Concerning the second extra peak, probably the oxidation process and the amorphous  $SiO_2$  film over the  $Si$  produce a destructive interference and make it impossible to see. But it corresponds to the growth plane provided by the  $Si$  manufacturer (See Appendix B).

Table 4-1.: Identified peaks in Fig. 4-5 for substrates and *Co* doped *ZnO* thin films.

#	Pos. [ $2\theta^\circ$ ]	Match	PDF file <sup>a</sup>	Plane	Crystal system	Space Group
1	34, 364	<i>ZnO</i>	01-080-00074	002	Hexagonal	186
2	36, 207	<i>ZnO</i>	01-080-00074	101	Hexagonal	186
3	38, 185	<i>Au</i>	00-004-0784	111	Cubic	225
4	38, 473	<i>Al</i>	00-004-0787	111	Cubic	225
5	44, 393	<i>Au</i>	00-004-0784	200	Cubic	225
6	44, 140	<i>Al</i>	00-004-0787	200	Cubic	225
7	62, 754	<i>ZnO</i>	01-080-00074	103	Hexagonal	186
8	64, 578	<i>Au</i>	00-004-0784	220	Cubic	225
9	65, 135	<i>Al</i>	00-004-0787	220	Cubic	225
10	69, 119	<i>SiO<sub>2</sub></i>	01-085-0461	300	Hexagonal	154
11	75, 967	<i>SiO<sub>2</sub></i>	01-085-0461	104	Hexagonal	154
12	77, 549	<i>Au</i>	00-004-0784	311	Cubic	225
13	78, 230	<i>Al</i>	00-004-0787	311	Cubic	225
-	37, 763	<i>Al<sub>2</sub>O<sub>3</sub></i>	01-077-2135	110	Rhombo.	167
-	46, 384	<i>Si</i>	00-035-1158	200	Cubic	225

<sup>a</sup> See Appendix C.

The principal peak of *ZnO* ( $2\theta = 34, 364^\circ$ ) corresponds to the Wurtzite phase (plane [100]). This phase has an elastic energy/MCIA with each substrate of 0, 016 meV/28, 1 Å<sup>2</sup> ([111] *Al*), 0, 096 meV/180, 0 Å<sup>2</sup> ([100] *Al<sub>2</sub>O<sub>3</sub>*), 0, 060 meV/121, 8 Å<sup>2</sup> ([111] *Au*), and 0, 074 meV/192, 0 Å<sup>2</sup> ([110] *SiO<sub>2</sub>*). Also the [110] *Si* plane has 0, 055 meV/239, 3 Å<sup>2</sup> with the [100] *Si*.

The next relevant variable in the structure of the *Co* : *ZnO* is the Cobalt concentration. If it is too high, clusters of Cobalt will start to form, as well as secondary phases of *Co<sub>x</sub>O<sub>y</sub>*. If the Cobalt atoms are well distributed in the semiconductor matrix, no-extra diffraction peaks will appear. But, the presence of the impurities atom distorts the structure, and consequently the peaks in the diffraction pattern. This distortion could appear as a shift of the *ZnO* peaks, a change of the FWHM, a change in the relative intensities, and destruction of peaks. Fig. 4-6 and Fig. 4-7 show XRD measurements for the samples prepared with different  $P_{Co}$  (0 W, 20 W, 40 W, and 60 W).

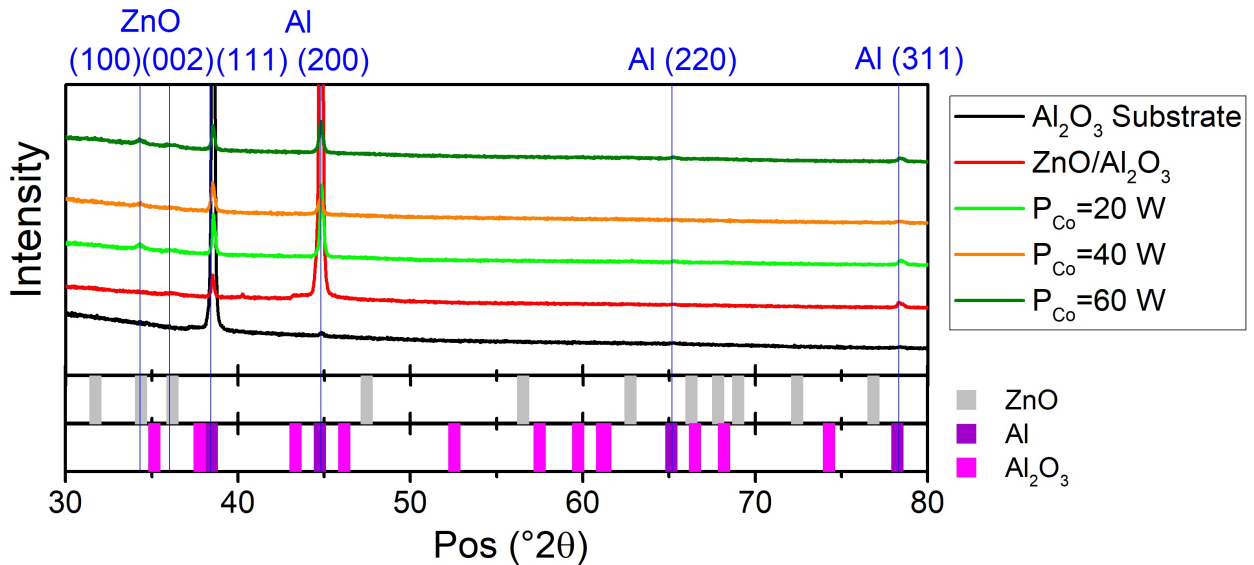


Figure 4-6.: X-ray diffraction pattern of the  $Co : ZnO/Al_2O_3$  samples synthesized at different Cobalt target power.

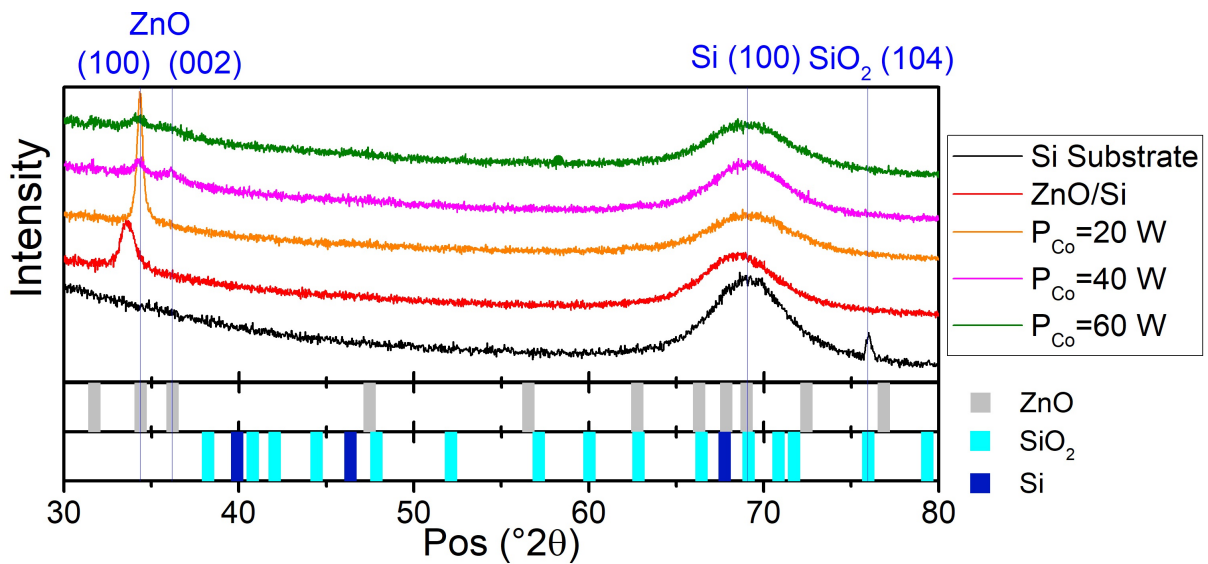


Figure 4-7.: X-ray diffraction pattern of the  $Co : ZnO/Si$  samples synthesized at different Cobalt target power.

There are not new peaks in the patterns when the Cobalt is added, even in the highest  $P_{Co}$ , and the variations in the pattern are imperceptible. Table 4-2 shows the original values for  $P_{Co} = 0$  W, the changes in the peak position, and the FWHM. Also, Table 4-2 shows the relative intensities with the principal peak of each pattern for the  $Zn[100]$  peak and the relative change in the intensity of the principal peak.

There is no apparent relation between the increase of Cobalt and the FWHM, or the rela-

Table 4-2.: Principal peaks position, FWHM, and relative intensities values/changes extracted from the XRD patterns of the *Co* : *ZnO* samples synthesized at different powers for the Cobalt target.

$P_{Co}$	Substrate	Position	FWHM	R. Intensity	Position	FWHM	R. Intensity
(W)		( $2\theta^\circ$ )	( $2\theta^\circ$ )	(%)	( $2\theta^\circ$ )	( $2\theta^\circ$ )	(%)
		Principal peak			<i>ZnO</i> [100]		
0	<i>Al<sub>2</sub>O<sub>3</sub></i>	38,50	0,12	100,00 <sup>b</sup>	34,36	-	-
20	<i>Al<sub>2</sub>O<sub>3</sub></i>	-0,05 <sup>a</sup>	-0,03 <sup>a</sup>	151,70 <sup>b</sup>	0,07 <sup>a</sup>	0,52 <sup>a</sup>	4,62 <sup>c</sup>
40	<i>Al<sub>2</sub>O<sub>3</sub></i>	-0,01 <sup>a</sup>	-0,09 <sup>a</sup>	97,38 <sup>b</sup>	0,05 <sup>a</sup>	0,45 <sup>a</sup>	10,98 <sup>c</sup>
60	<i>Al<sub>2</sub>O<sub>3</sub></i>	-0,02 <sup>a</sup>	-0,03 <sup>a</sup>	91,98 <sup>b</sup>	0,04 <sup>a</sup>	0,55 <sup>a</sup>	10,26 <sup>c</sup>
0	<i>Si</i>	68,51	5,20	100,00 <sup>b</sup>	33,62	0,98	91,13 <sup>c</sup>
20	<i>Si</i>	-0,59 <sup>a</sup>	0,19 <sup>a</sup>	56,65 <sup>b</sup>	-0,69 <sup>a</sup>	0,62 <sup>a</sup>	425,22 <sup>c</sup>
40	<i>Si</i>	-0,55 <sup>a</sup>	0,10 <sup>a</sup>	89,16 <sup>b</sup>	-0,63 <sup>a</sup>	0,16 <sup>a</sup>	28,18 <sup>c</sup>
60	<i>Si</i>	-0,52 <sup>a</sup>	-0,44 <sup>a</sup>	74,38 <sup>b</sup>	-0,52 <sup>a</sup>	-0,12 <sup>a</sup>	29,47 <sup>c</sup>

<sup>a</sup>  $P_{Co=0} - P_{Co}$                       <sup>b</sup>  $P_{Co}/P_{Co=0}$                       <sup>c</sup>  $P_{Co}^{[100]}/P_{Co}^{1st}$

tive intensities. Nevertheless, the change in the position decreased when  $P_{Co}$  increased. So, there is a first strong change in the position, and then it is smaller as the impurities increase. Probably that is a result of the formation of segregated phases of Cobalt. These phases are no-showed in XRD measurements due to their low concentration in the sample and their segregated nature. Some authors report several peaks associated to the different *Co* form into the material ( $Zn_{1-x}$ , *CoO*,  $Co_3O_4$ ,  $ZnCo_2O_4$ ) [214, 216]. All these peaks are near to  $36^\circ$  and the assignment is nontrivial, tiny shifts to the lower angles of the principal *ZnO* peak ( $\sim 36^\circ$ ) may be assigned to  $Zn_{1-x}Co_xO$ , where the Cobalt is replacing a Zinc atom in the structure. That is the case of the samples with different *Co* concentrations, and since no return to the original position is observed, it can be concluded that no *Co* phases are present in a notable quantity. On the other hand, the most common *Co* phase, which is possible in the synthesis condition, is characterized by a remarkable peak near to  $\sim 44^\circ$  and a decrease in the intensity of the *ZnO* peaks while that peak increase [214]. That is another reason to think that no secondary phases are present in thin films.

The final aspect that might affect the structure of the *Co* : *ZnO* is the deposit temperature. Despite having an *in situ* annealing process at 473(2) K for two hours, and lower temperatures in the synthesis, we expect that there has some influence. This temperature influence in the structure could be due to the species mobility when the film is growing. We expect to observe some dependence of the *Co* diffusion with the temperature. Fig. 4-8 and Fig. 4-9 show the diffractogram of samples prepared at different temperatures ( $T_s = 293(4)$ ,  $T_s = 323(6)$ ,  $T_s = 373(3)$ , and  $T_s = 423(2)$ ,) on *Al<sub>2</sub>O<sub>3</sub>* and *Si* respectively.

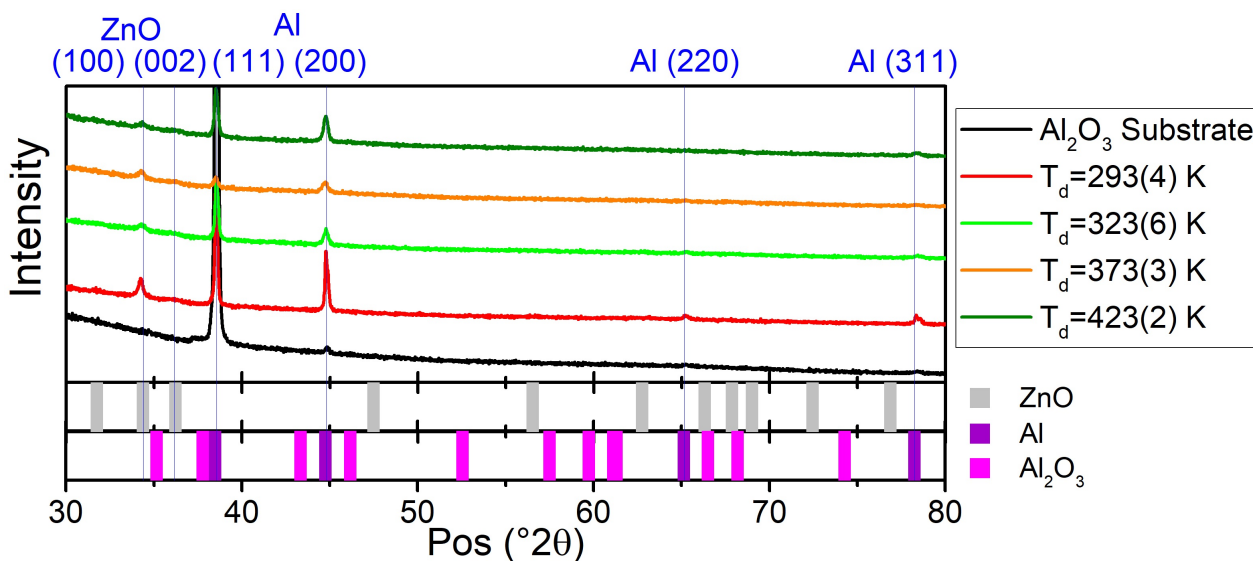


Figure 4-8.: Diffractogram for the *Co* doped *ZnO* samples over *Al*<sub>2</sub>*O*<sub>3</sub> prepared at different substrate temperature.

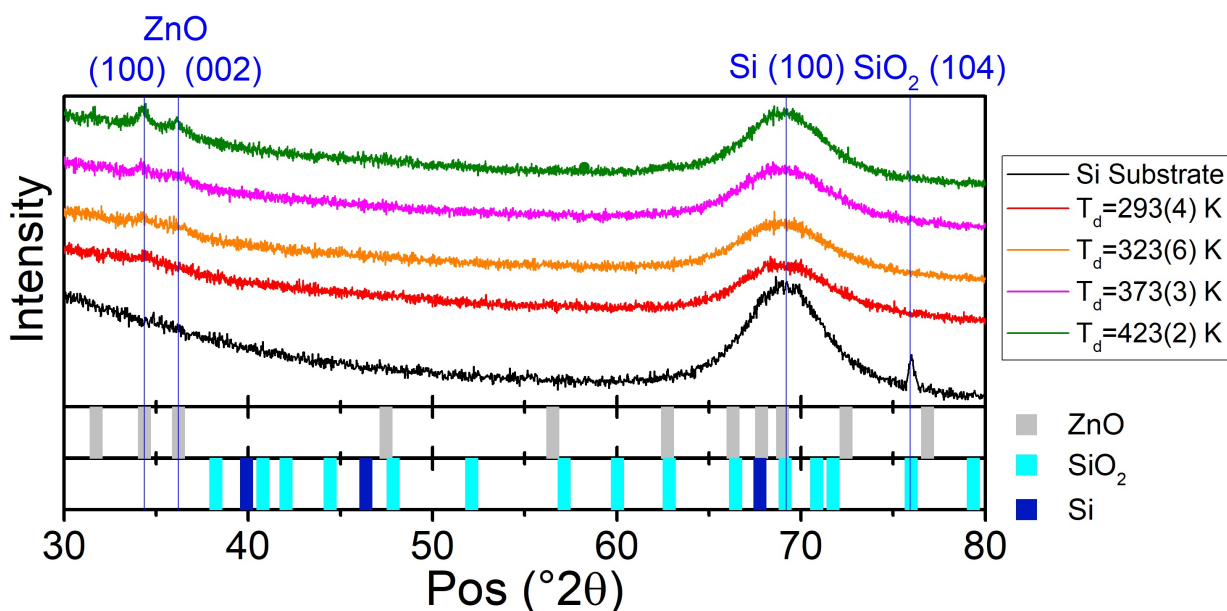


Figure 4-9.: Diffractogram for the *Co* doped *ZnO* samples over *Si* prepared at different substrate temperature.

There are the same peaks when the synthesis temperature change. Once again, the changes are more about the characteristics of each peak. Table 4-3 shows the original values for  $T_s = 293$  W, the changes in the peak position, and the FWHM. Also, Table 4-3 shows the

relative intensities whit the principal peak of each pattern for the  $Zn[100]$  peak and the relative change in the intensity of the principal peak.

Anew, seems like there are no evident correlation in the relative intensities. In the sam-

Table 4-3.: Principal peaks position, FWHM, and relative intensities values/changes extracted from the XRD patterns of the  $Co : ZnO$  samples synthesized at different substrate temperature.

$T_s$	Substrate	Position	FWHM	R. Intensity	Position	FWHM	R. Intensity
(K)		( $2\theta^\circ$ )	( $2\theta^\circ$ )	(%)	( $2\theta^\circ$ )	( $2\theta^\circ$ )	(%)
293	$Al_2O_3$	38,50	0,11	100,00 <sup>b</sup>	34,22	0,26	11,76 <sup>c</sup>
323	$Al_2O_3$	-0,03 <sup>a</sup>	0,02 <sup>a</sup>	52,69 <sup>b</sup>	0,01 <sup>a</sup>	-0,15 <sup>a</sup>	8,03 <sup>c</sup>
373	$Al_2O_3$	0,02 <sup>a</sup>	-0,14 <sup>a</sup>	6,07 <sup>b</sup>	-0,03 <sup>a</sup>	-0,10 <sup>a</sup>	70,32 <sup>c</sup>
423	$Al_2O_3$	0,00 <sup>a</sup>	-0,09 <sup>a</sup>	32,88 <sup>b</sup>	-0,09 <sup>a</sup>	-0,19 <sup>a</sup>	6,08 <sup>c</sup>
293	$Si$	69,03	5,60	100,00 <sup>b</sup>	34,00	6,00	29,57
323	$Si$	0,06 <sup>a</sup>	-0,27 <sup>a</sup>	107,78 <sup>b</sup>	-0,47 <sup>a</sup>	1,40 <sup>a</sup>	17,69 <sup>c</sup>
373	$Si$	0,05 <sup>a</sup>	-0,10 <sup>a</sup>	92,61 <sup>b</sup>	-0,18 <sup>a</sup>	4,00 <sup>a</sup>	23,53 <sup>c</sup>
423	$Si$	-0,03 <sup>a</sup>	0,50 <sup>a</sup>	140,86 <sup>b</sup>	-0,25 <sup>a</sup>	5,18 <sup>a</sup>	28,18 <sup>c</sup>

<sup>a</sup>  $T_{s=ROOM} - T_s$       <sup>b</sup>  $T_s/T_{s=ROOM}$       <sup>c</sup>  $T_s^{[100]}/T_s^{1st}$

ples over  $Si$ , the FWHM increases when the  $T_s$  does it. Also, the  $Zn[100]$  peak position has a left-shift that increase whit  $T_s$ . There are no major changes in the diffraction patterns in the studied range when the synthesis temperature increase. It is probably because the posterior *in situ* annealing has a higher temperature, so, the maximum mobility of ions is set by that temperature.

Another feature that might change with the deposit temperature is the topography of the samples. Due to the higher atoms' mobility when the temperature increase, there are more and bigger grains. The thin-films formation can be resumed as a four-step operation. A stochastic process of nucleation first. Then a controlled growth by the surface diffusion of the three-dimensional nuclei. Next, the formation of a network structure. And, finally, a subsequent filling to achieve a continuous film. Depending on the thermodynamic parameters of the deposit and the substrate surface, the initial stages of nucleation and growth can be described in three ways. (a) island type, called Volmer-Weber type, (b) layer type, called Frank-van der type Merwe, and (c) mixed type, called Stranski-Krastanov type. In almost all practical cases, growth is produced by the formation of islands [217].

Fig. 4-10 shows comparative results between a sample synthesized at room temperature (293 K) and another at 373 K.



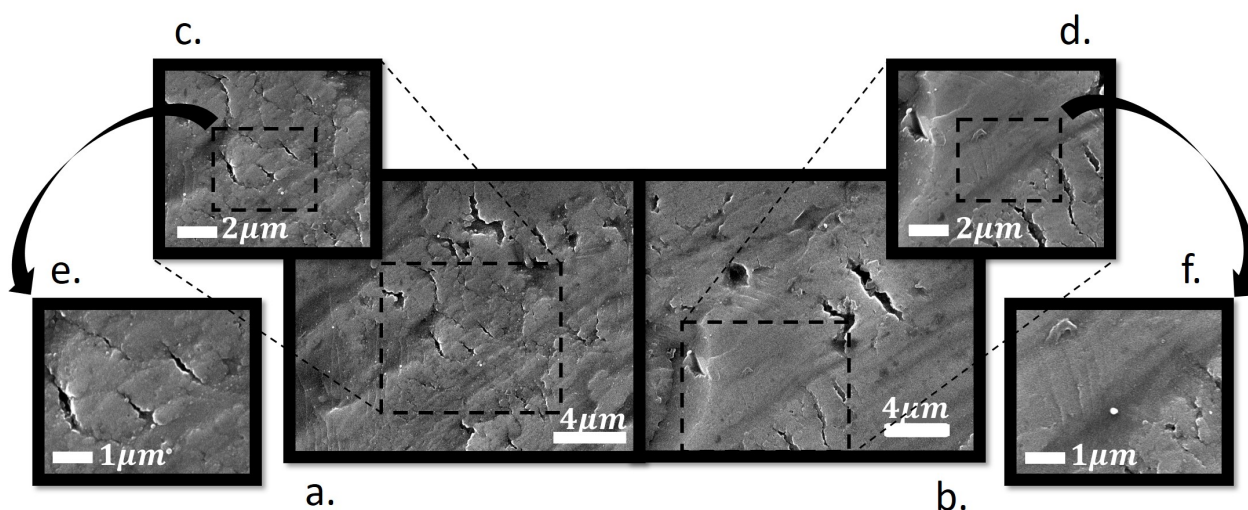


Figure 4-10.: SEM micrographs of  $Co : ZnO/Ti$  thin films fabricated at 293(4) K (left) and 373(2) K (right). All micrograph are from SE at  $HV = 30$  kV, average  $WD = 10,05(1)$  mm and magnifications of  $10kx$  (a, b),  $20kx$  (c, d), and  $40kx$  (e, f).

The micrographs have some slight differences at  $10kx$ . The room-fabricated have more fissure than the other. Probably cause there is more species mobility at higher temperatures. Also, due to the thermal stimulus more sputter atoms stick to the substrate. In conclusion, there are more atoms with higher mobility when the substrate temperature increase. So, that results in a more homogeneous thin film.

The chemical nature of the substrates is an important factor in the morphology of the thin films. That is due to their low thickness, so the first nanometers try to reproduce the substrate morphology. Also, the species mobility is bounded to the free bonds and electronegativity of the substrate surface. Fig. 4-11 shows comparatives micrographs synthesized on the different substrates.

The dependence of the substrate in the morphology is evident. There are some islands in the sample over  $Ti$  (Fig. 4-11.a) as we see in above (Fig. 4-10). Some black points are present on  $Co : ZnO/Au$  (Fig. 4-11.b), but seems homogeneous under that. The film deposited over glass is the most uniform (Fig. 4-11.c), also is the micrograph at lowest  $HV$  due to the insulator characteristic of the soda-lime glass. Some grains are observed in the  $Co$ -doped films over  $ITO$  (Fig. 4-11.d) and  $Al_2O_3$  (Fig. 4-11.e), being smaller in the second one. Finally, there are some grooves on the sample over  $Si$  that seem like the trace of bigger island formation.



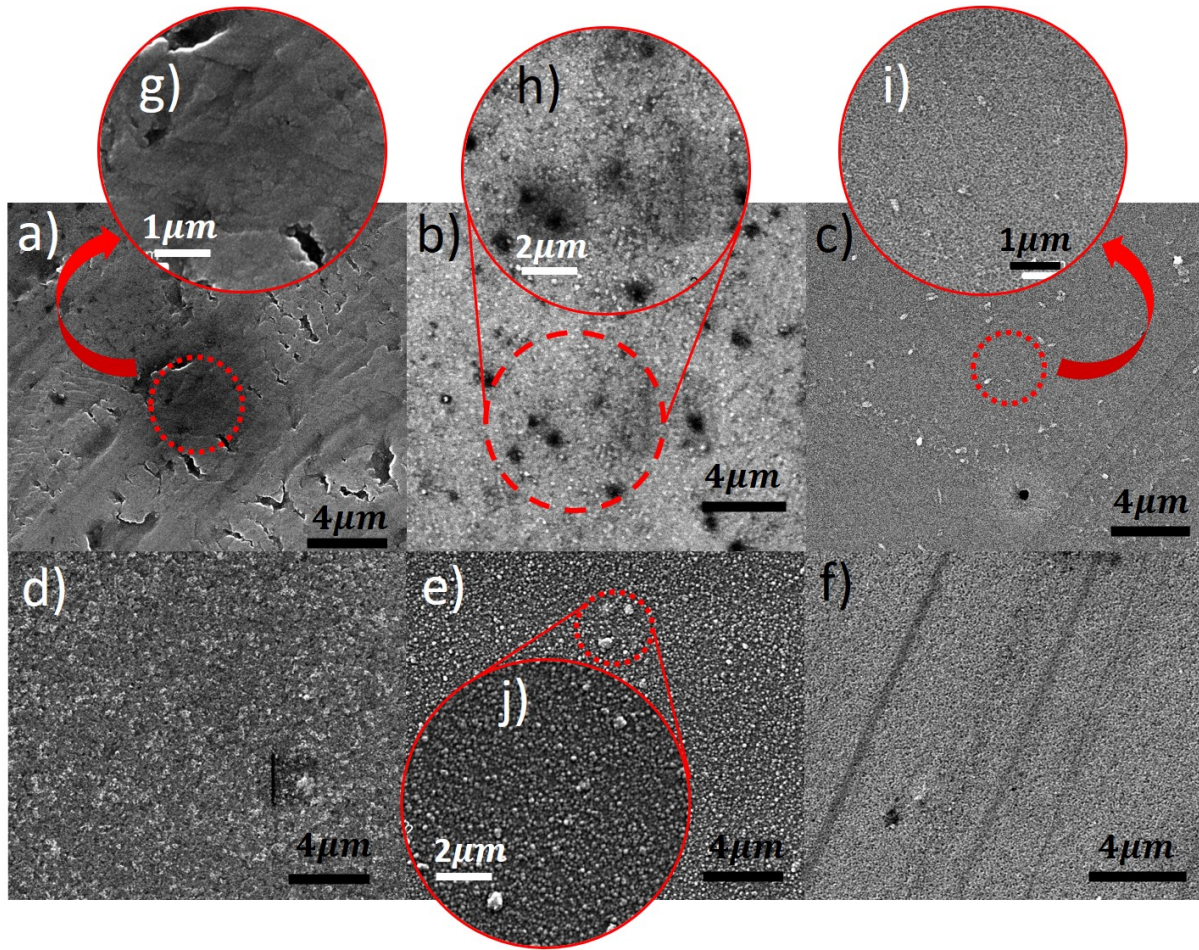


Figure 4-11.: SEM micrographs of  $Co : ZnO$  thin films fabricated at 423(2) K over  $Ti$  (a, g),  $Au$  (b, h), soda-lime glass (c, i), ITO (d),  $Al_2O_3$  (e, j), and  $Si$  (f). All micrographs are from SE at  $HV = 30$  kV (except c and i at 10 kV), average  $WD = 9,8(1)$  mm and magnifications of  $10k\times$  (a, b, c, d, e, f),  $20k\times$  (h, j),  $36k\times$  (i), and  $40k\times$  (g).

Now we are interested in the effect of Cobalt in the morphology, but in the resolution of the SEM apparently, there are not variations. So, AFM micrographs were taken in samples with different  $Co$  concentrations. Also, AFM can be performed in different modes. Using a  $Co$  tip, the magnetic interaction between an induced magnetic moment in the tip and the sample can be recorded. This extra-measurement gives information about the magnetic distribution in the surface, like magnetic domains. Fig. 4-12 show some AFM/MFM micrographs as a function of the  $P_{Co}$ .

The grain height increase significantly when the Cobalt increase in the semiconductor matrix. It is easy to observe in the change of the scales, where the range change from 8,5 nm ( $P_{Co} = 0$  W) to 180 nm ( $P_{Co} = 60$  W). Also, the intensity of the magnetic response is bigger.

Zoom in Fig. 4-12.b and its 3D representation (Fig. 4-12.c) show an isotropic distribution of the grains. That is very important to industrial applications. If the grain distribution would have a spatial dependence, there would have no standard electric properties, but as expected the sputtering technique results in uniform films.

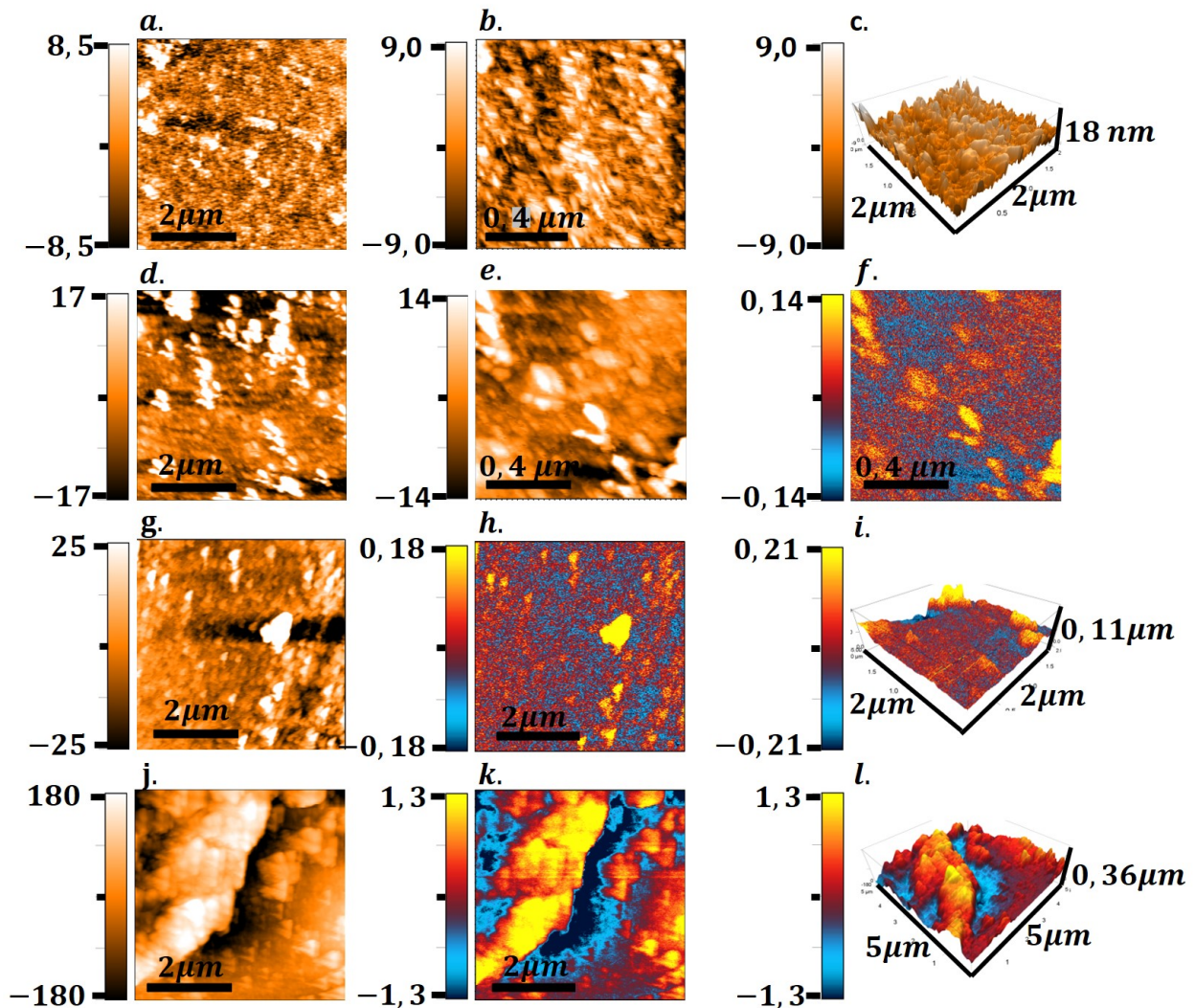


Figure 4-12.: AFM/MFM micrographs of  $ZnO$  (a-c) and  $Co$ -doped  $ZnO$ . Thin films prepared over soda-lime glass at 423(2) K and  $P_{Co} = 20$  W (d-f),  $P_{Co} = 40$  W (g-i), and  $P_{Co} = 60$  W (j-l). All the color-bars scale are in nm. Gold figures AFM Height, and cold-warm scale represent the amplitude of the signal from the magnetic interaction. Z-axis in 3D plots represent the AFM height.

Comparing Fig. 4-12.e and Fig. 4-12.f (Zoom of the Fig. 4-12.d) there is some correlation in the highs of the topographic and magnetic response. From here it can be inferred that the grains have a high concentration of  $Co$ . The spintronic application requires maintaining the semiconductor properties of the samples, if the grain boundary is too well defined it



may represent a problem. Possible  $Co$  phases are present in these grains, and there is not a uniform distribution of Cobalt on the surface. In a similar way, Fig. 4-12.g and Fig. 4-12.h have a correlation, and the 3D-zoom (Fig. 4-12.i) helps to understand it. Here, the grain is more defined but it is only one of it in  $25\mu\text{m}^2$ . o, there is no reason to worry about it if we keep a higher scale in the applications. The worst scenery is to have extensive and high grains with a stronger magnetic response. Unfortunately, is the  $P_{Co} = 60\text{ W}$  case. There, no secondary phases were identified by XRD measurements, but huge magnetic grains are on the surface (See Fig. 4-12.j-l).

Now, the primordial interest is to have a balance between the magnetic response and the no- $Co$ -phases condition. Although the grains are not necessarily evidence of secondary phases, if it does not exist there are not concerns. The AFM measurements allow the quantification of how high are in average the grains in the sample. This is known as roughness. Besides the roughness, the root-mean-square (RMS) roughness ( $R_q$ ) is the square root of the distribution of surface height (See Fig. 4-13).

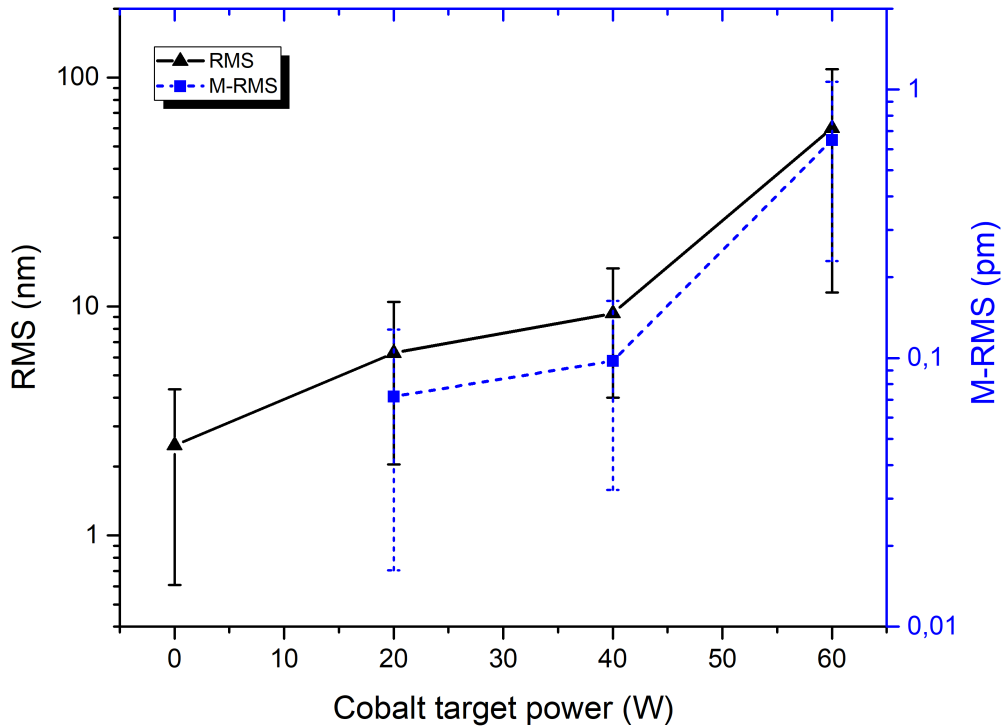


Figure 4-13.: Root mean square roughness as a function of the Cobalt power target for  $Co : ZnO$  thin films synthesized at 473(2) K over soda-lime glass. Error bars represent the standard deviation.

---

It is considered to be more sensitive than the average roughness for large deviations. In the Fig. **4-12** cases, there are some isolated big grains. So, RMS is the best option. The Fig. **4-13** shows that value as a function of the  $P_{Co}$ . Here, a logarithmic scale is necessary cause the variation in the RMS from 40 W to 60 W is more than 600%. Here there is a huge change in the topography and the magnetic response. In the figure can be observed a change even in the concavity of the tendency. In the magnetic RMS, the change is also large, but in  $P_{Co} = 0$  there is no data. That value can be assumed very close to 0 pm, but once again would be another outsize change. Focus on that, when we have no Cobalt in the semiconductor matrix, we do not have a DMS. Also, when we have too much Cobalt in the structure, it becomes an alloy and stops being a DMS. In that logic, the  $Co$  concentration appears to be an order parameter.

# 5. Electrical, optical and magnetic characterization of Cobalt doped ZnO thin films

Until now, Cobalt concentrations were identified for different  $P_{Co}$  values and their distribution on the substrates. Also, there are no secondary phases of  $Co$  presented in the XRD analysis. Finally, it was identified a strong correlation between the M-RMS and the  $Co$  concentration. Now, the principal interest is to correlate the optical, electrical, and magnetic properties of the thin films with those results. To do that, this chapter starts similarly to the previous. First, a background is seated and after establishing the experimental and technical details the results of the optical, electric, and magnetic characterization are presented.

## 5.1. State of the art: Electrical, optical and magnetic properties

To develop information storage devices, both magnetic and electrical properties of solid-state materials have been considered, including magnetic recording, magnetoresistive random access memory (MRAM), and flash memory, resistive random access memory (RRAM) [218]. In these techniques, the spin, and charge of electrons are employed separately. Transition metal-doped  $ZnO$  is a promising candidate material for the field of spin-electronics.

Carrier spins are used to transport, store and process information in novel ways, providing both enhanced performance and new functionalities in traditional microelectronic devices. The magnetic properties of a DMS are intimately coupled to the carrier concentration and carrier type within the material through the s-d and p-d exchange integrals. This is beneficial because it allows external control over the magnetic properties by electronically or optically manipulating the carriers in the DMS [219, 220]. For example, in magnetic recording, a magnetic field is used to write or read the information stored on the magnetization. Simultaneously, RRAM, as a promising candidate for next-generation nonvolatile memory, is based on resistance change (high and low) modulated by an electrical stimulus, for the recording of two logic states (“0” and “1”) [221]. The quest for higher data density in information storage is motivating research on manipulating magnetization without the need

of H, [21, 25, 222–226] to achieve a new paradigm where spin and charge act on each other. Ultimately, allowing faster, low-energy operations with a combination of information writing, transfer, treatment, and reading. RRAM is currently of great interest to realize the switching between insulating/conductive states with an ultrahigh off/on ratio, [221, 226]. Cobalt-doped ZnO (*Co : ZnO*) has been selected as the storage medium in this work for three reasons. First, *Co : ZnO* stands out as a seminal spintronic material due to its high TC. [227–229]. Second, *Co : ZnO* shows robust ferromagnetism under both insulating and metallic states. [134, 230]. At last, the ZnO commutation systems show stable RS during repeated sweep cycles. [226].

Dietl’s theory [25] is based on an indirect exchange mechanism where the ferromagnetism between magnetic dopants is mediated by holes in the valence band. P-type material was predicted to result in high TC primarily because both the exchange integral parameter and the density of states are higher in the valence band than the conduction band. Dietl’s theory has proven useful in understanding the experimental results for *GaMnAs*. However, it does not appear to be consistent with the experimental results for transition metal-doped wide bandgap semiconductors, such as *ZnO* and *GaN*. This stems from several reasons, including the difficulty in experimentally preparing p-type ZnO material and the many observations of ferromagnetism in n-type ZnO DMS. Nevertheless, Dietl’s original theory has led to multiple experimental and computational studies of transition metal doping in ZnO and GaN [231–237].

Coey et al [227] have proposed another model for ferromagnetism in DMS materials based on a spin-split donor impurity band. This model provides a mechanism where ferromagnetism is influenced by defect states in the material. In the model, donor defects (which could arise from either Oxygen vacancies or Zinc interstitials in the case of ZnO) overlap at large concentrations to form an impurity band. The impurity band can interact with local magnetic moments through the formation of bound magnetic polarons (BMP). Within each BMP, the bound carrier interacts with the magnetic dopants inside its radius and can align the spins of the magnetic dopants parallel to one another. Ferromagnetism is achieved when the BMPs start to overlap to form a continuous chain throughout the material, thus percolating ferromagnetism in the DMS. However, Coey showed that, in this model, to achieve a high  $T_c$  a fraction of the polaronic charge must delocalize (or hybridize) onto each magnetic dopant. In a band scheme, this occurs when the impurity band overlaps with unoccupied d-levels of the magnetic dopant.

Within a similar framework to Coey’s model, Kittilstved et al [238] have performed detailed spectroscopic experiments on Cobalt-doped ZnO. Their results show that the singly ionized  $Co^+$  state lies close to the conduction band, similar in energy to a shallow donor state. Since the energies are similar, charge transfer (CT) can occur between the Cobalt

atoms and the donor impurities, thus leading to the hybridization necessary for ferromagnetism. Kittilstved et al have also shown that this leads to an inherent polarity difference for ferromagnetism in Cobalt- and Manganese-doped ZnO. Whereas ferromagnetism in Cobalt-doped ZnO is closely tied to the presence of shallow donors, Manganese-doped ZnO is closely tied to the presence of shallow acceptors. The difference lies in the location of the singly ionized Mn+3 state, which sits close to the valence band in ZnO. Consistent results have been reported for carrier-doped Mn:ZnO films [239, 240].

Other studies have also elucidated the importance of carriers and defects in mediating ferromagnetism in ZnO. Tuan et al [99] found that weak ferromagnetism in Co-doped ZnO films can be activated by post-growth vacuum annealing, changing the films from insulating to semiconducting behavior. The specific role of Zn interstitials has also been studied. Zn interstitials are believed to form a shallow donor state in ZnO. Reversible on/off ferromagnetic ordering at room temperature in chemically synthesized Co-doped ZnO films was achieved by the controlled incorporation and removal of Zn interstitials [241]. Zn interstitials were introduced by annealing in the presence of Zn vapor and subsequently removed by annealing in Oxygen. The interstitials were believed to activate ferromagnetism by introducing electrons, which were removed by oxidation. Khare et al [242] have also investigated the role of Zn interstitials.

They also found that the magnetization in Co-doped ZnO is enhanced by introducing Zn interstitials into the lattice during annealing, but that the magnetization did not depend on carrier concentration. Their results also indicated that Oxygen vacancies were not responsible for changes in magnetization. However, recent theoretical modeling does suggest that Co+2–Oxygen vacancy pairs are capable of promoting long-range FM coupling in the presence of n-type doping [243]. It seems, therefore, the recent literature suggests that ferromagnetism in Co-doped ZnO is highly dependant on intrinsic defects in the material. These defects may rely on the presence of the transition metal dopants by the formation of complexes that mediate FM ordering or defects alone may be enough to cause ferromagnetism.

The sharp absorption edge and high optical transmission within the visible region of the spectrum are reported as proof of the high quality of ZnO nanostructures. When the samples exhibited sharp absorption near the bandgap edge, indicating that no extra phases are formed [178]. Many groups have confirmed that Co atomically substitutes on Zn sites using a variety of methods, including EXAFS [125, 130], XPS [90, 99, 244, 245], MCD [99, 234, 246], XAS [125, 247] ESR [248], XANES [249] and optical absorption [99, 101, 246, 250, 251]. Three absorption peaks are reported in the doped films, characteristic of a d–d transition levels attributed to  $Co^{+2}$  occupying tetrahedral lattice positions, and indicate that Cobalt is substituting as  $Co^{+2}$  on Zn lattice sites in the films; these peaks are reported in multiple publications on  $Zn_{1-x}Co_xO$  films as mentioned above.

Some reports in the literature observe a red-shift in the bandgap energy as the Cobalt concentration is increased [252–255]. The red-shift is typically attributed to the sp–d exchange between the ZnO band electrons and localized d-electrons associated with the doped  $Co^{+2}$  cations. The interaction leads to corrections in the energy bands; the conduction band is lowered and the valence band is raised causing the bandgap to shrink [256]. On the other hand, other papers have reported a blue-shift in the bandgap of ZnO with Cobalt doping. Peng et al [257] reported a blue-shift in the bandgap of the material and a red-shift in the band tails. Ozerov et al [248] also reported a blue-shift in the bandgap in nanocrystalline films. Yoo et al [258] observed a blue-shift in Al- and Co-codoped ZnO films which were attributed to the Burstein–Moss effect from an increase in the carrier concentration.

## 5.2. Experimental aspects

In this section some fundamentals of the techniques involved will be approached, this will allow a better understanding of the results. First, an explanation of the Wenner method and its implementation for the thin films, then a simple review of the UV-VIS-NIR spectroscopy is presented, and finally, some generalities of the vibrating sample magnetometer (VSM) used for the magnetic characterization are explained.

The Wenner method [259], also known as the four-point method, consists of obtaining a potential difference and the imposition of a current from 4 electrodes on the surface of the material, in an aligned and equidistant way [259], bearing in mind that conduction can occur superficially, the closer the electrodes are, the less electronic noise the signal will have. Knowing the distance between the electrodes, the applied current, and the potential drop, it is possible to determine the resistivity of the material [259, 260].

That configuration allows the measurement of the superficial resistance, also known as sheet resistance. If each couple of electrodes are placed in the top and bottom of the thin film respectively, the bulk resistance can be measured using the same configuration. Also, some interesting effects can be observed when the entire material takes part, and not only the superficial part.

The chemical nature of the electrodes and how they interact with the material are crucial variables in electric measurements. Different kinds of electrodes (Gold, Silver, and graphite) were used in the samples. The gold electrode is the commonest for industrial application, due to its long durability and excellent performance. Silver contacts are uncommon in de-



vices due to the easy oxidation with the environment, but its better conductivity could give more information for research proposes. Also, graphite is the cheapest option but has a considerable conductivity that can allow the operation of the device at a lower price.

Ultraviolet-visible-near infrared (UV-VIS-NIR) spectrophotometry is a photon emission spectroscopic technique that uses electromagnetic radiation of a very precise wavelength, said radiation is absorbed, reflected, or transmitted by the sample, causing transitions that are quantified by the detector. To quantify the physical phenomena mentioned above, three optical parameters are used: spectral transmission (T), spectral reflectance (R), and absorbance (A). The UV-Vis-NIR spectroscopy employs a wide range of optical radiation, to carry it out is necessary three different lamps: a mercury lamp, a tungsten lamp, and a deuterium lamp, to be capable of covering a wide range of wavelengths from the electromagnetic spectrum (usually from 300 to 2500 nm). The measurement is done illuminating the sample under study with monochromatic electromagnetic radiation at a 90° angle and collecting information of the transmitted or reflected radiation after it has interacted with the sample.

For the magnetic characterization of the *ZnO* thin films, a magnetic properties measurements system (MPMS) based on the Vibrant Sample Method was used. The external magnetic field is generated with a superconducting coil, usually *Ti/Nb*, which allows it to achieve a high magnetic field variation with relative precision. In the vibrating sample method, the sample is subjected to sinusoidal motion between two pickup coils. The electrical output signal of these coils depends on the induced magnetic field and results with the same oscillation frequency of the sample and with an intensity proportional to the magnetic moments of the sample [261].

Since the magnetic moments fulfill the superposition principle, it is possible to substrain the contribution of the substrate. Assuming an isotropic distribution in each part, the magnetic behavior can be analyzed separately. First, the diamagnetic behavior can be subtracted by a simple calculation of its diamagnetic constant ( $\chi$ ):

$$M_m^{tf}[H] = M_m^{sample}[H] - \chi HV^{dia}, \quad (5-1)$$

where  $M_m^{tf(sample)}$  is the total magnetic moment of the thin film(sample),  $H$  is the external magnetic field and  $V^{dia}$  is the volume of the diamagnetic contribution. For example, for the samples over glass,  $\chi = -5,426(8)$  Oe emu<sup>-1</sup>cm<sup>-3</sup> and  $V^{dia} = width \cdot area_{sample}$  ( $width = 1,12(1)$  mm). This procedure is used to guarantee the isotropic of the magnetization, and separate the contribution of the sample from the substrate. In this way, a volume-normalization can be done and obtain the magnetization of the sample.

### 5.3. Methods and model

Electrical Current Vs. Voltage (I-V) characterization was performed by a Wenner method. A source-meter 2460 High-Current Interactive SourceMeter Instrument from Keithley was used in the 4-Wires configuration. The instrument has an accuracy of  $\pm 10^{-12}$  A and  $\pm 10^{-12}$  V, as source and meter. Electric measurements were made at room temperature and atmospheric pressure. Several cycles were made for I-V measurements, in Figures, only are showed one of each 50.

For the DC electric measurements in bulk, the samples were synthesized on the down electrodes (Fig. 5-1). The top electrodes were placed mechanically (*Au*) or by painting methods (*Ag* and graphite). The gold contacts always have a constant area of  $0,094(8)$  mm<sup>2</sup> and the painted contacts have a bigger contact area of  $\sim 0,74(6)$  mm<sup>2</sup>. The distance between electrodes was fixed at  $5,68(5)$  mm.

Magnetic properties of the samples were obtained through a commercial Quantum De-

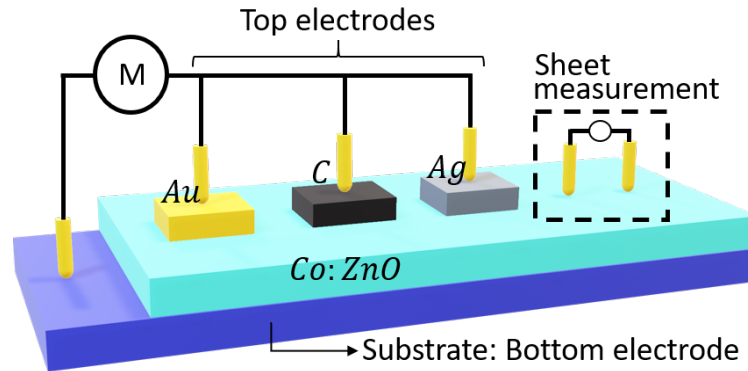


Figure 5-1.: Arrangement of the different upper electrodes in the *Co : ZnO* film deposited on the lower electrode (ITO). On the right side, the configuration for sheet measurements can be observed.

sign magnetometer. This vibrating sample magnetometer has coupled a SQUID sensor and is capable of producing magnetic fields up to 30 kOe using a *Ti - Nb* superconductor coil. Measurements can be made within a temperature range between 50 K and 400 K, with an accuracy of 0,01 K. The equipment has a precision of  $5 \times 10^{-9}$  emu. The magnetic characterization was performed by Magnetization as a function of the applied magnetic field (*M* Vs. *H*) or the temperature. (*M* Vs. *T*). The external magnetic field fixed in 300 Oe for the *M* Vs. *T* measurements. *M* Vs. *H* behavior was studied at 50 K, 150 K and, 300 K. The VSM works at a pressure of  $\sim 2,5$  kPa. Magnetization values were founded by a volume-normalization of the magnetic moments, the thickness and area of the thin films were directly measured by profilometer and optical microscopy respectively.

The optical properties of the samples were obtained using a UV-VIS-NIR spectrophotometer reference T70 + UV/VIS from PG instruments at atmospheric pressure and room temperature.

Assisted laser impedance measurements (ALIS) measurement was performed in the same condition as the performed with DC with a Keysight E4980AL-precision LCR meter. All measurements were achieved with an AC signal of 1 V amplitude over a frequency range from 20 Hz to 1 MHz and with zero DC bias. Each point measurement was an average of 20 trials. Measurements were carried out at room temperature in a dark and electromagnetic isolated room. Before all ALIS experiments, a compensation protocol was performed, first with an open-loop configuration and then with a short-circuit connection, to correct for thermal noise and wiring, capacitance, and impedance leakage signals. Photonic excitation was realized with unpolarized TEM 00 solid-state lasers of wavelength  $\lambda = 632$  nm (power of 149(1) mW mm<sup>-2</sup>) and  $\lambda = 390$  nm (power of 2,89(3) W mm<sup>-2</sup>). All optics were assembled on a vibration-isolated breadboard. The compatible elements were acquired from Thorlabs. Moreover, to avoid parasitic signals, all ALIS facility is attached to an independent ground pole. The impedance noise for darkness or illumination is in the order of  $\sim 9\Omega$ , which is low in comparison to the smallest impedance [262].

All the fitting were performed using the least-squares method with a Levenberg Marquardt algorithm. Also, Magnetization curves were smoothed by an FFT with an 8-point window.

## 5.4. Results and discussions

As it was discussed above, some oxides have a resistive switching property when a voltage bias is applied through them. This determines the applicability in NVM technologies, then the different results obtained are shown based on the information of the current-voltage measurements and the different resistance variations. The theoretical condition to have this phenomenon is simple. An insulator (or semiconductor) between two conductive materials. For this reason, the samples studied were deposited over some conductor substrate (*ITO*, *Gold*, *Ti*, and *Al*). Also, different kinds of the top electrode were used (*Graphite*, *Au*, and *Ag*)

As it was expected, the thin films deposited by DC-Magnetron Sputtering of *ZnO* present a switching in the resistance. Fig. 5-2 shows a bipolar resistive switching behavior, a typical hysteresis of the RRAM. In these kinds of measurements the current has to be limited, cause in another case, the switching is permanent. If the current limit is too low, there are no changes in the resistance, or the resistance difference is too tiny. To have two well distin-

guish states is necessary to have a High Resistance State (HRS) and a Low Resistance State (LRS).

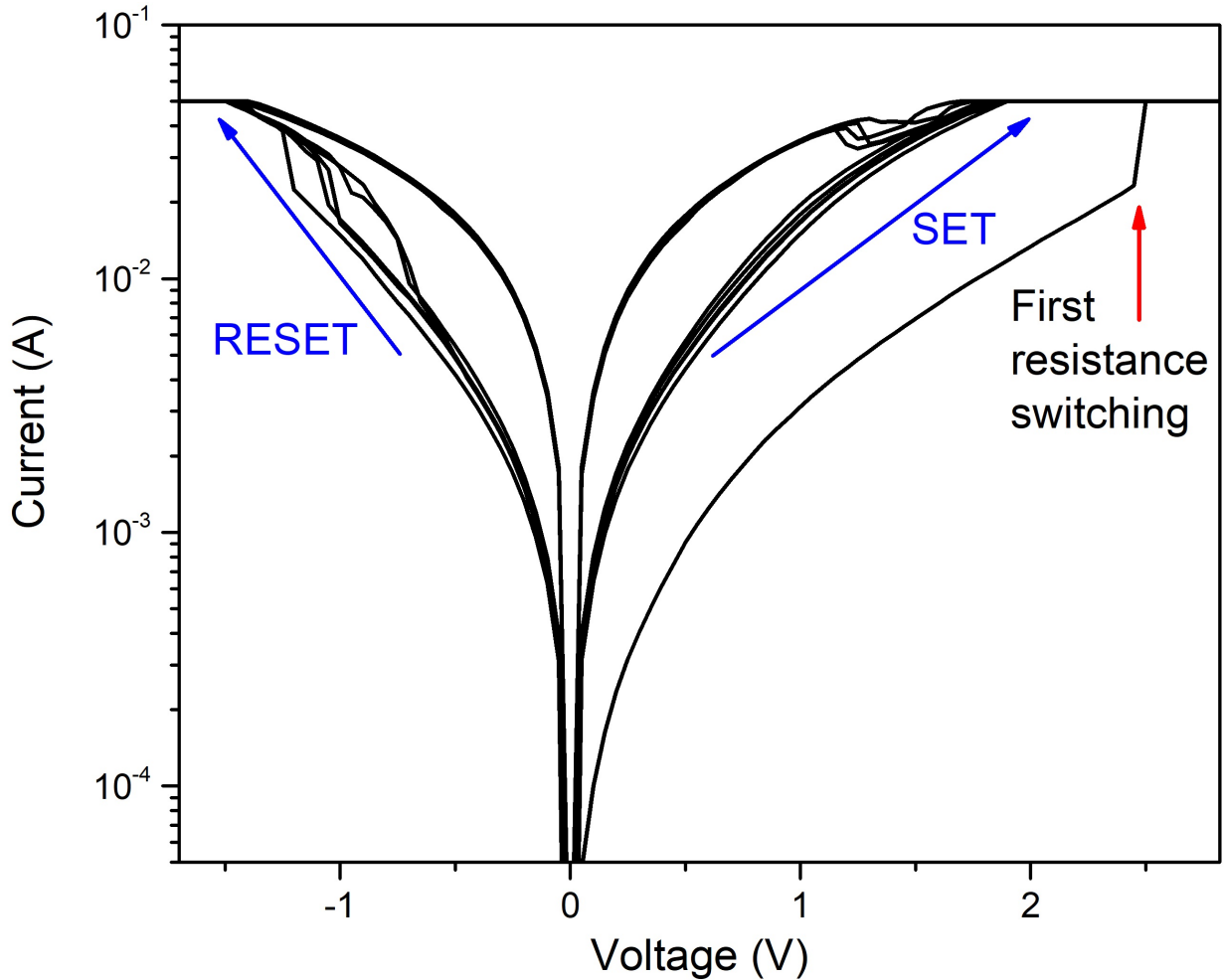


Figure 5-2.: Bipolar resistive switching for a sample of  $Au/ZnO/ITO$  thin film prepared at 423(2) K (250 cycles performed).

Also, in Fig. 5-2 can be observed that the first switching is energetically more expensive, and the consequent cycles have a dispersion around a central value. The central value of voltage in which the resistance change abruptly is known as the SET value or RESET value. The values of SET, RESET, first switching, optimal current limit, and resistance dispersion depend strongly on the synthesis parameters.

So, once the typical I-V curves are well obtained with  $ZnO$  as an insulator, it is time to add some  $Co$  impurities and see the effect in the phenomenon. The first thing that we observe

when the *Co* increases the resistance of the metal-insulator-metal (MIM) structure increase. For this reason, the current limit must be lower to avoid a short circuit. Fig. 5-3(right) shows the SET section of the I-V cycles for samples with different Cobalt target power. In these measurements, the limit current was fixed to 0,2 mA and the voltage bias was varied between -6 V and 6 V. Here the aperture of the curve is different for each *Co* concentration, and is too low for the undoped *ZnO* (black). The SET value at this limit current is very low for the sample with 8,70 % (red) of Cobalt and the pure *ZnO*.

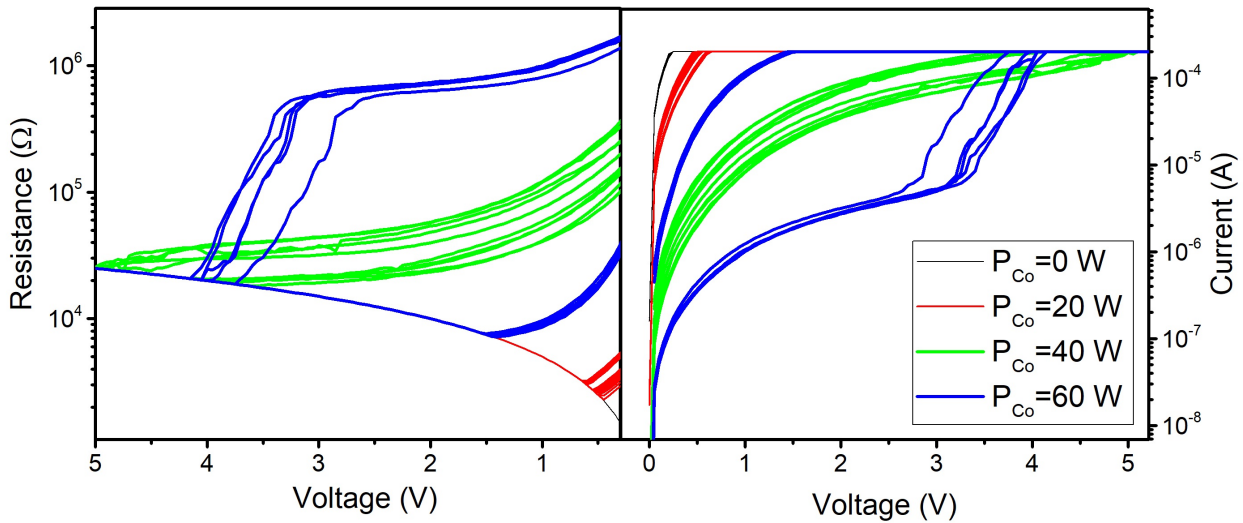


Figure 5-3.: Current (right) and resistance (left) in the switching cycles for *Co*-doped *ZnO* thin films at different  $P_{Co}$  and prepared at 423(2) K. Current limit fix to 0,2 mA in all the 250 cycles.

Fig. 5-3(left) shows the resistance values for the same thin films as the right part. Here, the HR and LR states can be easily identified for the sample with *Co* at 14,39 % (blue). A lot of dispersion is observed in the sample with 13,19 % of Cobalt and it is difficult to distinguish the two resistance states. At this limit current, the lower concentrations of *Co* seems impossible to work as NVM.

Now, this limit current does not work well for every Cobalt concentration. So, a variation of this parameter was done from  $5 \times 10^{-3}$  mA to 100 mA in each sample and the maximum hysteresis areas were saved. Fig. 5-4 shows the I-V cycles for the best current limit when the free parameter is the Cobalt concentration. In this case, all the samples have well-separated resistance states but once again is the thin film with the highest *Co* concentration the optimal NVM candidate.

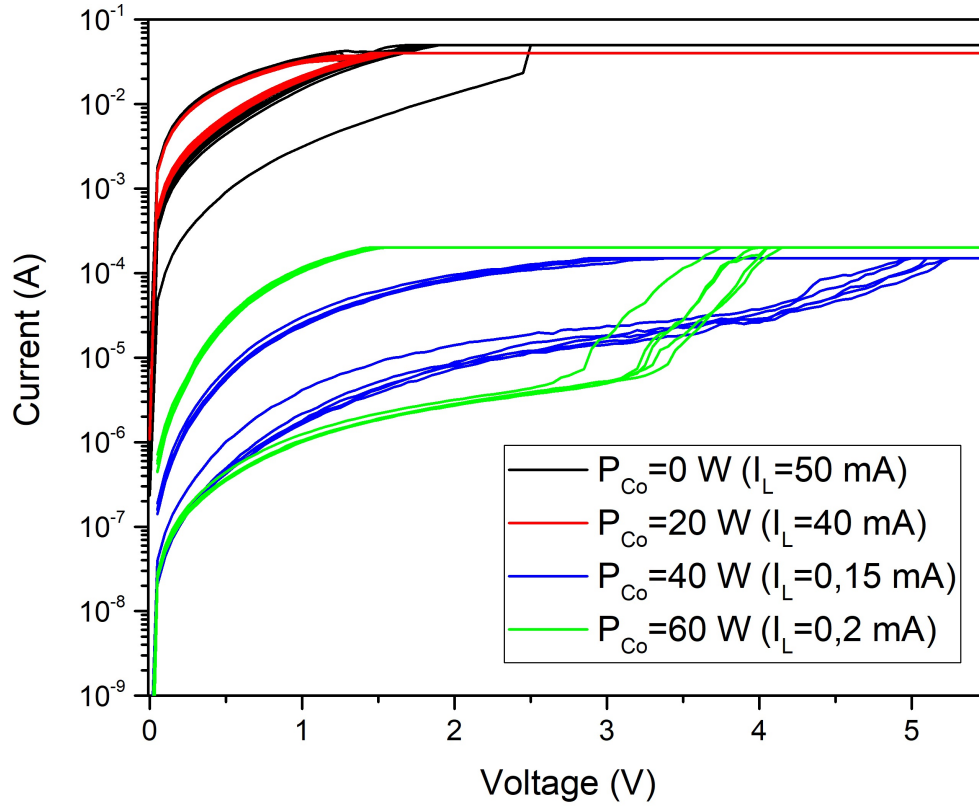


Figure 5-4.: Current-Voltage SET cycles (250) for the different  $Co$  concentrations at their optimal (op) limit current.

The application and reliability of the device need to have into account the electrical power that is necessary for the set-reset process. Table 5-1 shows the average necessary powers to set and reset the memory cell. In an electronic device, no I-V curve is performed, quite the opposite, a pulse of fixed power is used to configure the bit and a lower pulse is used to read the value. This process is faster than the I-V measurement, and the time required to set or reset the value is known as the frequency of the memory. The values in Table 5-1 were calculated as the average area of the cycles in the set and the reset of the memory cell. The first values are for the optimal limit current and the last ones for  $I_{max} = 0,2$  mA. A decrease in the power is found when the Cobalt concentration increases, due to the lower optimal current, that comes from the higher resistance at higher impurities concentration.

Another important parameter in the commutation MIM system is the thickness of the insulator. In Fig. 5-5 a comparison between the resistance states at optimal (op) limit current and fix it at 0,1 mA. Here can be observed the previous argument, a fixed current limit is not the best option for all the samples, that limit should change with every sample. The basic idea of a reliable NVM device starts with a resistance states such that their dispersion is much lower than their resistance gap. The fixed limit current meets this necessity only

Table 5-1.: Powers of SET and RESET for different Cobalt concentration and current limit.

$P_{Co}$ W	$Co/Zn$ % at.	$I_{max}$ mA	Area SET mW	Area RESET mW
0	0	50	18, 20(1, 43)	14, 17(2, 40)
20	8, 7	40	11, 35(82)	10, 59(89)
40	13, 19	0, 15	0, 203(33)	0, 105(22)
60	14, 39	0, 2	0, 549(29)	0, 014(9)
0	0	0, 2	0, 0025(1)	0, 0005(1)
20	8, 7	0, 2	0, 015(2)	0, 025(1)
40	13, 19	0, 2	0, 198(29)	0, 015(13)
60	14, 39	0, 2	0, 550(29)	0, 014(9)

once in a while. So, make sense to study the other requirements only with the optimal limit current. The optimal thickness for the electrical properties, the highest resistance gap with the lowest dispersion, was  $\sim 130$  nm ( $t_d = 15$  min).

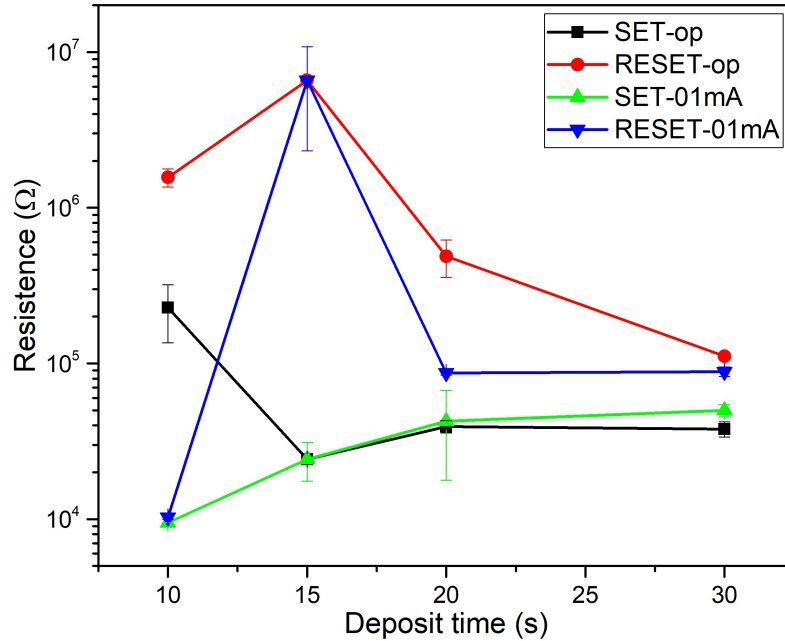


Figure 5-5.: Average LRS and HRS as function of the deposit time for  $Co$ -doped  $ZnO$  at 13, 19 %. The limit current was the optimal (red and black) or fix at 0, 1 mA (blue and red). Error bars represent the state dispersion of the average over 250 cycles.

Now, it is possible that the dispersion increase with the re-writing of the memory. Mostly commercial memories guarantee at least 10 000 cycles until 100 000. This can be studied from the increasing of the dispersion with the cycles, and extrapolate until the dispersion reach a considerable fraction of the gap.

Fig. 5-6 shows the low and high resistance states as a function of the number of cycles. The state was set and reset by fixed power pulses according to the Table 5-1 and measured at 1 V after the bit was written. The behavior oscillates around central values, and the dispersion is around 1,5 M $\Omega$  in both cases. Due to the higher resistance gap, the device is still reliable, and no deformation is observed after the 16000 set and reset processes.

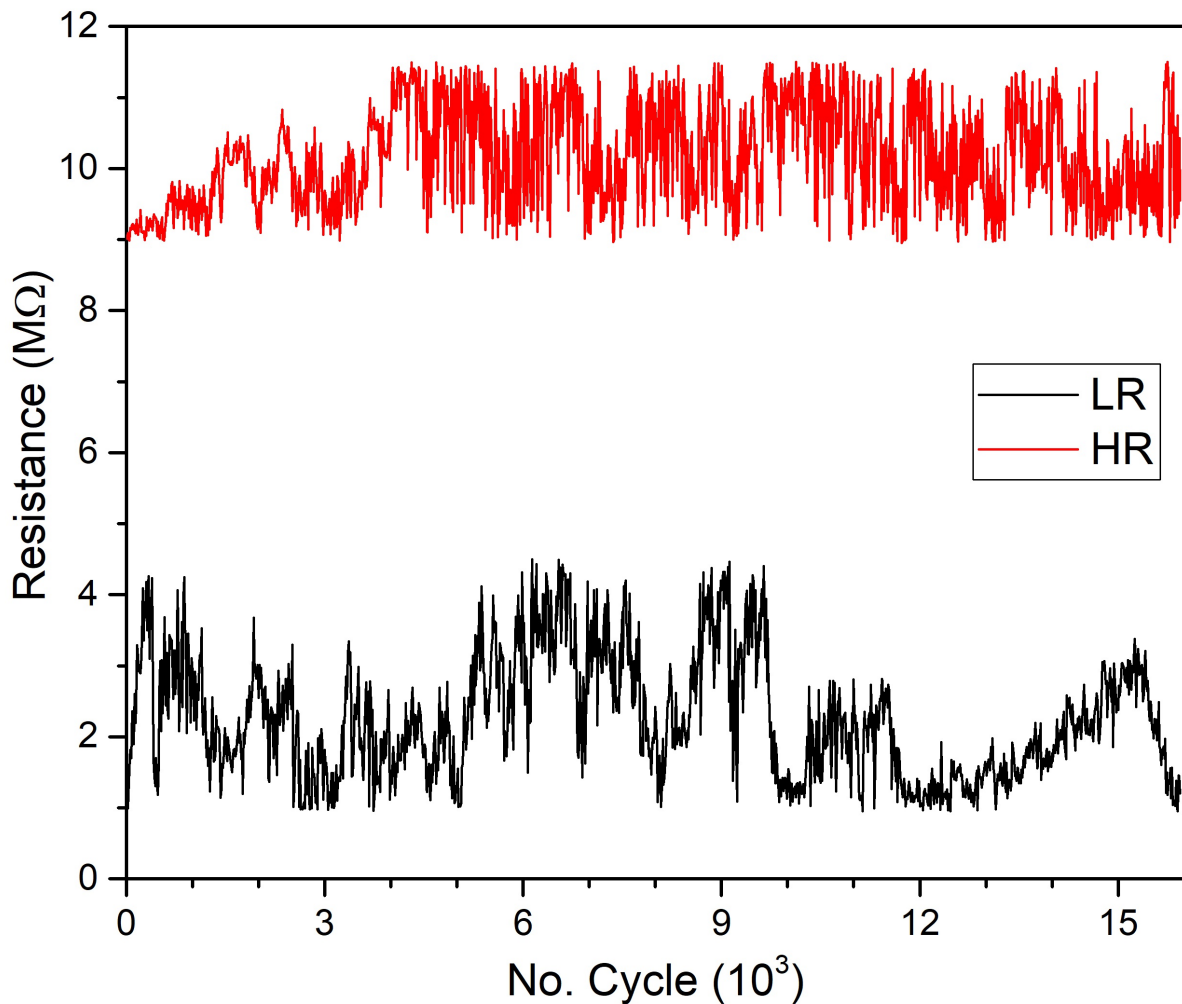


Figure 5-6.: Low and high resistance states as a function of the number of cycles for a *Au/Co : ZnO/ITO* system.

Once the device has two well-distinguish resistance states, the next important requirement for an NVM is its non-volatile condition. For this test, the memory cell was set it up in the



LRS, and some measurements along the time were performed. Fig. 5-7 shows the behavior of the LRS as a function of the time for  $10^5$  seconds. Green triangles show the measurements and the dash-line shows the average HRS measured before the set, and after the reset of the commutation system. The fluctuations in the time are lower than the fluctuation in the cycles, which gives a lot of confidence in the save of the information, even extrapolating to the 20 years of the set, the resistance state still in the accepted range.

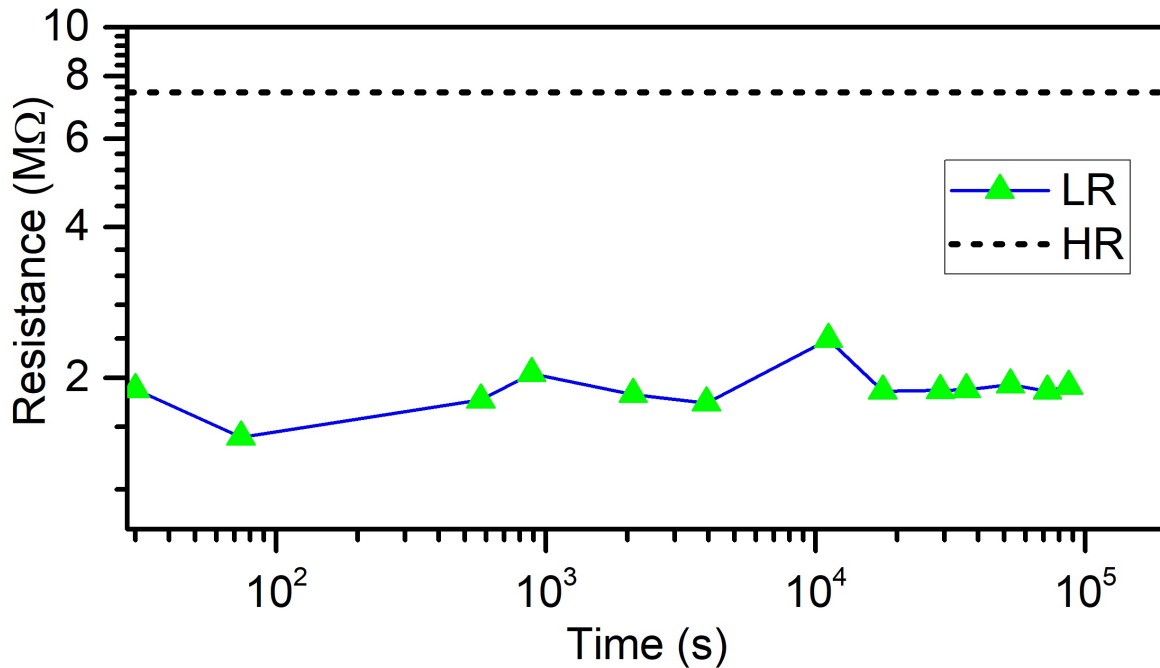


Figure 5-7.: LRS and average HRS as a function of the time for a *Au/Co : ZnO/ITO* system.

The device can be affected by an external source of light and change its resistivity states. For this reason, it is important to check if there is some energy for which the photons are absorbed by the material. Fig. 5-8 shows the absorbance spectrums as a function of the Cobalt concentration, an increase in the absorbance is observed with the *Co*, as expected [263]. Also, comparing the pure *ZnO* with the doped samples appears some slight peaks in the spectrum. These peaks are marked in the figure and correspond to optical excitations of the d-d bond of the Cobalt [264]. This bond is a particularity of the *Co* oxidation state +2, that could confirm a substitutional impurity into the *ZnO* matrix.

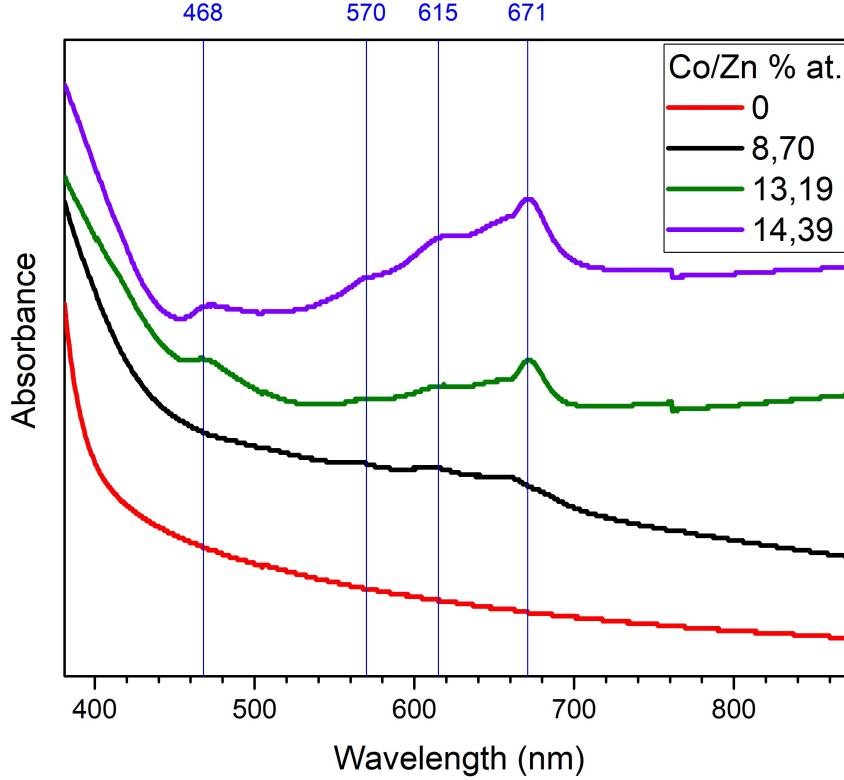


Figure 5-8.: Absorbance spectrum for different Cobalt concentrations in  $Co : ZnO/Glass$ .

From the absorbance spectrums, using the Beer-Lambert law [265] the band-gap could be calculated. Table 5-2 shows the values of the forbidden band for the samples over Glass, and over ITO. A UV-shift is observed when the Cobalt increases in the structure. The fact that the shift never collapses is a good clue of the no formation of secondary phases [252].

Table 5-2.: Gap values for the different  $Co$  concentrations in the  $ZnO$  thin films over glass and ITO.

$P_{Co}$ W	$Co/Zn$ % at.	Gap-Glass eV	Gap-ITO eV
0	0	3,19(6)	3,26(3)
20	8,7	3,26(3)	3,31(14)
40	13,19	3,28(1)	3,29(2)
60	14,39	3,45(1)	3,29(4)

Now there is a particular interest in a model to explain the behavior inside the bulk in the high resistance state. It is well known that the low resistance state behaves like an ohmic material. But the reason why the resistance switching and how it can be modeled

remains a question. To have a first approach to solve these questions was studied the electrical response of the material through an AC electromagnetic field. The amplitude of the complex impedance of the bulk and the phase change in the resultant signal was measured as a function of the signal frequency. Fig. 5-9 shows the impedance amplitude and phase for four different concentrations of Cobalt (Bode plot). The bulk impedance increase with the impurity concentration, in amplitude and phase. The amplitude behavior has the same start and in the high-frequency zone are subsequent endings.

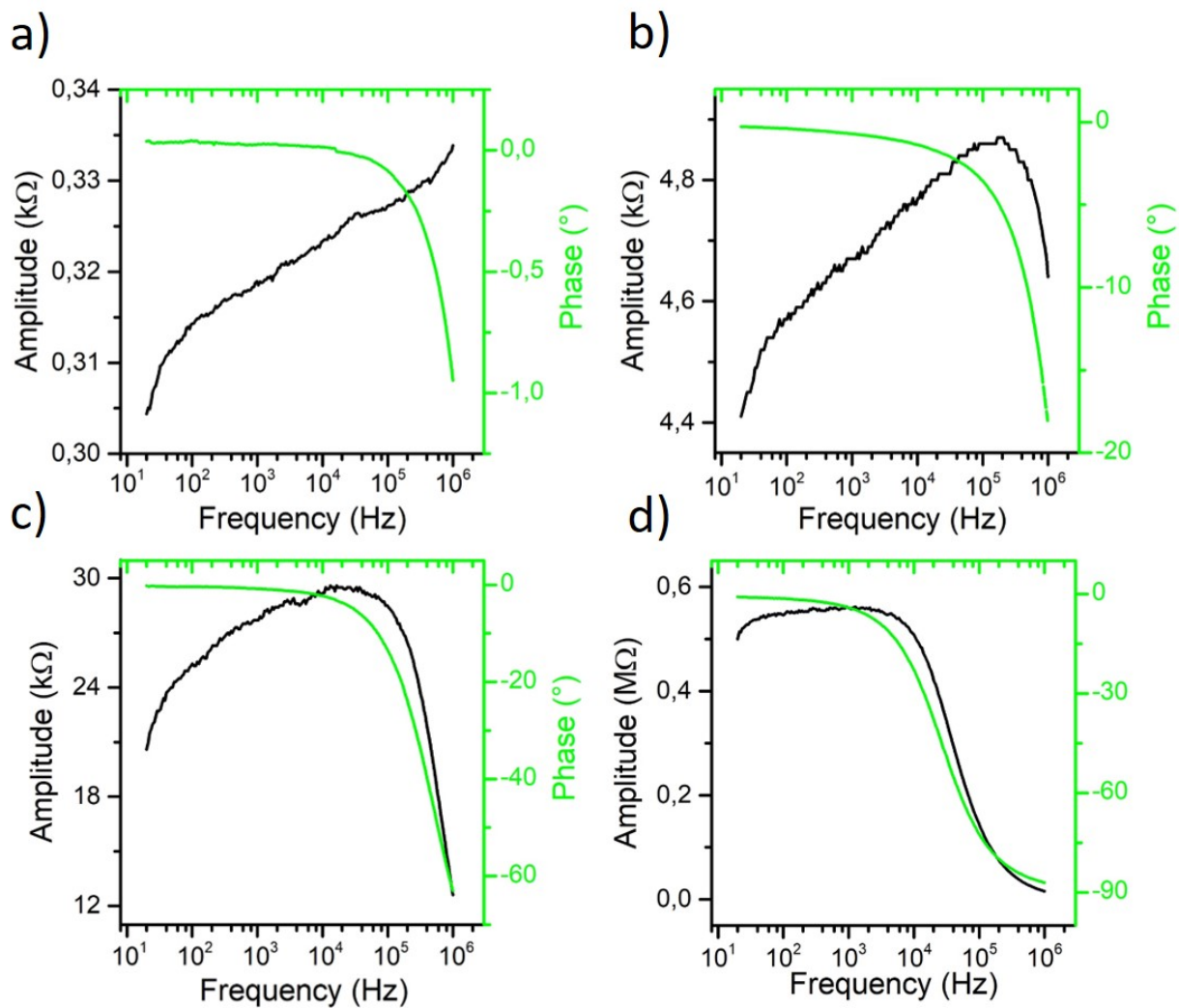


Figure 5-9.: Bode plots for the impedance bulk measurement of  $Au/Co : ZnO/ITO$  systems at different Cobalt concentrations: 0 % at. (a), 8,7 % at. (b), 13,19 % at. (c), and 14,39 % at. (d).

That can be observed better in a normalized Nyquist plot (Fig. 5-10), here all the  $Z$  values are normalized by the maximum value of the real part ( $Z_0$ ). Here can be observed how each curve appears to be completed by the next concentration, starting as a sim-

ple Capacitor-resistance [266] for the undoped material, and become showing a resistance-capacitor//resistance typical behavior when the Cobalt concentration increases [267, 268].

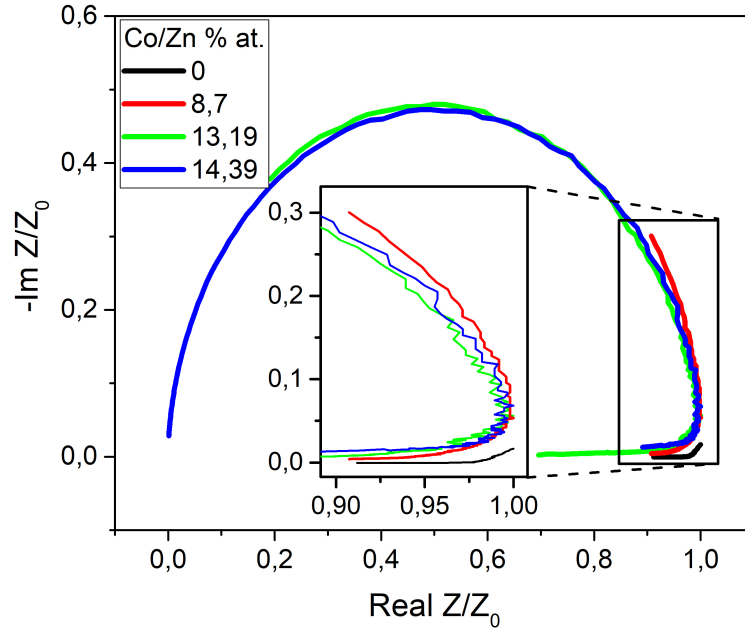
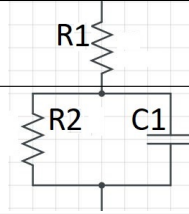


Figure 5-10.: Normalized Nyquist plot for different Cobalt concentrations in the  $Co : ZnO/ITO$  thin films. The inset shows the low frequencies range for the highest concentration of Cobalt.

For the doped samples, Table 5-3 shows the values of the equivalent circuit for each case. The electrical model was chosen as a resistance in series with parallel resistance and capacitor, the series resistance represents the facility of the electric wire in the switching most accepted model, and the parallel circuit represents the accumulated ions in each electrode as a real capacitor. The series resistor increase with the magnetic doping agreeing with the previous electric measurements, while the capacitor remains almost constant, appearing to be an effect of the contacts, the second resistor increases dramatically with the Cobalt concentrations, resulting in a response to higher frequencies. Previously, the optical absorption and consequently the gap of the thin films were determined as a function of the magnetic doping, using these results, two optical stimuli could give information of the samples, the UV/Violet and the red. The first one should affect the whole thin film, with a bigger proportion at higher gaps, and in a proportional way to the  $ZnO$  quantity in the sample. Fig. 5-11(left) shows the impedance amplitude reduction (better conductivity) and the phase shift ( $\theta_{UV} - \theta_{dark}$ ) as a function of the frequency. The phase shift increases at high frequencies and has a peak for the higher impurity concentration, appearing that once again is the same behavior in all samples, with just a shift in the frequencies. On the other hand, the red

Table 5-3.: Equivalent circuit scheme and values for the different Cobalt doped ZnO thin films.

	Zn/Co (% at.)	R1 (MΩ)	R2 (Ω)	C (10 <sup>-11</sup> F)
	8,7	4,89(12)	9,37(2) × 10 <sup>-13</sup>	1,15(2)
	13,19	28,67(43)	572,40(2,40)	1,21(3)
	14,39	549,81(1,30)	940,25(6,89)	1,06(1)

stimulus only has an evident effect in the highest Co concentration (Fig. 5-11(right)). The other samples present a slight improvement in their conductivity, but no correlation with the magnetic concentration was founded. The thin film prepared at 60 W of Cobalt power, present some erratic peaks in the amplitude reduction, suggesting that probably different bonds are present in the material.

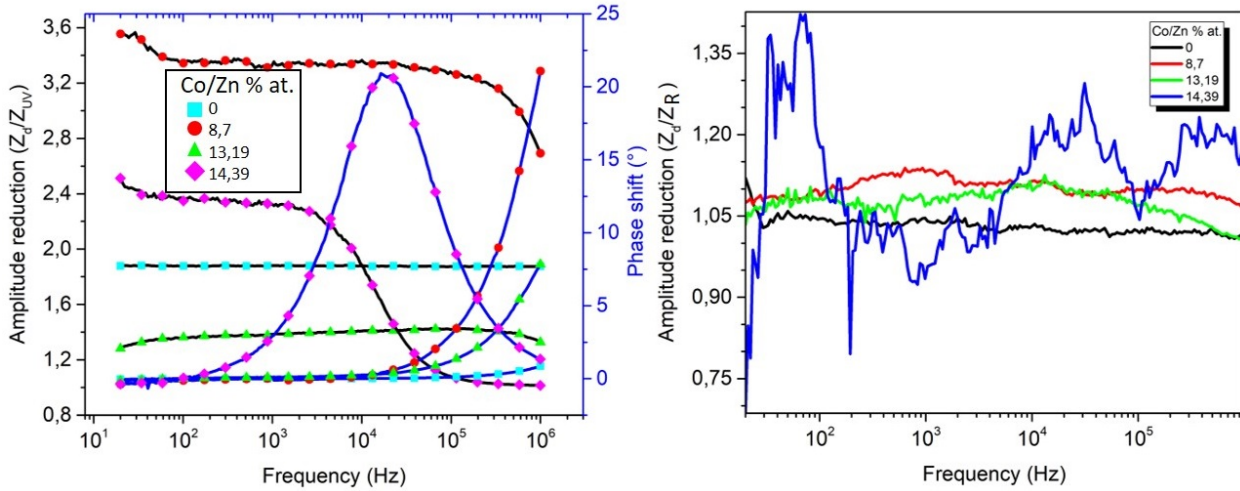


Figure 5-11.: ALIS results of the *Au/Co : ZnO/ITO* systems: Amplitude reduction and phase shift for the sample illuminated with  $\lambda = 390$  nm (left) and  $\lambda = 632$  nm (right).

The sheet resistivity was studied to determine the superficial electric mobility in the material as a function of the Cobalt concentration. Like the bulk resistivity, the sheet resistivity increase in several magnitude orders with the magnetic impurities, showing a phase transition from a pure semiconductor to an insulating alloy. Finally, the effect of the top contact was measured in term of the necessary power to set[reset] the resistance state in the material, at 0,15 mA as the limit current, the power values (mW) decrease significantly from 0,203(33)[0,105(22)] for the Au contact to 0,016(3)[0,005(3)] and 0,015(2)[0,043(12)] for Ag and graphite top contact respectively. This could be very good to have an efficient material for an electronic application.

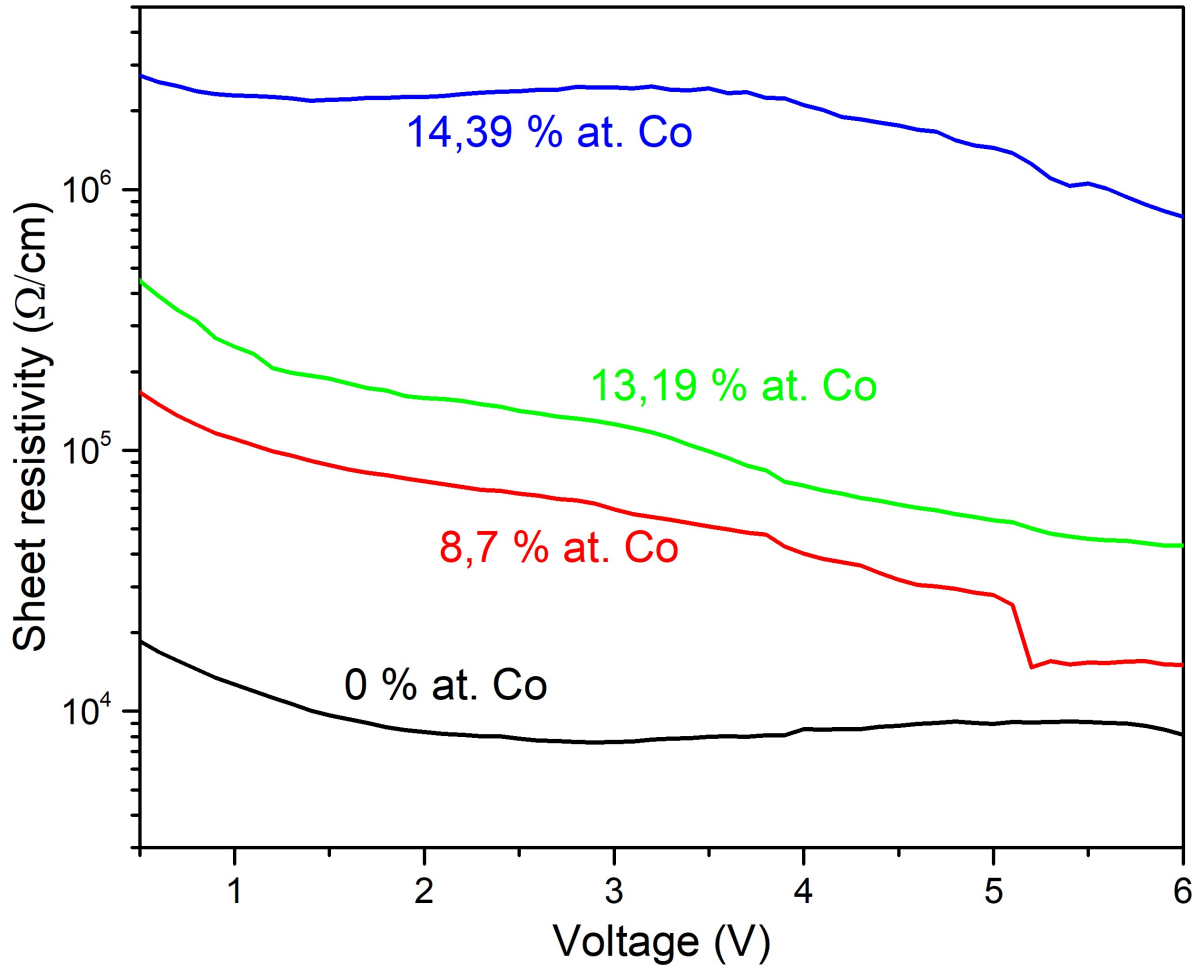


Figure 5-12.: Sheet resistivity of  $Co : ZnO$  for different Cobalt concentrations in the 0-6 V range.

To finish the experimental results, the magnetic properties of the  $Co$ -doped  $ZnO$  thin films were studied. Here, the goal is to achieve a relevant magnetic behavior at room temperature, full-filling the DMS conditions. In the experimental details of the thin-films synthesis, was mentioned that posterior annealing to the deposit is a requirement to have remarkable magnetic properties. Fig. 5-13 shows a comparing in the magnetization when the sample is annealed at 473(2) K. The effect of the annealing is evident, at low temperatures when the annealed sample has a strong competition between a ferromagnetic interaction and a diamagnetic contribution. Also, at 150 K the magnetization values are lower for the annealed sample. Fig. 5-13.c shows a zoom where is observed a slight hysteresis at 150 K with a tiny remainder magnetization and a considerable coercive field.

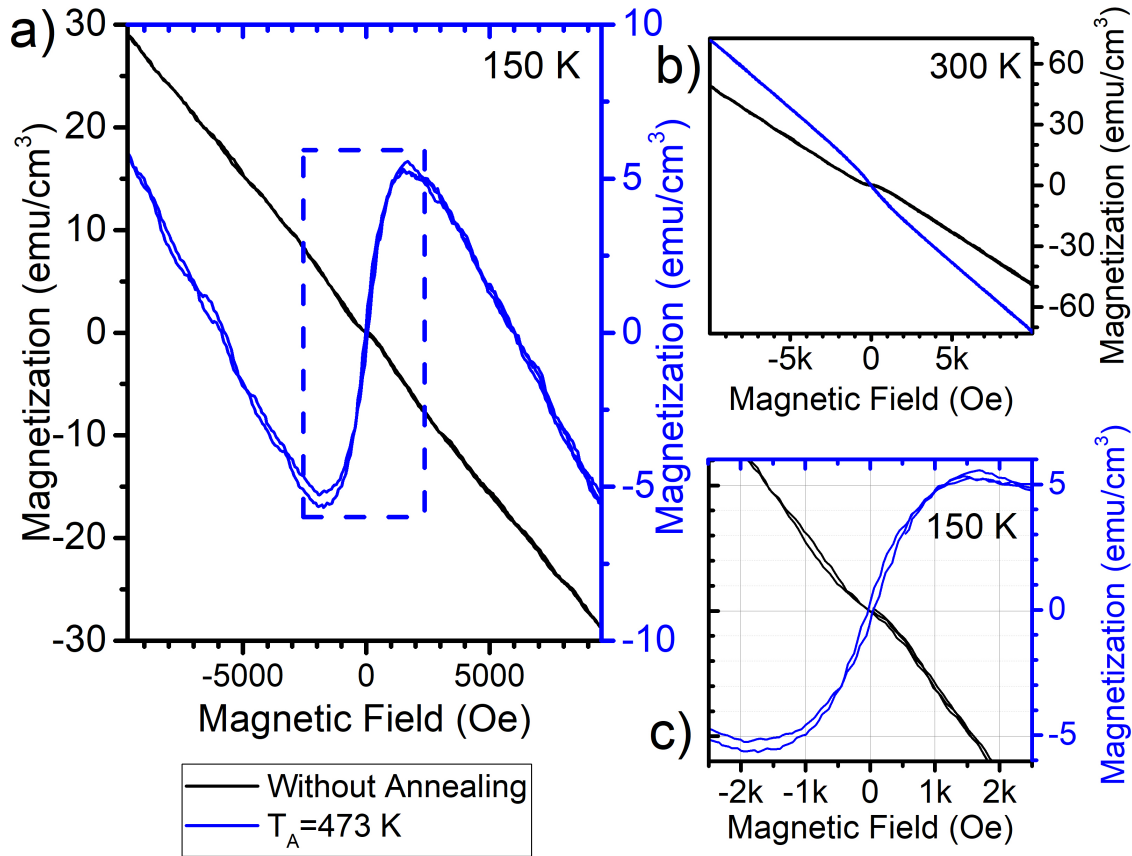


Figure 5-13.: Annealing effect in the magnetization as a function of the externally applied field. Measurements realized at 150 K (a, c) and 300 K (b) of *Co*-doped *ZnO/Glass* at 13, 19 %. Sub-figure c shows zoom-in low fields.

However, at room temperature (Fig. 5-13.b) no hysteresis was observed. Trying to achieve this goal, the previous results were analyzed. From the theoretical study, the Cobalt substitution in the wurtzite structure results in an efficient DMS. Also, the XRD results show that the amorphous soda-lime glass maybe is not the best substrate to introduce the doping. So, remember that the samples deposited on  $Al_2O_3$  substrate were the most crystalline, is a good idea to study the magnetic properties on these thin films. Nevertheless, the 100% diamagnetic contribution of the glass is easy to take off, and there is some uncertainty about how to have only into account the contribution of the thin films synthesized over  $Al_2O_3$ .

Fig. 5-14 shows the magnetization of the  $Al_2O_3$  substrate as function of the magnetic field. Also, it shows the magnetization without diamagnetic contributions. The diamagnetic constant was calculated assuming a linear combination of several magnetization sources. As the behavior is almost diamagnetic in high fields, the slope of the M-H curve was calculated by a linear fit.  $\chi = -4,58(3) \times 10^{-5} \text{ emu cm}^{-3} \text{ Oe}^{-1}$  was the diamagnetic constant found for  $Al_2O_3$ . Following the same procedure as the glass's contribution, the diamagnetic contri-



bution of  $Al_2O_3$  was subtracted from all the subsequent H-M measurements ( $\chi = -4,59(3)$  emu Oe $^{-1}$ cm $^{-3}$ ).

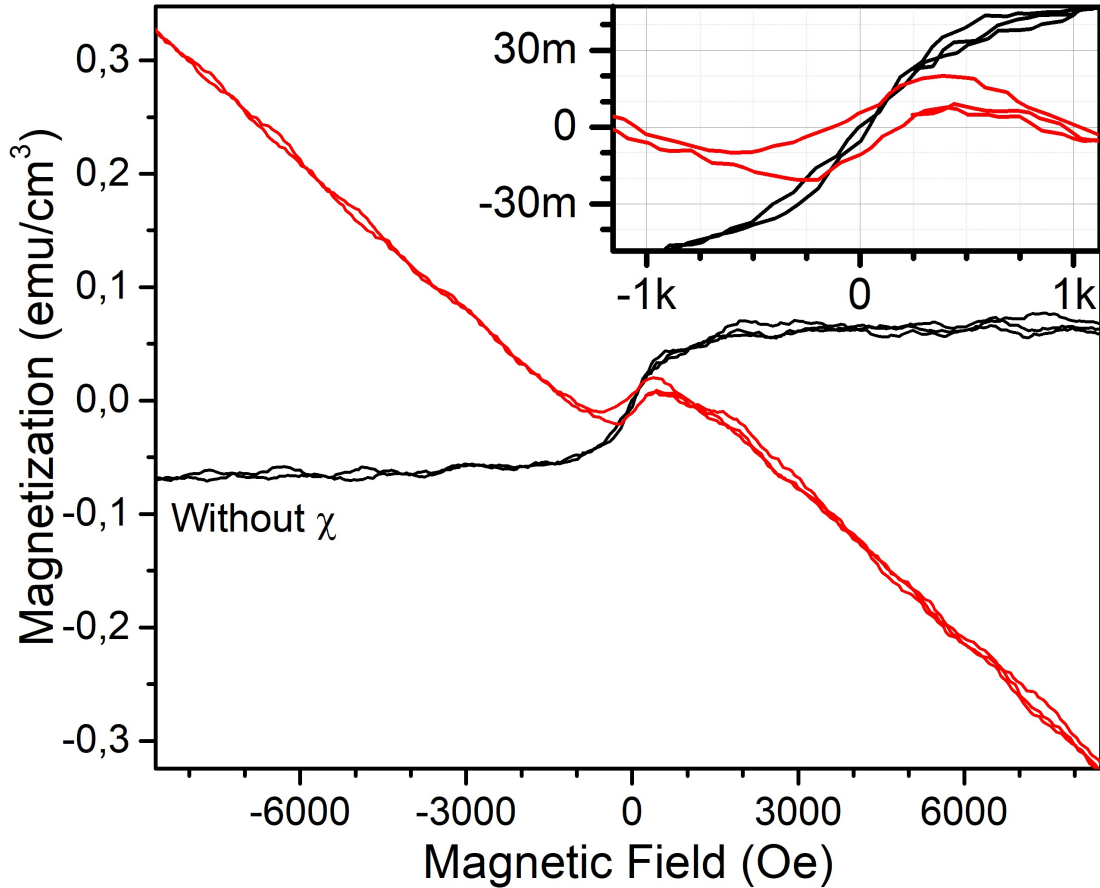


Figure 5-14.: Magnetization of the  $Al_2O_3$  substrate as function of the magnetic field (red line) and No-diamagnetic magnetization contribution (black line). The inset shows these magnetization at low external fields.

The inset in Fig. 5-14 shows a weird hysteresis in the original measurement of the substrate, however, it disappears when the diamagnetic contribution is subtracted. Now, without the diamagnetic contribution of the substrate, the interest is the focus on the magnetization effect of the Cobalt concentration. Remembering that  $Co$  ions increase his presence in the semiconductor matrix at highest  $P_{Co}$  ( $P_0 = 0\%$  at.,  $P_{20} = 8,70\%$  at.,  $P_{40} = 13,19\%$  at., and  $P_{60} = 14,39\%$  at.). Fig. 5-15 shows comparative M-H curves for each different  $P_{Co}$ , those powers corresponds to relative Cobalt concentration according to Auger measurements.



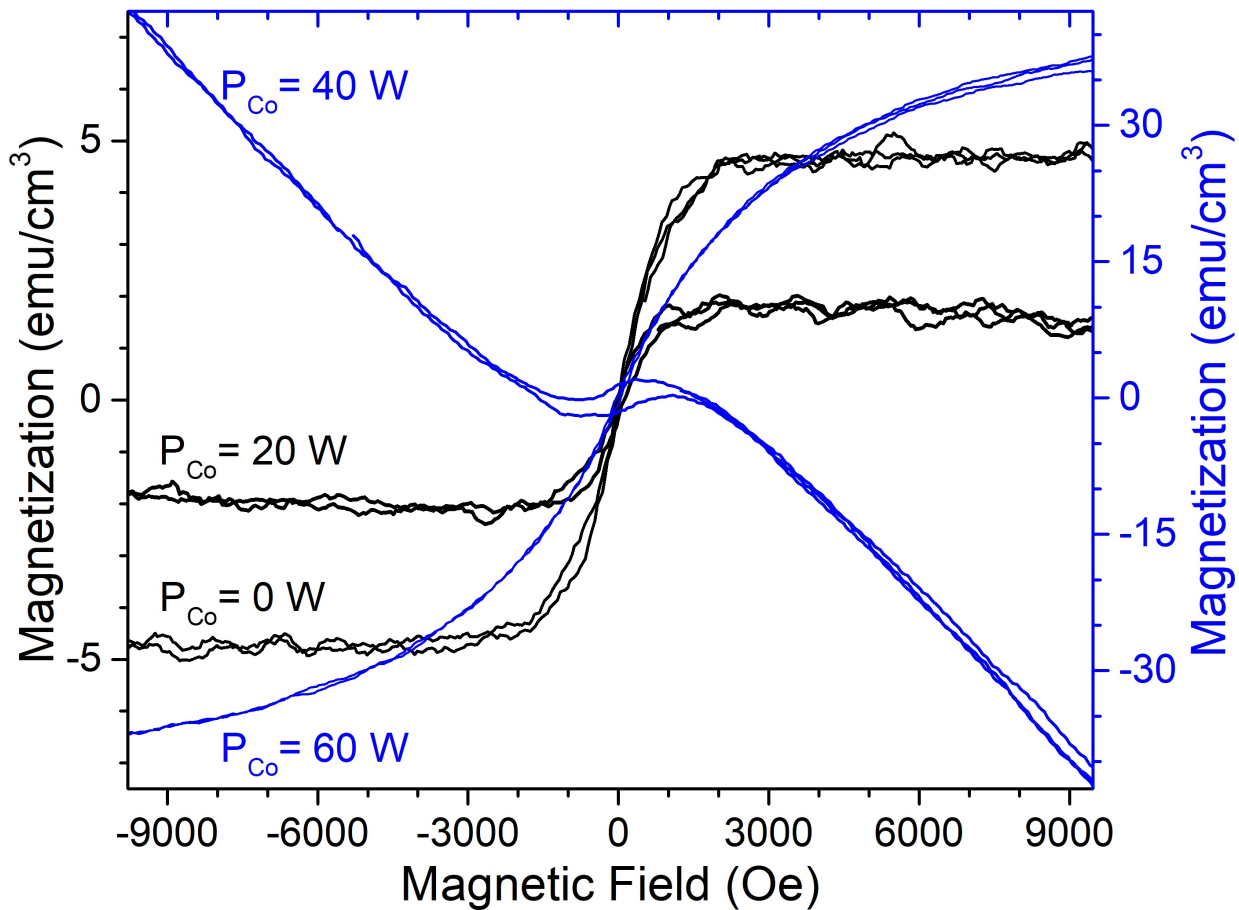


Figure 5-15.: M-H curves for each different  $P_{Co}$  at 300 K. Blue(black) lines correspond to the blue(black) magnetization scale.

The two highest concentrations have significantly higher magnetization (blue scale). The pure ZnO seems like a paramagnetic that saturates very fast. A tiny hysteresis is observed in the thin film with Co at 8,70% ( $P_{20}$ ) and like the  $Al_2O_3$  substrate, the  $P_{40}$  exhibits a disoriented hysteresis. The change in the shape of this magnetization is evident, cause a strong diamagnetic contribution appears ( $\chi = 5,66(2) \times 10^{-3} \text{ emu cm}^{-3} \text{ Oe}^{-1}$ ). The hysteresis here has a remainder magnetization of  $1,9(2) \text{ emu cm}^{-3}$  and a coercive field of  $1,31(17) \text{ KOe}$ . With the highest Co concentration, the interaction between Co defeats the diamagnetic contributions and shows a long and thin hysteresis. However, is not visible at this scale. Fig 5-16.b shows a scope at low fields of the hysteresis. It has a lower remainder magnetization ( $0,9(3) \text{ emu cm}^{-3}$ ) and coercive field ( $450(30) \text{ Oe}$ ). When the temperature down (Fig5-16.a) the hysteresis loop still thin, but is more defined and has a larger coercive field. Fig. 5-16 shows the FC M-T curve at 300 Oe of this sample. From the FC curve can be concluded that for this sample, the temperature is not an order parameter at least in the 50K-300K range.

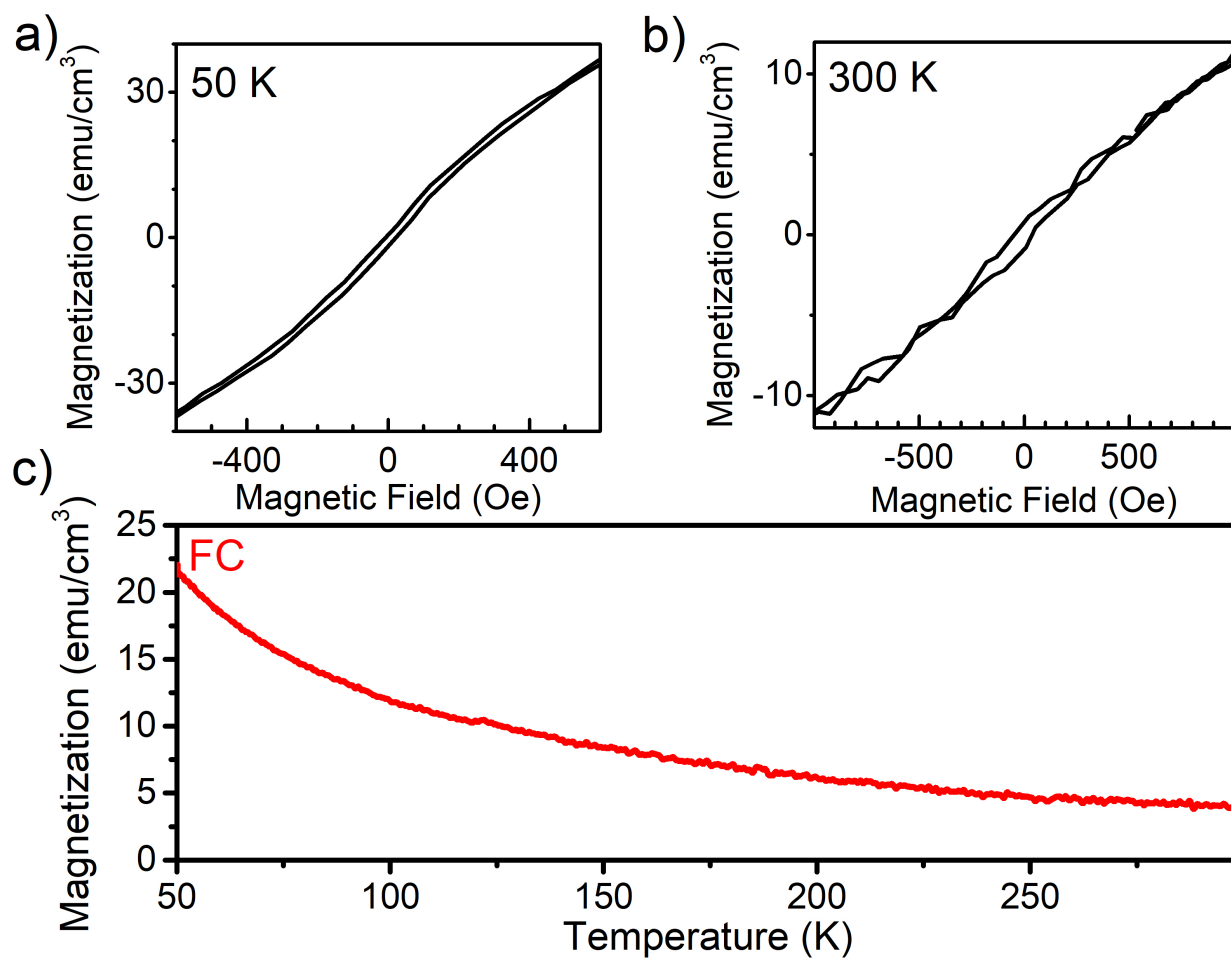


Figure 5-16.: Magnetization as a function of the external field at 50 K (a) and 300 K (b), for the  $Co:ZnO$  thin film doped at 14, 39%. (c) FC curve at 300 Oe for the same sample.

# 6. Conclusions and perspectives

## 6.1. Conclusions

*ZnO* and Cobalt doped *ZnO* thin films were successfully fabricated by DC-magnetron co-sputtering method. For this purpose, there were used Cobalt and Zinc oxide targets in a non-reactive sputtering machine with Argon as plasma gas. Several samples were prepared with different synthesis parameters (Cobalt power, deposit time, substrate temperature, chemical nature of substrate), with a thickness of the thin films between 50 and 190 nm, and optically transparent.

Based on *ab-initio* calculations and mean-field Heisenberg model, the effect of the  $V_O$  in *Co*-doped *ZnO* is principally an electron spin density redistribution around the  $V_O$ , which depends strongly on the *Co*- $V_O$  distance and the ratio of concentrations *Co* :  $V_O$ . All different  $V_O$ -configurations presented a lower total magnetization (per *Co* atom) than their equivalents without vacancies. But the increase of *Co* –  $V_O$  distance reduces the local magnetic moment on the *Co* atom, which is due to the antiferromagnetic coupling between *Co* and  $V_O$  impurity for the lowest distances *Co* –  $V_O$ . Formation energy shows an increment when the *Co* concentration and the *Co* –  $V_O$  distance raised but the average magnetization per Cobalt seems to not correlate with the *Co* concentration. However, a different effect was observed a second oxygen vacancy was added close to the first one. In the 1 : 2 ratio case, we found a maximum effect radius  $\Delta_2 \leq 3.5\text{\AA}$ . When the second  $V_O$  was closer than that, the electron spin distribution around Cobalt impurity was concentration depended, increasing or decreasing the magnetization ( $TMM/Co$ ). In all configurations, magnetic moments were mainly generated by *Co* – 3*d* orbitals and the presence of  $V_O$  helped to the ferromagnetic stabilization with high Curie temperatures when the *Co* – *Co* distance was lowest. Charge spin distribution allowed to note that the  $V_O$  presence increases the antiferromagnetic electronic spatially distributed. This explains the  $TMM/Co$  decrease by the  $V_O$  helped the ferromagnetic interaction between Cobalt atoms, working as an exchange bridge.

The Cobalt distribution as a function of the target power allowed the selection of the optimal samples for the DMS condition of no secondary phases in the semiconductor matrix. Also, a logarithmic tendency was found in the thickness of the samples as a function of the deposit time and an increase of it with the Cobalt concentration was evidenced. Through Auger spectroscopy, a random distribution of the Cobalt into the bulk was found, and quan-

tification of the atoms was performed. The Cobalt concentrations, relative to the Zinc in the studied samples, was on average 8,70 %, 13,18 %, and 14,38 % for the powers of  $P_{Co} = 20W, 40W, 60W$  respectively. In the diluted matrix, was found a 0,49 ratio for the  $O : Zn$  atoms, implying several oxygen vacancies in the structure, the possibility of  $Zn$  clusters was denied by XRD measurements and the high electrical resistance.

Structural characterization revealed the typical wurtzite phase of  $ZnO$  and growth in the substrate preferential planes. Secondary phases of  $Co$  were not found by XRD measurements. However, a decreasing shift in the position of the peaks was evidenced when the  $Co$  concentration increases. No relevant change in the diffraction patterns was observed when the substrate temperature increased, probably due to the fact of the *in situ* annealing of a higher temperature. Same reason for the no relevant changes in the topography of the thin films deposited at different temperatures.

A correlation between the chemical nature of the substrate and the topography was observed in the micrographs by SEM. To study the morphological effects of the Cobalt concentration, AFM measurements were performed. Here, a  $Co$  tip was used to additionally study the magnetical response of the surface. The grain height increased in the function of Cobalt and some remarkable magnetic grains were identified in the highest concentrations. For the 15% Cobalt sample, a magnetic distribution in the surface was observed, where the upper RMS/M-RMS was present.

The resistive switching phenomenon was observed in the pure  $ZnO$  and  $Co : ZnO$  thin films. The higher electric power of the first set is in agreement with the proposed models for the effect. It showed a strong dependence with the current limit of the set-reset process and each sample exhibited an optimal current limit, *i.e.* the current in which the high and low resistance states are more separated and less dispersed. The resistive gap between the LRS and the HRS is enough to propose a memory application, which increases with the resistance values and the  $Co$  concentration. Also, the required electrical power to set or reset the bit in the memory was lower when the magnetic impurities increases.

The optimal deposit time for the memory application was 15 minutes, where the relation between the HRS-LRS separation and the dispersion of the measurement was the best. The reliability of the device was tested with 16000 cycles and dispersion of  $\sim 3 M\Omega$  in each resistive state was found. The separation of the states is enough to take this dispersion without jeopardizing the reliability. Also, the condition of non-volatile was tested, performing measurements for  $10^5$  seconds with only one set pulse. The time-behavior of the set state was steady and it guarantees the duration of the data for a long time (can be extrapolated until the standard 10 years from the market).

Optical characterization shows an increase in the opacity of the thin films with the Cobalt concentration and exhibited some absorption peaks associated with *Co* d-d bonds in the structure. Through the Beer law, the energy forbidden band was calculated as a function of the impurities concentration. It had a UV-shift that increases with the absorption.

Also, magnetic characterization of the samples showed hysteresis loops in the magnetization at room temperature. The crystallinity of the samples played an essential role in the magnetic behavior, represented by the annealing requirement and the substrate dependence. The magnetization hysteresis had a remainder magnetization of  $1,9(2)$  emu  $\text{cm}^{-3}$  and a coercive field of  $1,31(17)$  KOe for the sample with 13,19% of Cobalt. From the FC curve can be concluded that for this sample, the temperature is not an order parameter at least in the 50 K-300 K range.

Finally, due to the coexistence between the magnetic and the electric properties of the *Co*-doped *ZnO*, several spintronic applications can be performed using these thin films as precursors. Using resistive switching and remanent magnetization, a higher-density memory cell can be formulated with a layer of the undoped material between two films of the doped one, as Andrew W. Stephan et. al. proposed theoretically [269]. Also, with the properties showed it is possible to formulate spin-valves [270] or spin-polarized transistors, that have serious troubles with the Curie temperature of the current spintronics [271].

## 6.2. Perspectives

Due to the fact that the *Co* : *ZnO* is a well-studied material, the principal perspectives of this work are about the applications. However, the industrial closeness of the sputtering technique, makes it deserve a deeper analysis into the growth and crystalline structure formation. Also, the explanation of the ferromagnetic behavior in this material remains an open question.

The possible magnetoresistance effect in this material could bring it close to a spintronic application, also probably the magnetic impurities under external magnetic fields could increase the frequency of the device, as in the case of Giant magnetoresistive nanopillars and the Spin-orbit torque devices.

The wide band-gap of the material and the well-known electrical properties of the pure semiconductor could have an interesting application in optoelectronic science and technology. A possible spin-valve at room temperature could be the best simple spintronic device of *Co* : *ZnO*.

Also, continue as doubt the presence of possible segregated Cobalt phases in the samples,

which should be cleared by other characterization techniques as XPS.

## 6.3. Peer-reviewed articles

Among the production of this work, some articles in peer-reviewed journals were published or are in the peer review process.

### 6.3.1. *ZnO* DFT approach

- (In peer review process) Physica Status Solidi (b) Influence of Oxygen vacancies on Room-temperature ferromagnetism in Cobalt-doped ZnO. E. F. Galindez, Rafael González-Hernández, A. Dussan, and Victor Mendoza

### 6.3.2. Cobalt influence in DMS

- Heliyon (2019) Ferromagnetic-like Behavior of Co doped TiO<sub>2</sub> Flexible Thin Films Fabricated Via co-Sputtering for Spintronic Applications. Heiddy P. Quiroz, E. F. Galindez, A. Dussan. <https://doi.org/10.1016/j.heliyon.2020.e03338>
- J Mater Sci (2020) Super-exchange interaction model in DMOs: Co doped TiO<sub>2</sub> thin films. Heiddy P. Quiroz, E. F. Galindez, J. G. Ramírez A. Dussan. <https://doi.org/10.1007/s10853-020-05282-2>



# A. Appendix: Purity report of ZnO and Co targets

## PLASMATERIALS Certificate of Analysis

Customer Name:	Vortex Company	Material:	Cobalt
Purchase Order No.:	Vortex3912014	Composition:	Co
Lot Number:	PLA 120018326	Size:	3" Dia X 0.125" Thick
Product Description:	Sputtering Target	Purity:	99.9%

### Spectrographic Analysis PPM

Si 60	Fe 70	Zn 14
Pb 3	Ni 15	Cd 6
Mn 34	Ca 4	Mg 6
Cr 40		

Note: Typical Analysis of Starting Material Only

Date of Certification: 06/30/2014

By: \_\_\_\_\_



# PLASMATERIALS

## Certificate of Analysis

<b>Customer Name:</b>	Vortex Company	<b>Material:</b>	Zinc Oxide
<b>Purchase Order No.:</b>	1099	<b>Composition:</b>	ZnO
<b>Lot Number:</b>	PLA490890390	<b>Size:</b>	3" Dia X 0.125" Thick
<b>Product Description:</b>	Sputtering Target	<b>Purity:</b>	99.99%

### Spectrographic Analysis PPM

Mg <5	Al <5	Si <10
Ca <10	Ti <10	V <10
Cr <5	Mn <5	Fe <5
Ni <5	Co <5	Cu <1
As <1	Sn <1	Sb <1
Pb <5	Bi <5	Cd <10

Note: Typical Analysis of Starting Material Only

Date of Certification: 12/30/2015

By: \_\_\_\_\_

2268 Research Drive, Livermore, CA 94550



## B. Appendix: Substrates data-sheet

QUBITeXp International TRade S.A.S., NIT 900338166-0 Bogotá Kr. 8 167D-62 APT 1403  
Tel. +57 3104831915, Fax. +57 (1) 8050754 E-mail: beynor.paez@qubitexp.com



### REMISION

ITO Coated Corning Glass for R&D Use

Indium Tin Oxid (ITO) coated onto corning glass. DepotNano

Low sheet resistance and high transmittance,

Applications: OLED, OPV, electrochromic devices, electrochemistry, Low-Temperature Solution-Processed Perovskite Solar Cells.

#### Parameters:

Substrate: corning

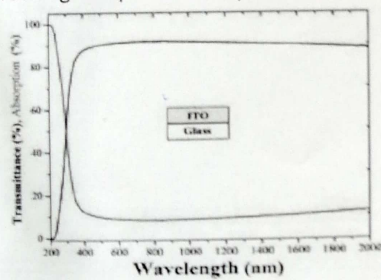
Sheet resistance: <10 ohm/sq

Transparency: >83%

Roughness: < 3 nm

Thickness of conductive layer =  $180.0 \pm 15.0$  Å

Working temperature: up to 300 °C



23/03/2021

Certificate Of Analysis

# Certificate of Analysis

**SIGMA-ALDRICH**

<b>Product Name</b>	Silicon, wafer (single side polished), <100>, N-type, contains phosphorus as dopant, diam. × thickness 3 in. × 0.5 mm
<b>Product Number</b>	647802
<b>Product Brand</b>	ALDRICH
<b>CAS Number</b>	<a href="#">7440-21-3</a>
<b>Molecular Formula</b>	Si
<b>Molecular Weight</b>	28.09

**TEST**

APPEARANCE

VENDOR INFORMATION

QUALITY CONTROL

**SPECIFICATION****LOT 10725KC RESULTS**

GREY DISC

(100) DOPED N-TYPE 3"DIAM

SEPTEMBER 2004



Barbara Rajzer, Supervisor  
Quality Control  
Milwaukee, Wisconsin USA



# C. Appendix: PDF files from XRD analysis

Date: 1/02/2021 Time: 6:54:04 p. m.

File: Al2O3

User: Alejandra

## Name and formula

Reference code: 00-004-0787

Mineral name: Aluminum, syn  
 Compound name: Aluminum  
 PDF index name: Aluminum

Empirical formula: Al  
 Chemical formula: Al

## Crystallographic parameters

Crystal system: Cubic  
 Space group: Fm-3m  
 Space group number: 225

a (Å): 4,0494  
 b (Å): 4,0494  
 c (Å): 4,0494  
 Alpha (°): 90,0000  
 Beta (°): 90,0000  
 Gamma (°): 90,0000

Calculated density (g/cm<sup>3</sup>): 2,70  
 Volume of cell (10<sup>6</sup> pm<sup>3</sup>): 66,40  
 Z: 4,00

RIR: 3,62

## Subfiles and quality

Subfiles: Alloy, metal or intermetallic  
 Common Phase  
 Educational pattern  
 Explosive  
 Forensic  
 Inorganic  
 Mineral  
 NBS pattern  
 Pigment/Dye

Quality: Star (S)

## Comments

Color: Light gray metallic  
 Creation Date: 1/01/1970  
 Modification Date: 1/01/1970  
 Color: Light gray metallic  
 Sample Preparation: The material used for the NBS sample was a melting point standard sample of aluminum prepared at NBS, Gaithersburg, Maryland, USA

Analysis: The chemical analysis (%): Si 0.011, Cu 0.006, Fe 0.007, Ti 0.0001, Zr 0.003, Ga 0.004, Mo 0.00002, S 0.0001, Al 99.9+ (by difference). Temperature of Data Collection: Pattern taken at 25 C. Mineral species of doubtful validity, *Am. Mineral.*, **65** 205 (1980). Additional Patterns: See ICSD 64700 (PDF 85-1327).

Date: 1/02/2021 Time: 6:39:37 p. m.

File: Au

User: Alejandra

**Name and formula**

Reference code: 00-004-0784

Mineral name: Gold, syn  
 Compound name: Gold  
 PDF index name: Gold

Empirical formula: Au  
 Chemical formula: Au

**Crystallographic parameters**

Crystal system: Cubic  
 Space group: Fm-3m  
 Space group number: 225

a (Å): 4,0786  
 b (Å): 4,0786  
 c (Å): 4,0786  
 Alpha (°): 90,0000  
 Beta (°): 90,0000  
 Gamma (°): 90,0000

Calculated density (g/cm<sup>3</sup>): 19,30  
 Measured density (g/cm<sup>3</sup>): 19,30  
 Volume of cell (10<sup>6</sup> pm<sup>3</sup>): 67,85  
 Z: 4,00

RIR: -

**Subfiles and quality**

Subfiles: Alloy, metal or intermetallic  
 Common Phase  
 Educational pattern  
 Forensic  
 Inorganic  
 Mineral  
 NBS pattern

Quality: Star (S)

**Comments**

Color: Yellow metallic  
 Creation Date: 1/01/1970  
 Modification Date: 1/01/1970  
 Color: Yellow metallic  
 Melting Point: 1061.6-1063.2  
 Sample Source or Locality: Sample purified at NBS, Gaithersburg, Maryland, USA and is about 99.997% Au  
 Temperature of Data Collection: Pattern taken at 26 C  
 Analysis: Spectrographic analysis (%): Si 0.001, Ca 0.001, Ag 0.001(?). Opaque mineral optical data on specimen from unspecified locality: RR<sub>2</sub>Re=71.6, Disp.=16, VHN<sub>100</sub>=53-58, Color values=.384, .391, 72.7, Ref.: IMA Commission on Ore Microscopy QDF. Optical Data: B=0.366.



Date: 1/02/2021 Time: 6:35:41 p. m.

File: Si

User: Alejandra

**Name and formula**

Reference code: 00-035-1158

Compound name: Silicon  
PDF index name: Silicon

Empirical formula: Si  
Chemical formula: Si

**Crystallographic parameters**

Crystal system: Cubic  
Space group: Fm3m  
Space group number: 225

a (Å): 3,9030  
b (Å): 3,9030  
c (Å): 3,9030  
Alpha (°): 90,0000  
Beta (°): 90,0000  
Gamma (°): 90,0000

Calculated density (g/cm<sup>3</sup>): 3,13  
Volume of cell (10<sup>6</sup> pm<sup>3</sup>): 59,46  
Z: 4,00

RIR: -

**Subfiles and quality**

Subfiles: Alloy, metal or intermetallic  
Inorganic

Quality: Blank (B)

**Comments**

Creation Date: 1/01/1970  
Modification Date: 1/01/1970  
Structures: N-type Si single-crystal grown by Czochralski method was subject to uniform compression to pressure up to 80 kbar. Pattern at 80 kbar.

**References**

Primary reference: Leonidova, G., *Sov. Phys. Solid State*, **22**, 559, (1980)

**Peak list**

No.	h	k	l	d [Å]	2Theta[deg]	I [%]
1	1	1	1	2,25800	39,893	100,0
2	2	0	0	1,95600	46,384	25,0
3	2	2	0	1,38170	67,766	20,0
4	3	1	1	1,17850	81,631	20,0
5	2	2	2	1,12730	86,206	10,0



Date: 1/02/2021 Time: 6:35:20 p. m.

File: Si

User: Alejandra

**Name and formula**

Reference code: 01-085-0461  
Compound name: Silicon Oxide  
ICSD name: Silicon Oxide  
Empirical formula: O<sub>2</sub>Si  
Chemical formula: SiO<sub>2</sub>

**Crystallographic parameters**

Crystal system: Hexagonal  
Space group: P3221  
Space group number: 154  
a (Å): 4,7040  
b (Å): 4,7040  
c (Å): 5,2610  
Alpha (°): 90,0000  
Beta (°): 90,0000  
Gamma (°): 120,0000  
Calculated density (g/cm<sup>3</sup>): 2,97  
Volume of cell (10<sup>6</sup> pm<sup>3</sup>): 100,82  
Z: 3,00  
RIR: 2,70

**Status, subfiles and quality**

Status: Diffraction data collected at non ambient pressure  
Subfiles: Alloy, metal or intermetallic  
Inorganic  
Modelled additional pattern  
Pharmaceutical  
Quality: Calculated (C)

**Comments**

ICSD collection code: 016335  
Creation Date: 1/01/1970  
Modification Date: 1/01/1970  
ICSD Collection Code: 016335  
ICSD SG: P3221S IT is: 154 SG short form: P3221. Calculated Pattern Original Remarks: REM  
PRE 6000. Test from ICSD: No R value given. Temperature Factor: ITF.

**References**

Primary reference: *Calculated from ICSD using POWD-12++, (1997)*  
Structure: d'Amour, H., Denner, W., Schulz, H., *Acta Crystallogr., Sec. B*, **35**, 550, (1979)

**Peak list**

Date: 1/02/2021 Time: 7:48:58 p. m.

File: 3a-4

User: Alejandra

**Name and formula**

Reference code: 01-080-0074  
Compound name: Zinc Oxide  
ICSD name: Zinc Oxide  
Empirical formula: OZn  
Chemical formula: ZnO

**Crystallographic parameters**

Crystal system: Hexagonal  
Space group: P63mc  
Space group number: 186  
a (Å): 3,2535  
b (Å): 3,2535  
c (Å): 5,2151  
Alpha (°): 90,0000  
Beta (°): 90,0000  
Gamma (°): 120,0000  
Calculated density (g/cm<sup>3</sup>): 5,65  
Volume of cell (10<sup>6</sup> pm<sup>3</sup>): 47,81  
Z: 2,00  
RIR: 5,44

**Subfiles and quality**

Subfiles: Alloy, metal or intermetallic  
Corrosion  
Inorganic  
Modelled additional pattern  
Pharmaceutical  
Quality: Calculated (C)

**Comments**

ICSD collection code: 067848  
Creation Date: 1/01/1970  
Modification Date: 1/01/1970  
ICSD Collection Code: 067848  
Calculated Pattern Original Remarks: REM RVP  
Calculated Pattern Original Remarks: REM K ZnO obtained from beta-Zn(OH)Cl  
Temperature Factor: ITF.

**References**

Primary reference: *Calculated from ICSD using POWD-12++, (1997)*  
Structure: Garcia-Martinez, O., Rojas, R.M., Vila, E., Martin de Vidales, J.L., *Solid State Ionics*, **63**, 442, (1993)

# Bibliography

- [1] Matthew S. Eastin, Nancy H. Brinson, Alexandra Doorey, and Gary Wilcox. Living in a big data world: Predicting mobile commerce activity through privacy concerns. *Computers in Human Behavior*, 58:214–220, may 2016.
- [2] VCould's News. Every Day Big Data Statistics – 2.5 Quintillion Bytes of Data Created Daily, 2015.
- [3] Johann W Kolar. Future Challenges in Power Electronics. Technical report, Eidgenössische Technische Hochschule Zürich, 2021.
- [4] V. G. Subbotin, A. M. Zubareva, A. A. Voinov, A. N. Zubarev, and L. Schlattauer. New analog electronics for the new challenges in the synthesis of superheavy elements. *Physics of Particles and Nuclei Letters*, 13(5):557–560, sep 2016.
- [5] Philipp R. Struck and Guido Burkard. Spin Quantum Computing. In *Handbook of Spintronics*, pages 71–103. Springer Netherlands, Dordrecht, 2016.
- [6] Hiroaki Yoda. MRAM Fundamentals and Devices. In *Handbook of Spintronics*, pages 1031–1064. Springer Netherlands, Dordrecht, 2016.
- [7] Supriyo Bandyopadhyay and Marc Cahay. General Principles of Spin Transistors and Spin Logic Devices. In *Handbook of Spintronics*, pages 1175–1242. Springer Netherlands, Dordrecht, 2016.
- [8] A. Anane, B. Dlubak, Hiroshi Idzuchi, H. Jaffres, M-B. Martin, Y. Otani, P. Seneor, and Albert Fert. Spin Transport in Carbon Nanotubes and Graphene: Experiments and Theory. In *Handbook of Spintronics*, pages 681–706. Springer Netherlands, Dordrecht, 2016.
- [9] Xiaoguang Zhang and William Butler. Theory of Giant Magnetoresistance and Tunneling Magnetoresistance. In *Handbook of Spintronics*, pages 3–69. Springer Netherlands, Dordrecht, 2016.
- [10] Tanja Graf, Claudia Felser, and Stuart S. P. Parkin. Heusler Compounds: Applications in Spintronics. In *Handbook of Spintronics*, pages 335–364. Springer Netherlands, Dordrecht, 2016.

- 
- [11] R. Brazil. Putting a spin on it: spintronics and super-fast computing. *Engineering & Technology*, 10(10):74–77, nov 2015.
- [12] Seongik Hong, Byoung-Joon (BJ) Lee, Chang-Mo (C.M) Yoo, Mi-Sun Do, and Jang-Woo Son. Comparative Study of Content-Centric vs. Content Delivery Networks. In *The 10th International Conference on Future Internet - CFI '15*, pages 35–40, New York, New York, USA, 2015. ACM Press.
- [13] Shinobu Fujita. MRAM Circuits. In *Handbook of Spintronics*, pages 1101–1125. Springer Netherlands, Dordrecht, 2016.
- [14] Nguyen Hoa Hong. Magnetic Oxide Semiconductors. In *Handbook of Spintronics*, pages 563–583. Springer Netherlands, Dordrecht, 2016.
- [15] Nguyen Hoa Hong. Diluted magnetic Semiconducting oxides. In *Functional Materials and Electronics*, pages 263–287. Apple Academic Press, Oakville, ON ; Waretown, NJ : Apple Academic Press, [2017], may 2018.
- [16] A. Kaminski and S. Das Sarma. Polaron Percolation in Diluted Magnetic Semiconductors. *Physical Review Letters*, 88(24):247202, may 2002.
- [17] Mikhail I. Dyakonov, editor. *Spin Physics in Semiconductors*, volume 157 of *Springer Series in Solid-State Sciences*. Springer International Publishing, Cham, 2017.
- [18] Li-Min Zheng, Jinkui Tang, Hao-Ling Sun, and Min Ren. Low Dimensional Molecular Magnets and Spintronics. In *Handbook of Spintronics*, pages 617–680. Springer Netherlands, Dordrecht, 2016.
- [19] Joël Cibert and Denis Scalbert. Diluted Magnetic Semiconductors: Basic Physics and Optical Properties. In *Spin Physics in Semiconductors*, pages 477–524. Springer, 2017.
- [20] J.M.D Coey. Dilute magnetic oxides. *Current Opinion in Solid State and Materials Science*, 10(2):83–92, apr 2006.
- [21] Tomasz Dietl. A ten-year perspective on dilute magnetic semiconductors and oxides. *Nature Materials*, 9(12):965–974, dec 2010.
- [22] I S I Web of Knowledge. Web of Knowledge, 2018.
- [23] Priya Gopal and Nicola A. Spaldin. Magnetic interactions in transition-metal-doped ZnO: An ab initio study. *Physical Review B - Condensed Matter and Materials Physics*, 74(9):094418, sep 2006.
- [24] Marius Grundmann. Magnetic Semiconductors. In *The Physics of Semiconductors*, pages 505–513. Springer, Cham, 2016.

- [25] T. Dietl, H. Ohno, F. Matsukura, J. Cibert, and D. Ferrand. Zener model description of ferromagnetism in zinc-blende magnetic semiconductors. *Science*, 287(5455):1019–1022, feb 2000.
- [26] H. Saito, V. Zayets, S. Yamagata, and K. Ando. Room-Temperature Ferromagnetism in a II-VI Diluted Magnetic Semiconductor  $Zn_{1-x}Cr_xTe$ . *Physical Review Letters*, 90(20):207202, may 2003.
- [27] Gennadiy A. Medvedkin, Takayuki Ishibashi, Takao Nishi, Koji Hayata, Yoichi Hasegawa, and Katsuaki Sato. Room Temperature Ferromagnetism in Novel Diluted Magnetic Semiconductor  $Cd_{1-x}Mn_xGeP_2$ . *Japanese Journal of Applied Physics*, 39(Part 2, No. 10A):L949–L951, oct 2000.
- [28] B. Poornaprakash, S. Ramu, Si-Hyun Park, R.P. Vijayalakshmi, and B.K. Reddy. Room temperature ferromagnetism in Nd doped ZnS diluted magnetic semiconductor nanoparticles. *Materials Letters*, 164:104–107, feb 2016.
- [29] Wenjian Liu, Hongxia Zhang, Jin-an Shi, Zhongchang Wang, Cheng Song, Xiangrong Wang, Siyuan Lu, Xiangjun Zhou, Lin Gu, Dmitri V. Louzguine-Luzgin, Mingwei Chen, Kefu Yao, and Na Chen. A room-temperature magnetic semiconductor from a ferromagnetic metallic glass. *Nature Communications*, 7(1):13497, dec 2016.
- [30] D. Saikia and J. P. Borah. Investigations of doping induced structural, optical and magnetic properties of Ni doped ZnS diluted magnetic semiconductors. *Journal of Materials Science: Materials in Electronics*, 28(11):8029–8037, jun 2017.
- [31] J. Hays, A. Thurber, K. M. Reddy, A. Punnoose, and M. H. Engelhard. Development and processing temperature dependence of ferromagnetism in  $Zn_{0.98}Co_{0.02}O$ . *Journal of Applied Physics*, 99(8):08M123, apr 2006.
- [32] Aaron P. Thurber, Geoffrey L. Beausoleil II, Gordon A. Alanko, Joshua J. Anghel, Michael S. Jones, Lydia M. Johnson, Jianhui Zhang, C. B. Hanna, D. A. Tenne, and Alex Punnoose. Magnetism of ZnO nanoparticles: Dependence on crystallite size and surfactant coating. *Journal of Applied Physics*, 109(7):07C305, apr 2011.
- [33] Seita Onishi, Miguel M. Ugeda, Yi Zhang, Yi Chen, Claudia Ojeda-Aristizabal, Hyejin Ryu, Sung-Kwan Mo, Zahid Hussain, Zhi-Xun Shen, Michael F. Crommie, and Alex Zettl. Magnetic Field Studies Near Superconducting Transition in MBE Grown Monolayer NbSe<sub>2</sub> on Bilayer Graphene. *APS March Meeting 2016, abstract id. V15.003*, 2016.
- [34] L. J. Collins-McIntyre, L. B. Duffy, A. Singh, N.-J. Steinke, C. J. Kinane, T. R. Charlton, A. Pushp, A. J. Kellock, S. S. P. Parkin, S. N. Holmes, C. H. W. Barnes, G. van der

- Laan, S. Langridge, and T. Hesjedal. Structural, electronic, and magnetic investigation of magnetic ordering in MBE-grown  $\text{Cr}_x\text{Sb}_{2-x}\text{Te}_3$  thin films. *EPL (Europhysics Letters)*, 115(2):27006, jul 2016.
- [35] Minju Ying, Shida Wang, Tao Duan, Bin Liao, Xu Zhang, Zengxia Mei, Xiaolong Du, F.M. Gerriu, A.M. Fox, and G.A. Gehring. The structure, optical and magnetic properties of arsenic implanted ZnO films prepared by molecular beam epitaxy. *Materials Letters*, 171:121–124, may 2016.
- [36] C. (Chennupati) Jagadish and S. J. Pearton. *Zinc oxide bulk, thin films and nanostructures : processing, properties and applications*. Elsevier, 2006.
- [37] R Eason. *Pulsed laser deposition of thin films: applications-led growth of functional materials*. Wiley-Interscience, 2007.
- [38] E H Nicollian and J R Brews. *MOS (Metal Oxide Semiconductor) Physics and Technology*. Wiley, 2002.
- [39] J Watson. The tin oxide gas sensor and its applications. *Sensors and Actuators*, 5(1):29–42, 1984.
- [40] A O Musa, T Akomolafe, and M J Carter. Production of cuprous oxide, a solar cell material, by thermal oxidation and a study of its physical and electrical properties. *Solar Energy Materials and Solar Cells*, 51(3):305–316, 1998.
- [41] Toshiaki Arai, Narihiro Morosawa, Kazuhiko Tokunaga, Yasuhiro Terai, Eri Fukumoto, Takashige Fujimori, Tetsuo Nakayama, Takashi Yamaguchi, and Tatsuya Sasaoka. 69.2: Highly Reliable Oxide-Semiconductor TFT for AM-OLED Display. *SID Symposium Digest of Technical Papers*, 41(1):1033–1036, 2012.
- [42] Andreas Kay and Michael Gretzel. Low cost photovoltaic modules based on dye sensitized nanocrystalline titanium dioxide and carbon powder. *Solar Energy Materials and Solar Cells*, 44(1):99–117, 1996.
- [43] J F Wager and R Hoffman. Thin, fast, and flexible. *IEEE Spectrum*, 48(5):42–56, may 2011.
- [44] E Fortunato, P Barquinha, and R Martins. Oxide Semiconductor Thin-Film Transistors: A Review of Recent Advances. *Advanced Materials*, 24(22):2945–2986, 2012.
- [45] Hideo Hosono and Hiroshi Kawazoe. Approach to novel crystalline and amorphous oxide materials for optoelectronics by ion implantation. *Materials Science and Engineering: B*, 41(1):39–45, 1996.

- [46] P Barquinha, L Pereira, G Gonzalves, R Martins, and E Fortunato. Toward High-Performance Amorphous GIZO TFTs. *Electrochemical Society*, 156(3):H161–H168, 2009.
- [47] Wantae Lim, E A Douglas, S.-H. Kim, D P Norton, S J Pearton, F Ren, H Shen, and W H Chang. Low-temperature-fabricated InGaZnO<sub>4</sub> thin film transistors on polyimide clean-room tape. *Applied Physics Letters*, 93(25):252103, 2008.
- [48] D.C. Look. Recent advances in ZnO materials and devices. *Materials Science and Engineering: B*, 80(1-3):383–387, mar 2001.
- [49] Ü Özgür, Ya. I Alivov, C Liu, A Teke, M A Reshchikov, S Doğan, V Avrutin, S.-J. Cho, and H Morkoç. A comprehensive review of ZnO materials and devices. *Journal of Applied Physics*, 98(4):41301, 2005.
- [50] Satishchan Ogale. *Thin Films and Heterostructures for Oxide Electronics*. Multifunctional Thin Film Series. Springer-Verlag, New York, 2005.
- [51] Norbert H. Nickel and Evgenii Terukov, editors. *Zinc Oxide — A Material for Micro- and Optoelectronic Applications*, volume 194 of *NATO Science Series II: Mathematics, Physics and Chemistry*. Springer Netherlands, Dordrecht, 2005.
- [52] D.G. Thomas. The exciton spectrum of zinc oxide. *Journal of Physics and Chemistry of Solids*, 15(1-2):86–96, aug 1960.
- [53] A. Mang, K. Reimann, and St. Rübenacke. Band gaps, crystal-field splitting, spin-orbit coupling, and exciton binding energies in ZnO under hydrostatic pressure. *Solid State Communications*, 94(4):251–254, apr 1995.
- [54] D.C. Reynolds, D.C. Look, and B. Jogai. Optically pumped ultraviolet lasing from ZnO. *Solid State Communications*, 99(12):873–875, sep 1996.
- [55] Yefan Chen, D. M. Bagnall, Hang-jun Koh, Ki-tae Park, Kenji Hiraga, Ziqiang Zhu, and Takafumi Yao. Plasma assisted molecular beam epitaxy of ZnO on *ici*-plane sapphire: Growth and characterization. *Journal of Applied Physics*, 84(7):3912–3918, oct 1998.
- [56] V. Srikant and D. R. Clarke. On the optical band gap of zinc oxide. *Journal of Applied Physics*, 83(10):5447–5451, may 1998.
- [57] D. M. Bagnall, Y. F. Chen, Z. Zhu, T. Yao, S. Koyama, M. Y. Shen, and T. Goto. Optically pumped lasing of ZnO at room temperature. *Applied Physics Letters*, 70(17):2230–2232, apr 1997.

- [58] New Jersey Zinc Company and H E Brown. *Zinc Oxide Rediscovered*. New Jersey Zinc Company, 1957.
- [59] Chris G. Van de Walle. Hydrogen as a Cause of Doping in Zinc Oxide. *Physical Review Letters*, 85(5):1012–1015, jul 2000.
- [60] A. F. Kohan, G. Ceder, D. Morgan, and Chris G. Van de Walle. First-principles study of native point defects in ZnO. *Physical Review B*, 61(22):15019–15027, jun 2000.
- [61] Chris G. Van de Walle. Defect analysis and engineering in ZnO. *Physica B: Condensed Matter*, 308-310:899–903, dec 2001.
- [62] S. B. Zhang, S.-H. Wei, and Alex Zunger. Intrinsic  $n$ -type versus  $p$ -type doping asymmetry and the defect physics of ZnO. *Physical Review B*, 63(7):075205, jan 2001.
- [63] Fumiyasu Oba, Shigeto R. Nishitani, Seiji Isotani, Hirohiko Adachi, and Isao Tanaka. Energetics of native defects in ZnO. *Journal of Applied Physics*, 90(2):824–828, jul 2001.
- [64] Anderson Janotti and Chris G. Van de Walle. Oxygen vacancies in ZnO. *Applied Physics Letters*, 87(12):122102, sep 2005.
- [65] Paul Erhart and Karsten Albe. First-principles study of migration mechanisms and diffusion of oxygen in zinc oxide. *Physical Review B*, 73(11):115207, mar 2006.
- [66] T. C. Kaspar, T. Droubay, S. M. Heald, P. Nachimuthu, C. M. Wang, V. Shutthanandan, C. A. Johnson, D. R. Gamelin, and S. A. Chambers. Lack of ferromagnetism in  $n$ -type cobalt-doped ZnO epitaxial thin films. *New Journal of Physics*, 10(18pp):55010, may 2008.
- [67] D. Anbuselvan, S. Nilavazhagan, A. Santhanam, N. Chidhambaram, K.V. Gunavathy, Tansir Ahamad, and Saad M. Alshehri. Room temperature ferromagnetic behavior of nickel-doped zinc oxide dilute magnetic semiconductor for spintronics applications. *Physica E: Low-dimensional Systems and Nanostructures*, 129:114665, 2021.
- [68] Y. Ohno, I. Arata, F. Matsukura, K. Ohtani, S. Wang, and H. Ohno. MBE growth and electroluminescence of ferromagnetic/non-magnetic semiconductor pn junctions based on (Ga,Mn)As. *Applied Surface Science*, 159-160:308–312, jun 2000.
- [69] H. Munekata, H. Ohno, S. von Molnar, Alex Harwit, Armin Segmüller, and L. L. Chang. Epitaxy of III–V diluted magnetic semiconductor materials. *Journal of Vacuum Science & Technology B: Microelectronics and Nanometer Structures*, 8(2):176, mar 1990.



- [70] H. Munekata, A. Zaslavsky, P. Fumagalli, and R. J. Gambino. Preparation of (In,Mn)As/(Ga,Al)Sb magnetic semiconductor heterostructures and their ferromagnetic characteristics. *Applied Physics Letters*, 63(21):2929–2931, nov 1993.
- [71] Matthias Bock, Pascal Eich, Stephan Kucera, Matthias Kreis, and et.al. High-fidelity entanglement between a trapped ion and a telecom photon via quantum frequency conversion. *Nature Communications*, 9(1):1998, dec 2018.
- [72] J M D Coey, Kwanruthai Wongsaprom, J Alaria, and M Venkatesan. Charge-transfer ferromagnetism in oxide nanoparticles. *Journal of Physics D: Applied Physics*, 41(13):134012, jul 2008.
- [73] J M D Coey, P Stamenov, R D Gunning, M Venkatesan, and K Paul. Ferromagnetism in defect-ridden oxides and related materials. *New Journal of Physics*, 12(5):053025, may 2010.
- [74] J. Philip, A. Punnoose, B. I. Kim, K. M. Reddy, S. Layne, J. O. Holmes, B. Satpati, P. R. LeClair, T. S. Santos, and J. S. Moodera. Carrier-controlled ferromagnetism in transparent oxide semiconductors. *Nature Materials*, 5(4):298–304, apr 2006.
- [75] Boris Straumal, Andrei Mazilkin, Svetlana Protasova, Ata Myatiev, Petr Straumal, Eberhard Goering, and Brigitte Baretzky. Influence of texture on the ferromagnetic properties of nanograined ZnO films. *physica status solidi (b)*, 248(7):1581–1586, jul 2011.
- [76] Daqiang Gao, Jing Zhang, Jingyi Zhu, Jing Qi, Zhaohui Zhang, Wenbo Sui, Huigang Shi, and Desheng Xue. Vacancy-Mediated Magnetism in Pure Copper Oxide Nanoparticles. *Nanoscale Research Letters*, 5(4):769–772, apr 2010.
- [77] Xu Zuo, Soack-Dae Yoon, Aria Yang, and et.al. Ferromagnetism in pure wurtzite zinc oxide. *Journal of Applied Physics*, 105(7):07C508, apr 2009.
- [78] J F Liu, En-Zuo Liu, H Wang, N H Su, J Qi, and J Z Jiang. Surface magnetism in amine-capped ZnO nanoparticles. *Nanotechnology*, 20(16):165702, apr 2009.
- [79] K. Sato, L. Bergqvist, J. Kudrnovský, P. H. Dederichs, O. Eriksson, I. Turek, B. Sanyal, G. Bouzerar, H. Katayama-Yoshida, V. A. Dinh, T. Fukushima, H. Kizaki, and R. Zeller. First-principles theory of dilute magnetic semiconductors. *Reviews of Modern Physics*, 82(2):1633–1690, may 2010.
- [80] M. Bououdina, N. Mamouni, O.M. Lemine, A. Al-Saie, A. Jaafar, B. Ouladdiaf, A. El Kenz, A. Benyoussef, and E.K. Hlil. Neutron diffraction study and ab-initio calculations of nanostructured doped ZnO. *Journal of Alloys and Compounds*, 536:66–72, sep 2012.

- [81] T. Fukumura, Zhengwu Jin, A. Ohtomo, H. Koinuma, and M. Kawasaki. An oxide-diluted magnetic semiconductor: Mn-doped ZnO. *Applied Physics Letters*, 75(21):3366–3368, nov 1999.
- [82] T. Fukumura, Zhengwu Jin, M. Kawasaki, T. Shono, T. Hasegawa, S. Koshihara, and H. Koinuma. Magnetic properties of Mn-doped ZnO. *Applied Physics Letters*, 78(7):958–960, feb 2001.
- [83] Zhengwu Jin, T. Fukumura, M. Kawasaki, K. Ando, H. Saito, T. Sekiguchi, Y. Z. Yoo, M. Murakami, Y. Matsumoto, T. Hasegawa, and H. Koinuma. High throughput fabrication of transition-metal-doped epitaxial ZnO thin films: A series of oxide-diluted magnetic semiconductors and their properties. *Applied Physics Letters*, 78(24):3824–3826, jun 2001.
- [84] Jae Hyun Kim, Hyojin Kim, Dojin Kim, Young Eon Ihm, and Woong Kil Choo. Magnetic properties of epitaxially grown semiconducting Zn<sub>1-x</sub>Co<sub>x</sub>O thin films by pulsed laser deposition. *Journal of Applied Physics*, 92(10):6066–6071, nov 2002.
- [85] A. Tiwari, C. Jin, A. Kvit, D. Kumar, J. F. Muth, and J. Narayan. Structural, optical and magnetic properties of diluted magnetic semiconducting Zn<sub>1-x</sub>Mn<sub>x</sub>O films. *Solid State Communications*, 121(6-7):371–374, feb 2002.
- [86] Kenji Ueda, Hitoshi Tabata, and Tomoji Kawai. Magnetic and electric properties of transition-metal-doped ZnO films. *Applied Physics Letters*, 79(7):988–990, aug 2001.
- [87] T. Wakano, N. Fujimura, Y. Morinaga, N. Abe, A. Ashida, and T. Ito. Magnetic and magneto-transport properties of ZnO: Ni films. *Physica E: Low-Dimensional Systems and Nanostructures*, 10(1-3):260–264, may 2001.
- [88] Hiromasa Saeki, Hitoshi Tabata, and Tomoji Kawai. Magnetic and electric properties of vanadium doped ZnO films. *Solid State Communications*, 120(11):439–443, nov 2001.
- [89] Young Mok Cho, Woong Kil Choo, Hyojin Kim, Dojin Kim, and Youngeon Ihm. Effects of rapid thermal annealing on the ferromagnetic properties of sputtered Zn<sub>1-x</sub>(Co<sub>0.5</sub>Fe<sub>0.5</sub>)<sub>x</sub>O thin films. *Applied Physics Letters*, 80(18):3358–3360, may 2002.
- [90] Hyeon Jun Lee, Se Young Jeong, Chae Ryong Cho, and Chul Hong Park. Study of diluted magnetic semiconductor: Co-doped ZnO. *Applied Physics Letters*, 81(21):4020–4022, nov 2002.
- [91] S. W. Jung, S. J. An, Gyu Chul Yi, C. U. Jung, Sung Ik Lee, and Sunglae Cho. Ferromagnetic properties of Zn<sub>1-x</sub>Mn<sub>x</sub>O epitaxial thin films. *Applied Physics Letters*, 80(24):4561–4563, jun 2002.

- [92] S. J. Han, J. W. Song, C. H. Yang, S. H. Park, J. H. Park, Y. H. Jeong, and K. W. Rhie. A key to room-temperature ferromagnetism in Fe-doped ZnO: Cu. *Applied Physics Letters*, 81(22):4212–4214, nov 2002.
- [93] S. G. Yang, A. B. Pakhomov, S. T. Hung, and C. Y. Wong. Room-temperature magnetism in Cr-doped AlN semiconductor films. *Applied Physics Letters*, 81(13):2418–2420, sep 2002.
- [94] D. P. Norton, S. J. Pearton, A. F. Hebard, N. Theodoropoulou, L. A. Boatner, and R. G. Wilson. Ferromagnetism in Mn-implanted ZnO:Sn single crystals. *Applied Physics Letters*, 82(2):239–241, jan 2003.
- [95] S. A. Chambers, S. Thevuthasan, R. F.C. Farrow, R. F. Marks, J. U. Thiele, L. Folks, M. G. Samant, A. J. Kellock, N. Ruzycki, D. L. Ederer, and U. Diebold. Epitaxial growth and properties of ferromagnetic co-doped TiO<sub>2</sub> anatase. *Applied Physics Letters*, 79(21):3467–3469, nov 2001.
- [96] D. P. Norton, M. E. Overberg, S. J. Pearton, K. Pruessner, J. D. Budai, L. A. Boatner, M. F. Chisholm, J. S. Lee, Z. G. Khim, Y. D. Park, and R. G. Wilson. Ferromagnetism in cobalt-implanted ZnO. *Applied Physics Letters*, 83(26):5488–5490, dec 2003.
- [97] K. Rode, A. Anane, R. Mattana, J. P. Contour, O. Durand, and R. LeBourgeois. Magnetic semiconductors based on cobalt substituted ZnO. In *Journal of Applied Physics*, volume 93, pages 7676–7678. American Institute of PhysicsAIP, may 2003.
- [98] M. Ivill, S. J. Pearton, S. Rawal, L. Leu, P. Sadik, R. Das, A. F. Hebard, M. Chisholm, J. D. Budai, and D. P. Norton. Structure and magnetism of cobalt-doped ZnO thin films. *New Journal of Physics*, 10(21pp):65002, jun 2008.
- [99] A. C. Tuan, J. D. Bryan, A. B. Pakhomov, V. Shutthanandan, S. Thevuthasan, D. E. McCready, D. Gaspar, M. H. Engelhard, J. W. Rogers, K. Krishnan, D. R. Gamelin, and S. A. Chambers. Epitaxial growth and properties of cobalt-doped ZnO on  $\alpha$ -Al<sub>2</sub>O<sub>3</sub> single-crystal substrates. *Physical Review B - Condensed Matter and Materials Physics*, 70(5):054424, aug 2004.
- [100] Guang Chen, Cheng Song, Chao Chen, Shuang Gao, Fei Zeng, and Feng Pan. Resistive switching and magnetic modulation in cobalt-doped ZnO. *Advanced Materials*, 24(26):3515–3520, jul 2012.
- [101] C. B. Fitzgerald, M. Venkatesan, J. G. Lunney, L. S. Dorneles, and J. M.D. Coey. Cobalt-doped ZnO - A room temperature dilute magnetic semiconductor. *Applied Surface Science*, 247(1-4):493–496, jul 2005.

- [102] Said Benramache and Boubaker Benhaoua. Influence of substrate temperature and Cobalt concentration on structural and optical properties of ZnO thin films prepared by Ultrasonic spray technique. *Superlattices and Microstructures*, 52(4):807–815, oct 2012.
- [103] Sesha Vempati, Amitha Shetty, P. Dawson, K. K. Nanda, and S. B. Krupanidhi. Solution-based synthesis of cobalt-doped ZnO thin films. *Thin Solid Films*, 524:137–143, dec 2012.
- [104] Arockia Jayalatha Kulandaisamy, Chitra Karthek, Prabakaran Shankar, Ganesh Kumar Mani, and John Bosco Balaguru Rayappan. Tuning selectivity through cobalt doping in spray pyrolysis deposited ZnO thin films. *Ceramics International*, 42(1):1408–1415, jan 2016.
- [105] Dhruvashi and P. K. Shishodia. Effect of cobalt doping on ZnO thin films deposited by sol-gel method. *Thin Solid Films*, 612:55–60, aug 2016.
- [106] Zheng Wu Jin, T. Fukumura, K. Hasegawa, Y. Z. Yoo, K. Ando, T. Sekiguchi, P. Ahmet, T. Chikyow, T. Hasegawa, H. Koinuma, and M. Kawasaki. Optical and electrical properties of Co-doped epitaxial ZnO films. *Journal of Crystal Growth*, 237-239(1-4):548–552, apr 2002.
- [107] Jaydeep Sarkar. Chapter 2 - Sputtering and Thin Film Deposition. In Jaydeep Sarkar, editor, *Sputtering Materials for VLSI and Thin Film Devices*, pages 93–170. William Andrew Publishing, Boston, 2014.
- [108] Ronald A Powell and Stephen M Rossnagel. Chapter 2 Physics of sputtering. In *PVD for Microelectronics*, volume 26 of *Thin Films*, pages 23–49. Elsevier, 1999.
- [109] Hideaki Adachi, Tomonobu Hata, and Kiyotaka Wasa. 5 - Basic Process of Sputtering Deposition. In Kiyotaka Wasa, Isaku Kanno, and Hidetoshi Kotera, editors, *Handbook of Sputtering Technology (Second Edition)*, pages 295–359. William Andrew Publishing, Oxford, second edi edition, 2012.
- [110] Institute of Materials and Machine Mechanics. Coating techniques, 2016.
- [111] Petr Vasina. *Plasma diagnostics focused on new magnetron sputtering devices for thin film deposition*. Universite Paris-Sud XI , Masaryk University in Brno, 20085. pag. 11-30.
- [112] R. Erik Holmlin, Rainer Haag, Michael L. Chabinye, Rustem F. Ismagilov, Adam E. Cohen, Andreas Terfort, Maria Anita Rampi, and George M. Whitesides. Electron transport through thin organic films in metal-insulator-metal junctions based on self-assembled monolayers. *Journal of the American Chemical Society*, 123(21):5075–5085, 2001. PMID: 11457338.

- [113] H. Pagnia and N. Sotnik. Bistable switching in electroformed metal–insulator–metal devices. *physica status solidi (a)*, 108(1):11–65, 2015.
- [114] S. Grover, O. Dmitriyeva, M. J. Estes, and G. Moddel. Traveling-wave metal/insulator/metal diodes for improved infrared bandwidth and efficiency of antenna-coupled rectifiers. *IEEE Transactions on Nanotechnology*, 9(6):716–722, Nov 2010.
- [115] Argon (Ar) - Chemical properties, Health and Environmental effects.
- [116] SEMICORE Equipment, Inc. and Matt Hughes. News & articles: What is RF sputtering?, Oct 27, 2016. <http://www.semicore.com/news/92-what-is-rf-sputtering>[Online; accedido el 27-Agosto-2018].
- [117] Alconox® detergent Bulk Packed — Sigma-Aldrich.
- [118] Kurt J. Lesker Company. Kurt j. lesker company — zinc oxide zno sputtering targets — vacuum science is our business.
- [119] J. Zussman. (R. W. G.) Wyckoff. Crystal Structures. 2nd edition, vol. 4. Miscellaneous Inorganic Compounds, Silicates, and Basic Structural Information. Chichester and New York (Wiley: Interscience), 1968. 566 pp. Price 235s. *Mineralogical Magazine*, 37(288):532–534, dec 1969.
- [120] W Prellier, A Fouchet, and B Mercey. Oxide-diluted magnetic semiconductors: A review of the experimental status. *Journal of Physics Condensed Matter*, 15(37):R1583–R1601, sep 2003.
- [121] Rana Mukherji and Vishal Mathur. Review on available theoretical models for room temperature ferromagnetism in dilute magnetic semiconductors. *Journal of Nano- and Electronic Physics*, 11(3), 2019.
- [122] S. A. Wolf, D. D. Awschalom, R. A. Buhrman, J. M. Daughton, S. Von Molnár, M. L. Roukes, A. Y. Chtchelkanova, and D. M. Treger. Spintronics: A spin-based electronics vision for the future, nov 2001.
- [123] Kanwal Preet Bhatti, Vivek Kumar Malik, and Sujeet Chaudhary. Cobalt substituted ZnO thin films: A potential candidate for spintronics. In *Journal of Materials Science: Materials in Electronics*, volume 19, pages 849–854, sep 2008.
- [124] Gugu H. Mhlongo, Katekani Shingange, Zamaswazi P. Tshabalala, Baban P. Dhonge, Fawzy A. Mahmoud, Bonex W. Mwakikunga, and David E. Motaung. Room temperature ferromagnetism and gas sensing in ZnO nanostructures: Influence of intrinsic defects and Mn, Co, Cu doping. *Applied Surface Science*, 390:804–815, dec 2016.

- [125] Kevin R. Kittilstved, Dana A. Schwartz, Allan C. Tuan, Steve M. Heald, Scott A. Chambers, and Daniel R. Gamelin. Direct kinetic correlation of carriers and ferromagnetism in  $\text{Co}^{2+}:\text{ZnO}$ . *Physical Review Letters*, 97(3):037203, jul 2006.
- [126] Aron Walsh, Juarez L F Da Silva, and Su-Huai Wei. Theoretical description of carrier mediated magnetism in cobalt doped ZnO. *Physical review letters*, 100(25):256401, jun 2008.
- [127] G. Lawes, A. S. Risbud, A. P. Ramirez, and Ram Seshadri. Absence of ferromagnetism in Co and Mn substituted polycrystalline ZnO. *Physical Review B - Condensed Matter and Materials Physics*, 71(4):045201, jan 2005.
- [128] C. N.R. Rao and F. L. Deepak. Absence of ferromagnetism in Mn- and Co-doped ZnO. *Journal of Materials Chemistry*, 15(5):573–578, feb 2005.
- [129] Parmanand Sharma, Amita Gupta, K. V. Rao, Frank J. Owens, Renu Sharma, Rajeev Ahuja, J. M. Osorio Guillen, Börje Johansson, and G. A. Gehring. Ferromagnetism above room temperature in bulk and transparent thin films of Mn-doped ZnO. *Nature Materials*, 2(10):673–677, oct 2003.
- [130] Jung H. Park, Min G. Kim, Hyun M. Jang, Sangwoo Ryu, and Young M. Kim. Co-metal clustering as the origin of ferromagnetism in Co-doped ZnO thin films. *Applied Physics Letters*, 84(8):1338–1340, feb 2004.
- [131] Darshan C. Kundaliya, S. B. Ogale, S. E. Lofland, S. Dhar, C. J. Metting, S. R. Shinde, Z. Ma, B. Varughese, K. V. Ramanujachary, L. Salamanca-Riba, and T. Venkatesan. On the origin of high-temperature ferromagnetism in the low-temperature-processed Mn-Zn-O system. *Nature Materials*, 3(10):709–714, sep 2004.
- [132] Herbeet A. Weakliem. Optical spectra of  $\text{Ni}^{2+}$ ,  $\text{Co}^{2+}$ , and  $\text{Cu}^{2+}$  in tetrahedral sites in crystals. *The Journal of Chemical Physics*, 36(8):2117–2140, apr 1962.
- [133] A. Barla, G. Schmerber, E. Beaurepaire, A. Dinia, H. Bieber, S. Colis, F. Scheurer, J. P. Kappler, P. Imperia, F. Nolting, F. Wilhelm, A. Rogalev, D. Müller, and J. J. Grob. Paramagnetism of the Co sublattice in ferromagnetic  $\text{Zn}_{1-x}\text{Co}_x\text{O}$  films. *Physical Review B - Condensed Matter and Materials Physics*, 76(12):125201, sep 2007.
- [134] A. J. Behan, A. Mokhtari, H. J. Blythe, D. Score, X. H. Xu, J. R. Neal, A. M. Fox, and G. A. Gehring. Two magnetic regimes in doped ZnO corresponding to a dilute magnetic semiconductor and a dilute magnetic insulator. *Physical Review Letters*, 100(4):047206, jan 2008.
- [135] Er Jun Kan, Lan Feng Yuan, and Jinlong Yang. Electron-induced ferromagnetic ordering of Co-doped ZnO. *Journal of Applied Physics*, 102(3):033915, aug 2007.

- [136] C. H. Patterson. Role of defects in ferromagnetism in  $\text{Zn}_{1-x}\text{Co}_x\text{O}$ : A hybrid density-functional study. *Physical Review B - Condensed Matter and Materials Physics*, 74(14):144432, oct 2006.
- [137] Keshab Bashyal, Christopher K. Pyles, Sajjad Afroosheh, Aneer Lamichhane, and Alexey T. Zayak. Empirical optimization of DFT + U and HSE for the band structure of ZnO. *Journal of Physics Condensed Matter*, 30(6):065501, jan 2018.
- [138] Stephan Lany and Alex Zunger. Assessment of correction methods for the band-gap problem and for finite-size effects in supercell defect calculations: Case studies for zno and gaas. *Phys. Rev. B*, 78:235104, Dec 2008.
- [139] Paul Erhart, Karsten Albe, and Andreas Klein. First-principles study of intrinsic point defects in zno: Role of band structure, volume relaxation, and finite-size effects. *Phys. Rev. B*, 73:205203, May 2006.
- [140] Matteo Gerosa. Special issue on self-interaction corrected functionals for solids and surfaces, may 2018.
- [141] S. J. Clark, J. Robertson, S. Lany, and A. Zunger. Intrinsic defects in ZnO calculated by screened exchange and hybrid density functionals. *Physical Review B - Condensed Matter and Materials Physics*, 81(11):115311, mar 2010.
- [142] Matteo Gerosa, Carlo Enrico Bottani, Lucia Caramella, Giovanni Onida, Cristiana Di Valentin, and Gianfranco Pacchioni. Electronic structure and phase stability of oxide semiconductors: Performance of dielectric-dependent hybrid functional DFT, benchmarked against GW band structure calculations and experiments. *Physical Review B - Condensed Matter and Materials Physics*, 91(15):155201, apr 2015.
- [143] M. Gerosa, C. E. Bottani, C. Di Valentin, G. Onida, and G. Pacchioni. Accuracy of dielectric-dependent hybrid functionals in the prediction of optoelectronic properties of metal oxide semiconductors: A comprehensive comparison with many-body GW and experiments. *Journal of Physics Condensed Matter*, 30(4):44003, jan 2018.
- [144] M. K. Yaakob, N. H. Hussin, M. F.M. Taib, T. I.T. Kudin, O. H. Hassan, A. M.M. Ali, and M. Z.A. Yahya. First principles LDA+U calculations for ZnO materials. In *Integrated Ferroelectrics*, volume 155, pages 15–22. Taylor and Francis Inc., jul 2014.
- [145] H. Karzel, W. Potzel, M. Köfferlein, W. Schiessl, M. Steiner, U. Hiller, G. Kalvius, D. Mitchell, and T. Das. Lattice dynamics and hyperfine interactions in ZnO and ZnSe at high external pressures. *Physical Review B - Condensed Matter and Materials Physics*, 53(17):11425–11438, may 1996.

- [146] Liang Wu, Tingjun Hou, Yi Wang, Yanfei Zhao, Zhenyu Guo, Youyong Li, and Shuitong Lee. First-principles study of doping effect on the phase transition of zinc oxide with transition metal doped. *Journal of Alloys and Compounds*, 541:250–255, nov 2012.
- [147] S. Saib and N. Bouarissa. Structural parameters and transition pressures of ZnO: ab-initio calculations. *physica status solidi (b)*, 244(3):1063–1069, mar 2007.
- [148] Salah Eddine Boulfefel and Stefano Leoni. Competing intermediates in the pressure-induced wurtzite to rocksalt phase transition in ZnO. *Physical Review B - Condensed Matter and Materials Physics*, 78(12):125204, sep 2008.
- [149] John E. Jaffe, James A. Snyder, Zijing Lin, and Anthony C. Hess. LDA and GGA calculations for high-pressure phase transitions in ZnO and MgO. *Physical Review B - Condensed Matter and Materials Physics*, 62(3):1660–1665, jul 2000.
- [150] D. Maouche, F. Saad Saoud, and L. Louail. Dependence of structural properties of ZnO on high pressure. *Materials Chemistry and Physics*, 106(1):11–15, nov 2007.
- [151] M D Segall, Philip J D Lindan, M J Probert, C J Pickard, P J Hasnip, S J Clark, and M C Payne. First-principles simulation: ideas, illustrations and the CASTEP code. *Journal of Physics: Condensed Matter*, 14(11):2717–2744, mar 2002.
- [152] Philip J. Hasnip, Keith Refson, Matt I. J. Probert, Jonathan R. Yates, Stewart J. Clark, and Chris J. Pickard. Density functional theory in the solid state. *Philosophical Transactions of the Royal Society A: Mathematical, Physical and Engineering Sciences*, 372(2011):20130270, mar 2014.
- [153] Zheng Chuan Wang and Bo Zang Li. Geometric phase in relativistic quantum theory. *Physical Review A - Atomic, Molecular, and Optical Physics*, 60(6):4313–4317, dec 1999.
- [154] Michael Stone. Born-Oppenheimer approximation and the origin of Wess-Zumino terms: Some quantum-mechanical examples. *Physical Review D*, 33(4):1191–1194, feb 1986.
- [155] P. Hohenberg and W. Kohn. Inhomogeneous electron gas. *Physical Review*, 136(3B):B864, nov 1964.
- [156] W. Kohn and L. J. Sham. Self-consistent equations including exchange and correlation effects. *Physical Review*, 140(4A):A1133, nov 1965.
- [157] Fumiyasu Oba, Minseok Choi, Atsushi Togo, and Isao Tanaka. Point defects in ZnO: An approach from first principles, jun 2011.



- [158] G. C. Zhou, L. Z. Sun, X. L. Zhong, Xiaoshuang Chen, Lu Wei, and J. B. Wang. First-principle study on bonding mechanism of ZnO by LDA + U method. *Physics Letters, Section A: General, Atomic and Solid State Physics*, 368(1-2):112–116, aug 2007.
- [159] Jun Wu, Ji Hu, Lihuan Shao, Junming Xu, Kaixin Song, and Peng Zheng. First-principle investigation of K-N dual-acceptor codoping for p-ZnO. *Materials Science in Semiconductor Processing*, 29:245–249, jan 2015.
- [160] J. P. Perdew and Alex Zunger. Self-interaction correction to density-functional approximations for many-electron systems. *Physical Review B*, 23(10):5048–5079, may 1981.
- [161] Xinguo Ma, Ying Wu, Yanhui Lv, and Yongfa Zhu. Correlation effects on lattice relaxation and electronic structure of zno within the GGA+ U formalism. *Journal of Physical Chemistry C*, 117(49):26029–26039, dec 2013.
- [162] Chuanhui Xia, Feng Wang, and Chunlian Hu. Theoretical and experimental studies on electronic structure and optical properties of Cu-doped ZnO. *Journal of Alloys and Compounds*, 589:604–608, mar 2014.
- [163] John P. Perdew, Kieron Burke, and Matthias Ernzerhof. Generalized gradient approximation made simple. *Phys. Rev. Lett.*, 77:3865–3868, Oct 1996.
- [164] John P Perdew, P Ziesche, and H Eschrig. Electronic structure of solids' 91, 1991.
- [165] G. Kresse and J. Furthmüller. Efficient iterative schemes for ab initio total-energy calculations using a plane-wave basis set. *Phys. Rev. B*, 54:11169–11186, Oct 1996.
- [166] G. Kresse and J. Furthmüller. Efficiency of ab-initio total energy calculations for metals and semiconductors using a plane-wave basis set. *Computational Materials Science*, 6(1):15 – 50, 1996.
- [167] G. Kresse and D. Joubert. From ultrasoft pseudopotentials to the projector augmented-wave method. *Phys. Rev. B*, 59:1758–1775, Jan 1999.
- [168] John E. Northrup and S. B. Zhang. Dopant and defect energetics: Si in gaas. *Phys. Rev. B*, 47:6791–6794, Mar 1993.
- [169] X. M. Duan, C. Stampfl, M. M.M. Bilek, and D. R. McKenzie. Codoping of aluminum and gallium with nitrogen in ZnO: A comparative first-principles investigation. *Physical Review B - Condensed Matter and Materials Physics*, 79(23):235208, jun 2009.

- [170] Victor Mendoza-Estrada, William López-Pérez, Rafael González-Hernández, and Alvaro González-García. Electronic structure and magnetic order in Cu x Zn (1-x) O: A study GGA and GGA U. *Physica B: Condensed Matter*, 557:74–81, mar 2019.
- [171] Hadis Morkoç and Ümit Özgür. Zinc Oxide: Fundamentals, Materials and Device Technology. Hadis Morkoç and Ümit Özgr. *Structure*, 2009.
- [172] Weast Robert C. *CRC Handbook of Chemistry and Physics*. Press, Boca Raton, 58th edition, 1997.
- [173] Maryia Baranova, Alexander Danilyuk, and Viktor Stempitsky. Direct exchange interaction of cobalt chains in zinc oxide: Model approach. In *Materials Physics and Mechanics*, volume 39, pages 15–20. Institute of Problems of Mechanical Engineering, 2018.
- [174] Wolfgang Nolting, Anupuru Ramakanth, Wolfgang Nolting, and Anupuru Ramakanth. Heisenberg Model. In *Quantum Theory of Magnetism*, pages 273–386. Springer Berlin Heidelberg, 2009.
- [175] A González-García, V Mendoza-Estrada, W López-Pérez, C Pinilla-Castellanos, and R González-Hernández. Ab-initio study on electronic and magnetic properties of (ga,co) co-doped ZnO. *Journal of Physics: Conference Series*, 743:012002, aug 2016.
- [176] D. E. Heim, Jr Tsang, V. S. Speriosu, B. A. Gurney, M. L. Williams, and R. E. Fontana. Design and Operation of Spin Valve Sensors. *IEEE Transactions on Magnetics*, 30(2):316–321, 1994.
- [177] R. Q. Zhang, J. Su, J. W. Cai, G. Y. Shi, F. Li, L. Y. Liao, F. Pan, and C. Song. Spin valve effect induced by spin-orbit torque switching. *Applied Physics Letters*, 114(9):092404, mar 2019.
- [178] Husam S. Al-Salman and M. J. Abdullah. Effect of Co-doping on the structure and optical properties of ZnO nanostructure prepared by RF-magnetron sputtering. *Superlattices and Microstructures*, 60:349–357, aug 2013.
- [179] K. Kobayashi, T. Maeda, S. Matsushima, and G. Okada. Optical and electronic properties of cobalt-doped zinc oxide films prepared by the sputtering method. *Journal of Materials Science*, 27(21):5953–5957, nov 1992.
- [180] Asim Jilani, M. Sh Abdel-wahab, H. Y. Zahran, I. S. Yahia, Attieh A. Al-Ghamdi, Ahmed Alshahrie, and A. M. El-Naggar. Chemical state analysis, optical band gap, and photocatalytic decolorization of cobalt-doped ZnO nanospherical thin films by DC/RF sputtering technique. *Optik*, 164:143–154, jul 2018.

- [181] Srinivasan Anandan, Naoki Ohashi, and Masahiro Miyauchi. ZnO-based visible-light photocatalyst: Band-gap engineering and multi-electron reduction by co-catalyst. *Applied Catalysis B: Environmental*, 100(3-4):502–509, oct 2010.
- [182] M. A. Hasnat, M. M. Uddin, A. J.F. Samed, S. S. Alam, and S. Hossain. Adsorption and photocatalytic decolorization of a synthetic dye erythrosine on anatase TiO<sub>2</sub> and ZnO surfaces. *Journal of Hazardous Materials*, 147(1-2):471–477, aug 2007.
- [183] Talaat M. Hammad, Jamil K. Salem, and R. G. Harrison. Structure, optical properties and synthesis of Co-doped ZnO superstructures. *Applied Nanoscience (Switzerland)*, 3(2):133–139, apr 2013.
- [184] Hongjing Hao, Mei Qin, and Ping Li. Structural, optical, and magnetic properties of Co-doped ZnO nanorods fabricated by a facile solution route. *Journal of Alloys and Compounds*, 515:143–148, feb 2012.
- [185] Yongchun Lu, Yanhong Lin, Dejun Wang, Lingling Wang, Tengfeng Xie, and Tengfei Jiang. A high performance cobalt-doped ZnO visible light photocatalyst and its photogenerated charge transfer properties. *Nano Research*, 4(11):1144–1152, jul 2011.
- [186] M. Nirmala and A. Anukaliani. Synthesis and characterization of undoped and TM (Co, Mn) doped ZnO nanoparticles. *Materials Letters*, 65(17-18):2645–2648, sep 2011.
- [187] Megha Vagadia, Ashish Raval, Uma Khachar, P. S. Solanki, R. R. Doshi, S. Rayaprol, and D. G. Kuberkar. Size and grain morphology dependent magnetic behaviour of Co-doped ZnO. *Materials Research Bulletin*, 46(11):1933–1937, nov 2011.
- [188] R. Elilarassi and G. Chandrasekaran. Microstructural and photoluminescence properties of Co-doped ZnO films fabricated using a simple solution growth method. *Materials Science in Semiconductor Processing*, 14(2):179–183, jun 2011.
- [189] Manjula G. Nair, M. Nirmala, K. Rekha, and A. Anukaliani. Structural, optical, photocatalytic and antibacterial activity of ZnO and Co doped ZnO nanoparticles. *Materials Letters*, 65(12):1797–1800, jun 2011.
- [190] Huaming Yang and Sha Nie. Preparation and characterization of Co-doped ZnO nanomaterials. *Materials Chemistry and Physics*, 114(1):279–282, mar 2009.
- [191] E. V. Gritskova, D. M. Mukhamedshina, K. A. Mit', N. A. Dolya, and Kh A. Abdullin. The structure, photoluminescence, optical and magnetic properties of ZnO films doped with ferromagnetic impurities. *Physica B: Condensed Matter*, 404(23-24):4816–4819, dec 2009.

- [192] Zhuliang Wang, Xiaoli Li, Fengxian Jiang, Baoqiang Tian, Baohua Lu, and Xiaohong Xu. Effect of substrate temperature on the room temperature ferromagnetism of co-doped ZnO thin films. *Xiyou Jinshu Cailiao Yu Gongcheng/Rare Metal Materials and Engineering*, 37(5):831–834, may 2008.
- [193] Chao Xu, Lixin Cao, Ge Su, Wei Liu, Xiaofei Qu, and Yaqin Yu. Preparation, characterization and photocatalytic activity of Co-doped ZnO powders. *Journal of Alloys and Compounds*, 497(1-2):373–376, may 2010.
- [194] Huijuan Zhou, Limei Chen, Vivek Malik, Christoph Knies, Detlev M. Hofmann, Kanwal Preet Bhatti, S. Chaudhary, Peter J. Klar, Wolfram Heimbrodt, Claus Klingshirn, and Heinz Kalt. Raman studies of zno:co thin films. *physica status solidi (a)*, 204(1):112–117, 2007.
- [195] K. Barmak, A. Gungor, A. D. Rollett, C. Cabral, and J. M.E. Harper. Texture of Cu and dilute binary Cu-alloy films: Impact of annealing and solute content. *Materials Science in Semiconductor Processing*, 6(4):175–184, aug 2003.
- [196] Zhengwei Li and W. Gao. ZnO thin films with DC and RF reactive sputtering. *Materials Letters*, 58(7-8):1363–1370, mar 2004.
- [197] Asim Jilani, Javed Iqbal, Saqib Rafique, M. Sh Abdel-wahab, Yasir Jamil, and Attieh A. Al-Ghamdi. Morphological, optical and X-ray photoelectron chemical state shift investigations of ZnO thin films. *Optik*, 127(16):6358–6365, aug 2016.
- [198] Hualan Zhou and Zhuang Li. Synthesis of nanowires, nanorods and nanoparticles of ZnO through modulating the ratio of water to methanol by using a mild and simple solution method. *Materials Chemistry and Physics*, 89(2-3):326–331, feb 2005.
- [199] Mark C. Biesinger, Brad P. Payne, Andrew P. Grosvenor, Leo W.M. Lau, Andrea R. Gerson, and Roger St C. Smart. Resolving surface chemical states in XPS analysis of first row transition metals, oxides and hydroxides: Cr, Mn, Fe, Co and Ni. *Applied Surface Science*, 257(7):2717–2730, jan 2011.
- [200] Xiaoyuan Yang, Shujie Wu, Ling Peng, Jing Hu, Xiufang Wang, Xiaoran Fu, Qisheng Huo, and Jingqi Guan. Highly dispersed cobalt oxide nanoparticles on CMK-3 for selective oxidation of benzyl alcohol. *RSC Advances*, 5(124):102508–102515, nov 2015.
- [201] Xiong Wang, Xiangying Chen, Lisheng Gao, Huagui Zheng, Zude Zhang, and Yitai Qian. One-dimensional arrays of Co<sub>3</sub>O<sub>4</sub> nanoparticles: Synthesis, characterization, and optical and electrochemical properties. *Journal of Physical Chemistry B*, 108(42):16401–16404, oct 2004.

- [202] Mingce Long, Weimin Cai, Jun Cai, Baoxue Zhou, Xinye Chai, and Yahui Wu. Efficient photocatalytic degradation of phenol over  $\text{Co}_3\text{O}_4/\text{BiVO}_4$  composite under visible light irradiation. *Journal of Physical Chemistry B*, 110(41):20211–20216, oct 2006.
- [203] J. G. Dillard, C. V. Shenck, and M. H. Koppelman. Surface chemistry of cobalt in calcined cobalt-kaolinite materials. *Clays & Clay Minerals*, 31(1):69–72, 1983.
- [204] Shoko Aoi, Kentaro Mase, and Shunichi Ohkubo, Kei 38d Fukuzumi. Selective electrochemical reduction of  $\text{CO}_2$  to  $\text{CO}$  with a cobalt chlorin complex adsorbed on multi-walled carbon nanotubes in water. *Chemical Communications*, 51(50):10226–10228, may 2015.
- [205] P. Paufler. R. A. Young (ed.). The Rietveld Method. International Union of Crystallography. Oxford University Press 1993. 298 p. Price £ 45.00. ISBN 0–19–855577–6. *Crystal Research and Technology*, 30(4):494–494, jan 1995.
- [206] M. Rodríguez Gallego. *de La difracción de los rayos X*. Alhambra, 1982.
- [207] H. P. Rooksby. *The powder method in X-ray crystallography* by L. V. Azaroff and J. Buerger. *Acta Crystallographica*, 11(10):753–754, oct 1958.
- [208] José María Albella. *Láminas delgadas y recubrimientos: Preparación, Propiedades y Aplicaciones*. Editorial CSIC, 2003.
- [209] Siegfried Hofmann. *Auger- and X-Ray Photoelectron Spectroscopy in Materials Science*, volume 49 of *Springer Series in Surface Sciences*. Springer Berlin Heidelberg, Berlin, Heidelberg, 2013.
- [210] C. Kittel. *Introducción a la física del estado sólido*. Reverté, 1995.
- [211] Principios básicos del microscopio electrónico de barrido.
- [212] CSN. TEMA 2: INTERACCIÓN DE LA RADIACIÓN CON LA MATERIA. Technical report, Consejo de Seguridad Nacional, España, 2009.
- [213] G. Binnig, C. F. Quate, and Ch Gerber. Atomic force microscope. *Physical Review Letters*, 56(9):930–933, mar 1986.
- [214] M. Tay, Y. H. Wu, G. C. Han, Y. B. Chen, X. Q. Pan, S. J. Wang, P. Yang, and Y. P. Feng. Structural, optical, magnetic and electrical properties of  $\text{Zn}_{1-x}\text{Co}_x\text{O}$  thin films. *Journal of Materials Science: Materials in Electronics*, 20(1):60–73, feb 2009.
- [215] Hong Ding, Shyam S. Dwaraknath, Lauren Garten, Paul Ndione, David Ginley, and Kristin A. Persson. Computational approach for epitaxial polymorph stabilization through substrate selection. *ACS Applied Materials & Interfaces*, 8(20):13086–13093, 2016. PMID: 27145398.

- [216] Won Seok Seo, Jae Ha Shim, Sang Jun Oh, Eun Kwang Lee, Nam Hwi Hur, and Joon T. Park. Phase- and size-controlled synthesis of hexagonal and cubic CoO nanocrystals. *Journal of the American Chemical Society*, 127(17):6188–6189, may 2005.
- [217] Kiyotaka Wasa, Makoto Kitabatake, and Hideaki Adachi. 2 - thin film processes. In Kiyotaka Wasa, Makoto Kitabatake, and Hideaki Adachi, editors, *Thin Film Materials Technology*, pages 17 – 69. William Andrew Publishing, Norwich, NY, 2004.
- [218] Claude Chappert, Albert Fert, and Frédéric Nguyen Van Dau. The emergence of spin electronics in data storage. *Nature Materials*, 6(11):813–823, 2007.
- [219] H. Ohno, D. Chiba, F. Matsukura, T. Omiya, E. Abe, T. Dietl, Y. Ohno, and K. Ohtani. Electric-field control of ferromagnetism. *Nature*, 408(6815):944–946, dec 2000.
- [220] Ahsan M. Nazmul, S. Sugahara, and M. Tanaka. Ferromagnetism and high Curie temperature in semiconductor heterostructures with Mn  $\delta$ -doped GaAs and p-type selective doping. *Physical Review B - Condensed Matter and Materials Physics*, 67(24):241308, jun 2003.
- [221] Rainer Waser and Masakazu Aono. Nanoionics-based resistive switching memories. *Nature Materials*, 6(11):833–840, nov 2007.
- [222] D. Chiba, S. Fukami, K. Shimamura, N. Ishiwata, K. Kobayashi, and T. Ono. Electrical control of the ferromagnetic phase transition in cobalt at room temperature. *Nature Materials*, 10(11):853–856, oct 2011.
- [223] Thomas Lottermoser, Thomas Lonkai, Uwe Amann, Dietmar Hohlwein, Jörg Ihringer, and Manfred Fiebig. Magnetic phase control by an electric field. *Nature*, 430(6999):541–544, jul 2004.
- [224] Ying Hao Chu, Lane W. Martin, Mikel B. Holcomb, Martin Gajek, Shu Jen Han, Qing He, Nina Balke, Chan Ho Yang, Donkoun Lee, Wei Hu, Qian Zhan, Pei Ling Yang, Arantxa Fraile-Rodríguez, Andreas Scholl, Shan X. Wang, and R. Ramesh. Electric-field control of local ferromagnetism using a magnetoelectric multiferroic. *Nature Materials*, 7(6):478–482, apr 2008.
- [225] I. Stolichnov, S. W.E. Riester, H. J. Trodahl, N. Setter, A. W. Rushforth, K. W. Edmonds, R. P. Campion, C. T. Foxon, B. L. Gallagher, and T. Jungwirth. Non-volatile ferroelectric control of ferromagnetism in (Ga,Mn)As. *Nature Materials*, 7(6):464–467, may 2008.
- [226] Yu Chao Yang, Feng Pan, Qi Liu, Ming Liu, and Fei Zeng. Fully room-temperature-fabricated nonvolatile resistive memory for ultrafast and high-density memory application. *Nano Letters*, 9(4):1636–1643, apr 2009.

- [227] J. M.D. Coey, M. Venkatesan, and C. B. Fitzgerald. Donor impurity band exchange in dilute ferromagnetic oxides. *Nature Materials*, 4(2):173–179, feb 2005.
- [228] F. Pan, C. Song, X. J. Liu, Y. C. Yang, and F. Zeng. Ferromagnetism and possible application in spintronics of transition-metal-doped ZnO films. *Materials Science and Engineering R: Reports*, 62(1):1–35, jun 2008.
- [229] Satishchandra B. Ogale. Dilute Doping, Defects, and Ferromagnetism in Metal Oxide Systems. *Advanced Materials*, 22(29):3125–3155, aug 2010.
- [230] C. Song, X. J. Liu, K. W. Geng, F. Zeng, F. Pan, B. He, and S. Q. Wei. Transition from diluted magnetic insulator to semiconductor in Co-doped ZnO transparent oxide. *Journal of Applied Physics*, 101(10):103903, may 2007.
- [231] K. Ip, R. M. Frazier, Y. W. Heo, D. P. Norton, C. R. Abernathy, S. J. Pearton, J. Kelly, R. Rairigh, A. F. Hebard, J. M. Zavada, and R. G. Wilson. Ferromagnetism in Mn- and Co-implanted ZnO nanorods. *Journal of Vacuum Science & Technology B: Microelectronics and Nanometer Structures*, 21(4):1476, jul 2003.
- [232] S. J. Pearton, C. R. Abernathy, G. T. Thaler, R. Frazier, F. Ren, A. F. Hebard, Y. D. Park, D. P. Norton, W. Tang, M. Stavola, J. M. Zavada, and R. G. Wilson. Effects of defects and doping on wide band gap ferromagnetic semiconductors. In *Physica B: Condensed Matter*, volume 340-342, pages 39–47. North-Holland, dec 2003.
- [233] N. A. Theodoropoulou, A. F. Hebard, D. P. Norton, J. D. Budai, L. A. Boatner, J. S. Lee, Z. G. Khim, Y. D. Park, M. E. Overberg, S. J. Pearton, and R. G. Wilson. Ferromagnetism in Co- and Mn-doped ZnO. *Solid-State Electronics*, 47(12):2231–2235, dec 2003.
- [234] Milan Gacic, Gerhard Jakob, Christian Herbort, Hermann Adrian, Thomas Tietze, Sebastian Brück, and Eberhard Goering. Magnetism of Co-doped ZnO thin films. *Physical Review B - Condensed Matter and Materials Physics*, 75(20):205206, may 2007.
- [235] H. Schmidt, M. Diaconu, H. Hochmuth, G. Benndorf, H. Von Wenckstern, G. Biehne, M. Lorenz, and M. Grundmann. Electrical and optical spectroscopy on ZnO:Co thin films. *Applied Physics A: Materials Science and Processing*, 88(1):157–160, jul 2007.
- [236] Kanwal Preet Bhatti, Sujeet Chaudhary, Dinesh K. Pandya, and Subhash C. Kashyap. High temperature investigation of the magnetization behavior in cobalt substituted ZnO. *Journal of Applied Physics*, 101(3):033902, feb 2007.
- [237] A. Quesada, M. A. García, M. Andrés, A. Hernando, J. F. Fernández, A. C. Caballero, M. S. Martín-González, and F. Briones. Ferromagnetism in bulk Co-Zn-O. *Journal of Applied Physics*, 100(11):113909, dec 2006.

- [238] Kevin R. Kittilstved, William K. Liu, and Daniel R. Gamelin. Electronic structure origins of polarity-dependent high-T<sub>c</sub> ferromagnetism in oxide-diluted magnetic semiconductors. *Nature Materials*, 5(4):291–297, apr 2006.
- [239] M. Ivill, S. J. Pearton, D. P. Norton, J. Kelly, and A. F. Hebard. Magnetization dependence on electron density in epitaxial ZnO thin films codoped with Mn and Sn. *Journal of Applied Physics*, 97(5):053904, mar 2005.
- [240] M. Ivill, S. J. Pearton, Y. W. Heo, J. Kelly, A. F. Hebard, and D. P. Norton. Magnetization dependence on carrier doping in epitaxial ZnO thin films co-doped with Mn and P. *Journal of Applied Physics*, 101(12):123909, jun 2007.
- [241] D. A. Schwartz and D. R. Gamelin. Reversible 300 K Ferromagnetic Ordering in a Diluted Magnetic Semiconductor. *Advanced Materials*, 16(23-24):2115–2119, dec 2004.
- [242] N. Khare, M.J. Kappers, M. Wei, M.G. Blamire, and J.L. MacManus-Driscoll. Defect-Induced Ferromagnetism in Co-doped ZnO. *Advanced Materials*, 18(11):1449–1452, jun 2006.
- [243] C. D. Pemmaraju, R. Hanafin, T. Archer, H. B. Braun, and S. Sanvito. Impurity-ion pair induced high-temperature ferromagnetism in Co-doped ZnO. *Physical Review B - Condensed Matter and Materials Physics*, 78(5):054428, aug 2008.
- [244] L. B. Duan, W. G. Chu, J. Yu, Y. C. Wang, L. N. Zhang, G. Y. Liu, J. K. Liang, and G. H. Rao. Structural and magnetic properties of Zn<sub>1-x</sub>CoxO nanoparticles. *Journal of Magnetism and Magnetic Materials*, 320(8):1573–1581, apr 2008.
- [245] Q. Liu, C. L. Yuan, C. L. Gan, and G. C. Han. Effect of substrate temperature on pulsed laser ablated Zn<sub>0.95</sub>Co<sub>0.05</sub>O diluted magnetic semiconducting thin films. *Journal of Applied Physics*, 101(7):073902, apr 2007.
- [246] Zhengwu W. Jin, M. Murakami, T. Fukumura, Y. Matsumoto, A. Ohtomo, M. Kawasaki, and H. Koinuma. Combinatorial laser MBE synthesis of 3d ion doped epitaxial ZnO thin films. *Journal of Crystal Growth*, 214:55–58, jun 2000.
- [247] S. S. Lee, G. Kim, S. C. Wi, J. S. Kang, S. W. Han, Y. K. Lee, K. S. An, S. J. Kwon, M. H. Jung, and H. J. Shin. Investigation of the phase separations and the local electronic structures of Zn<sub>1-x</sub>T<sub>x</sub>O (T=Mn, Fe, Co) magnetic semiconductors using synchrotron radiation. *Journal of Applied Physics*, 99(8):08M103, apr 2006.
- [248] Igor Ozerov, Françoise Chabre, and Wladimir Marine. Incorporation of cobalt into ZnO nanoclusters. *Materials Science and Engineering C*, 25(5-8):614–617, dec 2005.



- [249] H. S. Hsu, J. C.A. Huang, Y. H. Huang, Y. F. Liao, M. Z. Lin, C. H. Lee, J. F. Lee, S. F. Chen, L. Y. Lai, and C. P. Liu. Evidence of oxygen vacancy enhanced room-temperature ferromagnetism in Co-doped ZnO. *Applied Physics Letters*, 88(24):242507, jun 2006.
- [250] C. Song, F. Zeng, K. W. Geng, X. B. Wang, Y. X. Shen, and F. Pan. The magnetic properties of Co-doped ZnO diluted magnetic insulator films prepared by direct current reactive magnetron co-sputtering. *Journal of Magnetism and Magnetic Materials*, 309(1):25–30, feb 2007.
- [251] K. Samanta, P. Bhattacharya, and R. S. Katiyar. Optical properties of Zn  $1-x$ Co  $x$ O thin films grown on Al  $2O_3$  (0001) substrates. *Applied Physics Letters*, 87(10):101903, sep 2005.
- [252] Kwang Joo Kim and Young Ran Park. Spectroscopic ellipsometry study of optical transitions in Zn  $1-x$ CoxO alloys. *Applied Physics Letters*, 81(8):1420–1422, aug 2002.
- [253] M. Bouloudenine, N. Viart, S. Colis, and A. Dinia. Bulk Zn  $1 - x$ Co  $x$ O magnetic semiconductors prepared by hydrothermal technique. *Chemical Physics Letters*, 397(1-3):73–76, oct 2004.
- [254] S. Venkataprasad Bhat and F. L. Deepak. Tuning the bandgap of ZnO by substitution with Mn $^{2+}$ , Co  $^{2+}$  and Ni $^{2+}$ . *Solid State Communications*, 135(6):345–347, aug 2005.
- [255] Xue Chao Liu, Er Wei Shi, Zhi Zhan Chen, Hua Wei Zhang, Li Xin Song, Huan Wang, and Shu De Yao. Structural, optical and magnetic properties of Co-doped ZnO films. *Journal of Crystal Growth*, 296(2):135–140, nov 2006.
- [256] Y. R. Lee, A. K. Ramdas, and R. L. Aggarwal. Energy gap, excitonic, and internal Mn $^{2+}$  optical transition in Mn-based II-VI diluted magnetic semiconductors. *Physical Review B*, 38(15):10600–10610, nov 1988.
- [257] Y. Z. Peng, T. Liew, W. D. Song, C. W. An, K. L. Teo, and T. C. Chong. Structural and optical properties of Co-doped ZnO thin films. *Journal of Superconductivity and Novel Magnetism*, 18(1):97–103, 2005.
- [258] Y. Z. Yoo, T. Fukumura, Zhengwu Jin, K. Hasegawa, M. Kawasaki, P. Ahmet, T. Chikyow, and H. Koinuma. ZnO-CoO solid solution thin films. *Journal of Applied Physics*, 90(8):4246–4250, oct 2001.
- [259] F. M. Smits. Measurement of sheet resistivities with the four-point probe. *Bell System Technical Journal*, 37(3):711–718, 1958.
- [260] F. Wenner. *A Method of Measuring Earth Resistivity*. Number n.<sup>o</sup> 258 in Bulletin of the Bureau of Standards. U.S. Government Printing Office, 1916.

- [261] K. H. J. Buschow and F. R. de Boer. *Physics of Magnetism and Magnetic Materials*. Springer US, 2003.
- [262] F. Mesa, B. A. Paez-Sierra, A. Romero, P. Botero, and S. Ramírez-Clavijo. Assisted laser impedance spectroscopy to probe breast cancer cells. *Journal of Physics D: Applied Physics*, 54(7):15, feb 2021.
- [263] Sang-Wook Lim, Deuk-Kyu Hwang, and Jae-Min Myoung. Observation of optical properties related to room-temperature ferromagnetism in co-sputtered zn1-xcoco thin films. *Solid State Communications*, 125(5):231–235, 2003.
- [264] P. Koidl. Optical absorption of  $\text{co}^{2+}$  in zno. *Phys. Rev. B*, 15:2493–2499, Mar 1977.
- [265] D. F. Swinehart. The Beer-Lambert law. *Journal of Chemical Education*, 39(7):333–335, 1962.
- [266] Luciano D. Sappia, Matias R. Trujillo, Israel Lorite, Rossana E. Madrid, Monica Tirado, David Comedi, and Pablo Esquinazi. Nanostructured zno films: A study of molecular influence on transport properties by impedance spectroscopy. *Materials Science and Engineering: B*, 200:124–131, 2015.
- [267] M. Chaik, S. Ben Moumen, A. Agdad, C.M. SambaVall, H. El Aakib, H. AitDads, A. Outzourhit, and L. Essaleh. Electrical impedance spectroscopy characterization of znte thin film deposited by r-f sputtering. *Physica B: Condensed Matter*, 572:76–80, 2019.
- [268] M. Dolores Perez, Fernando D. González, Natalia B. Correa Guerrero, and Federico A. Viva. Carrier conduction mechanisms of mesoporous titania thin films assessed by impedance spectroscopy. *Microporous and Mesoporous Materials*, 283:31–38, 2019.
- [269] Andrew W. Stephan, Qiuwen Lou, Michael T. Niemier, Xiaobo Sharon Hu, and Steven J. Koester. Nonvolatile spintronic memory cells for neural networks. *IEEE Journal on Exploratory Solid-State Computational Devices and Circuits*, 5(2):67–73, 2019.
- [270] G. Schmidt, D. Ferrand, L. W. Molenkamp, A. T. Filip, and B. J. van Wees. Fundamental obstacle for electrical spin injection from a ferromagnetic metal into a diffusive semiconductor. *Phys. Rev. B*, 62:R4790–R4793, Aug 2000.
- [271] P. R. Hammar, B. R. Bennett, M. J. Yang, and Mark Johnson. Observation of spin injection at a ferromagnet-semiconductor interface. *Phys. Rev. Lett.*, 83:203–206, Jul 1999.